JETP Letters, Vol. 80, No. 2, 2004, pp. 103–108. Translated from Pis'ma v Zhurnal Éksperimental'noĭ i Teoreticheskoĭ Fiziki, Vol. 80, No. 2, 2004, pp. 112–117.

Stable Nonlinear Excitations of the Spiral Type in 2D Magnetic Models

A. B. Borisov[1], I. G. Bostrem[2], and A. S. Ovchinnikov[2]

[1]*Institute of Metal Physics, Ural Division, Russian Academy of Sciences, Yekaterinburg, 620219 Russia*

[2]*Ural State University, Yekaterinburg, 620083 Russia*

Received May 14, 2004

A new class of stable topological excitations having the shape of small-amplitude spirals is considered in a 2D isotropic Heisenberg ferromagnet model. An exact solution generalizing some previous results is obtained. The main characteristics of small-amplitude spirals are determined using the conservation laws. The possibilities of experimental realization of such spiral structures are considered. © *2004 MAIK "Nauka/Interperiodica".*

PACS numbers: 75.10.Hk; 75.75.+a

In recent years, much attention has been devoted to the investigation of static and dynamic properties of nanomagnets (magnetic dots) in view of their possible use in data storage and recording devices [1, 2]. Experimental and numerical investigation of the magnetic structures formed in nanomaterials of various shapes—in particular, several-nanometer-thick disks [3] and parallelepipeds [4]—revealed various types of such structures. It was established that, at a fixed thickness, the ground or metastable state of these systems corresponds either to a planar single-domain ordering (if the characteristic radius l of the system, which is on the order of several hundred nanometers, does not exceed a certain critical value l_c), or to various vortexlike states (for $l > l_c$) with possible deviation of the magnetization vector from the disk plane [5].

The presence of vortex structures in magnetic dots was confirmed by electron microscopy and magnetic force microscopy techniques [6]. The switching processes, induced by in-plane or perpendicular pulsed magnetic fields, excite either magnetic structures of the skyrmion type theoretically predicted in [7] or the spiral structures [8]. It should be noted that magnetic structures of the shooting-target or spiral-domain type have been observed in thin magnetic films with a strong perpendicular anisotropy of the easy-axis type, being formed under the action of a harmonic or pulsed magnetic field from a disordered domain structure [9–11]. Such structures are expediently considered as quasi-stationary because they do not disappear when the magnetic field is switched off and their lifetimes are much greater than the magnetic field period.

Topological excitations in two-dimensional (2D) magnets are among the most important objects for investigation in the physics of low-dimensional magnetic systems. Despite numerous publications in this field, the phenomenon of spiral excitations in magnetic models has not received much attention. However, detailed study of the spiral solutions within both *XY* and Heisenberg models (in view of their universal character) is of interest both for the theory of low-dimensional magnetism and for the possible applications in the physics of liquid crystals and quantum Hall effect and in the study of biological systems featuring self-organized spiral structures [12].

A special class of spiral solutions which can be realized in 2D ferromagnets was recently studied in [13]. In this paper, we will consider the structure of small-amplitude spiral vortices in 2D ferromagnets. It will be demonstrated that such structures are formed due to the main exchange interaction. A new class of exact solutions of nonlinear equations in the Heisenberg model will be obtained using a special "linearization" procedure. First, we will construct a function of the initial dynamical variables satisfying the linear Laplace equation. Then, the reverse transformation leads to solutions of the initial nonlinear model, representing elementary functions of the harmonic solutions of the Laplace equation. Finally, we will consider the possibilities of experimental realization of such spiral structures.

Let us consider the standard isotropic Heisenberg Hamiltonian $H = -J\sum_{\langle ij\rangle} \mathbf{S}_i\mathbf{S}_j$ for the spin S on a square lattice, describing the interaction of nearest neighbors ($J > 0$ is the corresponding exchange integral). Using a continuum variant of the equations of spin motion corresponding to this Hamiltonian and introducing the spin angle variables θ and φ, the stationary solutions can be determined from the following system of nonlinear equations:

$$\begin{aligned} \Delta\theta &= \sin\theta\cos\theta(\nabla\varphi)^2, \\ \nabla(\sin^2\theta\nabla\varphi) &= 0. \end{aligned} \tag{1}$$

0021-3640/04/8002-0103$26.00

Axisymmetric solutions with the parametrization $\varphi = \varphi(\phi)$ and $\theta = \theta(r)$, where (r, ϕ) are the polar coordinates in the *xy* plane, obey the obvious relation $\nabla\varphi \perp \nabla\theta$. In order to find a solution of another class with $\nabla\varphi \parallel \nabla\theta$, we use the ansatz $\nabla\varphi = f(\theta)\nabla\theta$. Then, explicit expressions for the variables θ and φ are determined according to Eqs. (1) by a function f found from the Bernoulli equation

$$\sin\theta\frac{df}{d\theta} + 2f\cos\theta + f^3\sin^2\theta\cos\theta = 0. \quad (2)$$

The general solution to Eq. (2) is determined by a single-parametric family of the functions

$$f(\theta) = \frac{1}{\sqrt{c^2\sin^4\theta - \sin^2\theta}}, \quad (3)$$

where c is an arbitrary constant such that $c^2 > 1$.

Using relations (2) and (3), the initial system of equations (1) can be reduced to the Laplace equation

$$\Delta\left(\arccos\left[\frac{c\cos\theta}{\sqrt{c^2-1}}\right]\right) = 0. \quad (4)$$

A solution to this equation is given by the harmonic function

$$a(x, y) = \arccos\left[\frac{c\cos\theta}{\sqrt{c^2-1}}\right] \ (\Delta a = 0), \quad (5)$$

which yields the formulas for angles θ and φ:

$$\cos\theta = \frac{\sqrt{c^2-1}}{c}\cos a, \qquad \varphi = \arctan(c\tan a) + \varphi_0. \quad (6)$$

Below, we will consider the solutions $a(x, y)$ having the following form:

$$a = \sum_i \alpha_i \ln\left(\frac{\sqrt{(x-x_{0i})^2 + (y-y_{0i})^2}}{R_i}\right) + \sum_i q_i \arctan\left(\frac{y-\tilde{y}_{0i}}{x-\tilde{x}_{0i}}\right), \quad q_i \in Z. \quad (7)$$

The family of solutions is determined by the parameters α_i, q_i, R_i, and c; by coordinates of the sources (x_{0i}, y_{0i}), by the vortices $(\tilde{x}_{0i}, \tilde{y}_{0i})$; and by the initial azimuthal angle φ_0. The parameter α_i may be considered, by analogy with hydrodynamics, as the source "power." The parameter $c \geq 1$ controls the "amplitude" of the spin deviation from the *xy* plane: the limiting value $c = 1$ corresponds to the *xy* model ($\theta = \pi/2$ and $\nabla\theta = 0$). Solutions (7) may be called small-amplitude, because the angle θ occurs in the interval $\pi/2 - \theta_{\max} \leq \theta < \pi/2 + \theta_{\max}$, where $\theta_{\max} = \arcsin\sqrt{c^2-1}/c$. Formulas (6) and (7) describe both new and some of the partial solutions considered previously:

(i) **Flat vortices ($c = 1$).** Using the general formula (6) corresponding to flat spirals with $\theta = \pi/2$ and $\varphi = q\phi + \alpha\ln(r/R)$, we obtain for $\alpha = 0$ the well-known Kosterlitz–Thouless (KT) vortices [14], while $q = 0$ corresponds to the case of "sources" with $\varphi = \alpha\ln(r/R)$ [15].

(ii) **Nodal solutions.** The structures with $\alpha \neq 0$, $q = 0$, and the angles

$$\cos\theta = \frac{\sqrt{c^2-1}}{c}\cos\left(\alpha\ln\frac{r}{R}\right), \qquad \varphi = \arctan\left(c\tan\left(\alpha\ln\frac{r}{R}\right)\right) + \varphi_0 \quad (8)$$

determine the so-called "nodal" solutions analyzed in detail previously [16].

A new type of 2D structures determined by the relations

$$\cos\theta = \frac{\sqrt{c^2-1}}{c}\cos\left(\alpha\ln\frac{r}{R} + q\phi\right), \qquad \varphi = \arctan\left(c\tan\left(\alpha\ln\frac{r}{R} + q\phi\right)\right) + \varphi_0 \quad (9)$$

is flat spirals. The shapes of such spirals with various twist parameters α and the arm numbers q are illustrated in Fig. 1. For $\alpha = 0$, we obtain an out-of-plane vortex with

$$\cos\theta = \frac{\sqrt{c^2-1}}{c}\cos(q\phi), \qquad \varphi = \arctan(c\tan(q\phi)) + \varphi_0. \quad (10)$$

In contrast to skyrmion, this vortex has a zero topological charge: $\pi_2(S_2) = 0$. Note that the out-of-plane vortex is not axisymmetric and there is no relation between θ and r.

Let us consider the conservation laws and the stability of such new solutions. The necessary relations are presented in [17]. The excitation energy in the continuum approximation has the compact form

$$E = \frac{1}{2}JS^2\int d\mathbf{r}(\nabla a)^2. \quad (11)$$

Using formula (7) for the function a, we arrive at an expression analogous to that for the energy of a system of interacting flat vortices (with the product q_iq_j replaced by the sum $q_iq_j + \alpha_i\alpha_j$):

$$E = \pi JS^2 \times\left\{\sum_i(\alpha_i^2 + q_i^2)\ln\frac{L}{a} + \sum_{ij}(\alpha_i\alpha_j + q_iq_j)\ln\frac{L}{d_{ij}}\right\},$$

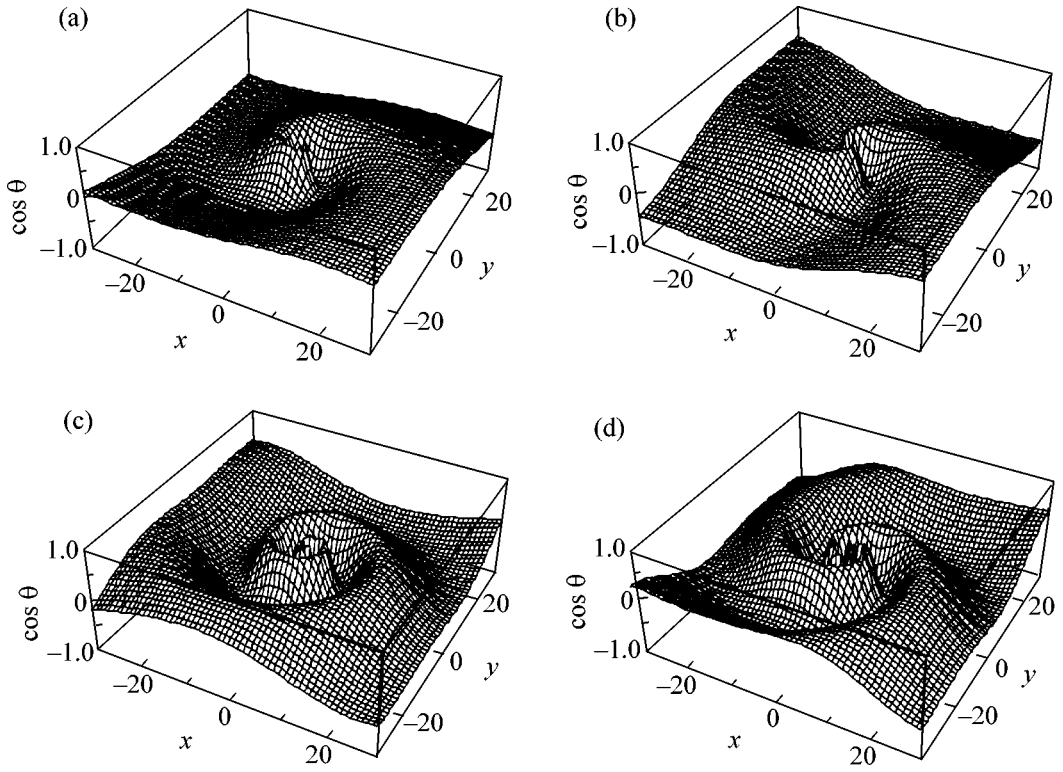

Fig. 1. Spatial distribution of magnetization in small-amplitude spirals with different numbers of arms [$q = 1$ (a, c) and 2 (b, d)] and twist parameters [$\alpha = 2.0$ (a, b) and 4.5 (c, d)].

where $d_{ij} = \sqrt{(x_{0i} - x_{0j})^2 + (y_{0i} - y_{0j})^2}$ is the distance between ith and jth vortex sources, L is the system size, and a is the lattice parameter. Note that the expression contains no cross-terms of the $\alpha_i q_j$ type (i.e., the vortices do not interact with sources) and that the energy depends neither on R_i nor on the parameter c (the amplitude of spin deviation from the xy plane).

The structures of size d with the parameters (α, q) and ($-\alpha$, $-q$) form, similar to flat vortices, a dipole (Fig. 2) with a finite energy

$$E = 2\pi JS^2(\alpha^2 + q^2)\ln\frac{d}{a}.$$

The density of momentum $\mathbf{P} = \hbar S(1 - \cos\theta)\nabla\varphi$ of the 2D spiral can be represented as

$$\mathbf{P} = \frac{\hbar S}{c + \sqrt{c^2 - 1}\cos a}\nabla a.$$

This value has both a radial component,

$$P_r = \frac{\hbar S}{c + \sqrt{c^2 - 1}\cos a}\frac{\alpha}{r},$$

and a tangential component,

$$P_\phi = \frac{\hbar S}{c + \sqrt{c^2 - 1}\cos a}\frac{q}{r},$$

determined by the twist parameter (α) and the number of spiral arms (q), respectively. The relations

$$\int_0^{2\pi} P_r R_0 d\phi = \alpha\hbar S\int_0^{2\pi} d\phi\frac{1}{c + \sqrt{c^2 - 1}\cos\left(q\phi + \alpha\ln\frac{r}{R}\right)} = 2\pi\alpha\hbar S$$

and

$$\int_0^{2\pi} P_\phi R_0 d\phi = q\hbar S\int_0^{2\pi} d\phi\frac{1}{c + \sqrt{c^2 - 1}\cos\left(q\phi + \alpha\ln\frac{r}{R}\right)} = 2\pi q\hbar S$$

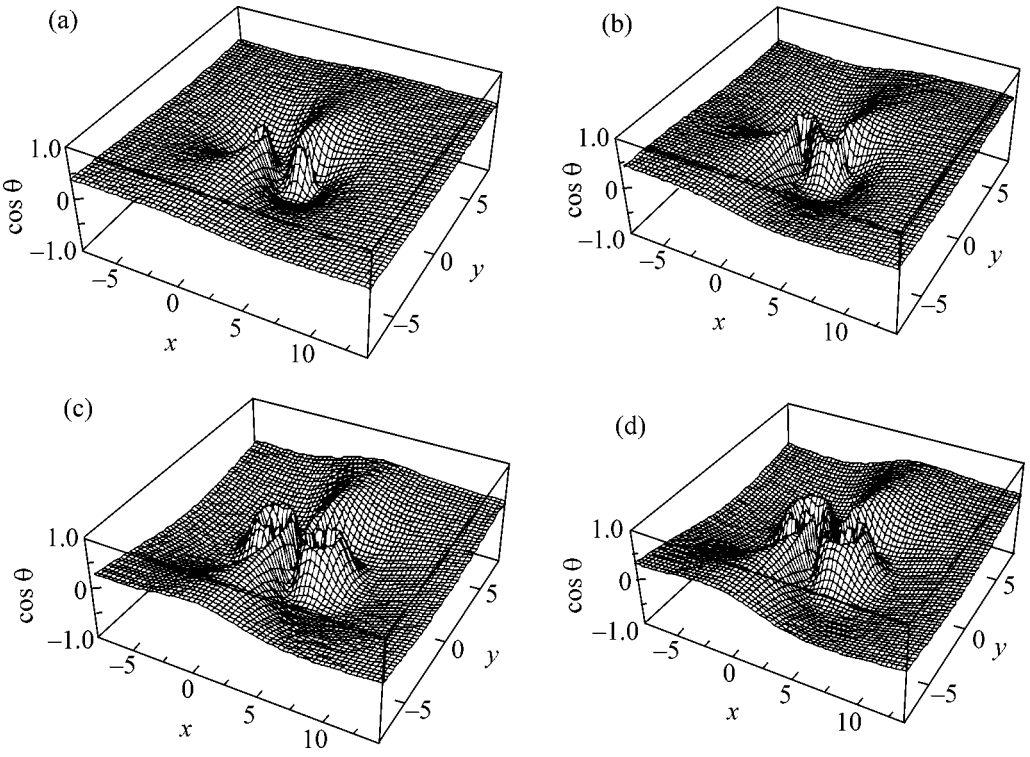

Fig. 2. Spatial distribution of magnetization in a pair of small-amplitude spirals with the separation $d = 4$ (other parameters are the same as in Fig. 1).

show that the parameters α and q also determine the flux through a circle of radius R_0 and the circulation along this circle. Obviously, the total momentum of the system is zero, $\int \mathbf{P} d\mathbf{r} = 0$, although the total angular momentum is nonzero:

$$L_z = S\hbar q \int_0^L r dr \int_0^{2\pi} d\phi \frac{1}{c + \sqrt{c^2 - 1}\cos\left(q\phi + \alpha \ln\frac{r}{R}\right)}$$

$$= S\hbar q \pi L^2,$$

where πL^2 is the system area and

$$\frac{S\hbar q}{c + \sqrt{c^2 - 1}\cos\left(q\phi + \alpha \ln\frac{r}{R}\right)}$$

is the angular momentum density.

It is expedient to compare the two substantially different classes of solutions for the isotropic Heisenberg ferromagnets admitting analytical description: spatial spirals with $\nabla\varphi \parallel \nabla\theta$ and skyrmions [7] with $\nabla\varphi \perp \nabla\theta$ and the parametrization $\tan(\theta/2) = R/r$. The results of such a comparison are presented in the table.

Finally, note that the new solutions, like the KT vortices, are stable in the class under consideration. This statement follows from an explicit expression for spiral energy (11) and the positive definiteness of the Laplace operator. Indeed, if $\delta\phi$ is a small variation of the harmonic solution a, then

$$E[a + \delta\phi] = \frac{1}{2} JS^2 \int d\mathbf{r} (\nabla a + \nabla \delta\phi)^2$$

$$= \frac{1}{2} JS^2 \int d\mathbf{r} ((\nabla a)^2 + 2(\nabla a)(\nabla \delta\phi) + (\nabla \delta\phi)^2)$$

$$= \frac{1}{2} JS^2 \int d\mathbf{r} ((\nabla a)^2 + (\nabla \delta\phi)^2) > E[a].$$

It should be noted that spiral dipoles, being characterized by low activation energy, might appear due to a thermofluctuation mechanism and contribute to thermodynamic properties of the system. In addition, the above analysis may also be useful for solving a number of problems in the physics of nonmagnetic systems. In this context, it should be noted that rapid development of the technology of thin films grown under ultrahigh vacuum conditions made possible the synthesis of artificially structured materials (ASMs)—alloys, which usually cannot exist in the equilibrium state of a volume system. New phases in such materials may appear in the course of thin film growth due to factors such as the possibility of controlling the surface diffusion, the influence of the substrate symmetry, the substrate pressure upon the film, and the low-dimensional effects. The latter factor implies, in particular, that the homoge-

A comparison of two classes of solutions for isotropic Heisenberg ferromagnets

	Spiral	Skyrmion
Energy density	$\frac{1}{2}JS^2\left(\nabla\left[\alpha\ln\frac{r}{R}+q\phi\right]\right)^2$	$4JS^2q^2\frac{R^2}{(R^2+r^2)^2}$
Momentum density	$\frac{\hbar S}{c+\sqrt{c^2-1}\cos\left[\alpha\ln\frac{r}{R}+q\phi\right]}\left(\frac{q}{r}\mathbf{e}_\varphi+\frac{\alpha}{r}\mathbf{e}_r\right)$	$\hbar S\frac{2R^2}{R^2+r^2}\frac{q}{r}$
Total momentum **P**	0	0
Angular momentum density	$\frac{\hbar S}{c+\sqrt{c^2-1}\cos\left[\alpha\ln\frac{r}{R}+q\phi\right]}$	$\hbar Sq\frac{2R^2}{R^2+r^2}$
Total angular momentum L_z (system size, L)	$\hbar Sq\times\pi L^2$	$\hbar Sq\times\pi R^2\ln\frac{L^2+R^2}{R^2}$

neous state traditionally considered as the ground state of a 2D Heisenberg ferromagnet cannot be realized in practice if the magnetic structure possesses a nonzero momentum or angular momentum. For example, in a flat *XY* system, a KT vortex will be the ground state of a spin system possessing an angular momentum and, accordingly, nonzero circulation of the momentum density vector.

It cannot be excluded that spiral structures will play a significant role in spin-polarized scanning tunnel microscopy (SPSTM), especially in expected microscopes with resolution on an atomic level. The SPSTM principle is based on scanning a film surface with a thin magnetized point probe (scattered field on the order of 0.1 T) and recording a magnetic signal. The strong point–sample interaction produces significant local perturbations in the directions of magnetic moments in the film, probably even with their reversal. Evidently, there arises a nonzero momentum flux in which the ground state will be that of the source. The results of our numerical modeling on a finite lattice (to be reported in detail separately) showed that such a flux can also be obtained in a system with fixed boundary conditions, whereby an individual spin or a small cluster is fixed at a certain angle relative to the direction of homogeneous ordering of the other spin moments.

In a 2D ferromagnetic ring, two nontrivial structures can exist with $L_z \neq 0$ (see table): a skyrmion with

$$L_z = \hbar Sq\times 2\pi R^2\ln\left(\frac{R^2+R_2^2}{R^2+R_1^2}\right)$$

and a 2D spiral (9) with

$$L_z = \hbar Sq\times\pi(R_2^2-R_1^2).$$

Deviating from the plane, spins at the center of the skyrmion exhibit almost parallel ordering. This makes the formation of a skyrmion preferred to the appearance of a 2D spiral, in which the central spins are substantially nonparallel. In a ring-shaped system, skyrmions lose this advantage and the favorable solution is determined by the boundary conditions. In order to illustrate these statements, let us consider a system having the form of a flat ring with the inner and outer radii R_1 and R_2, respectively. Let us estimate exchange energies for the solutions of the "skyrmion" and "out-of-plane vortex" (10) types possessing the same angular moments L_z. The dependence of the skyrmion localization radius R on the ring parameters R_1 and R_2 can be determined from the equation

$$\hbar Sq\times\pi(R_2^2-R_1^2) = \hbar Sq\times 2\pi R^2\ln\left(\frac{R^2+R_2^2}{R^2+R_1^2}\right). \quad (12)$$

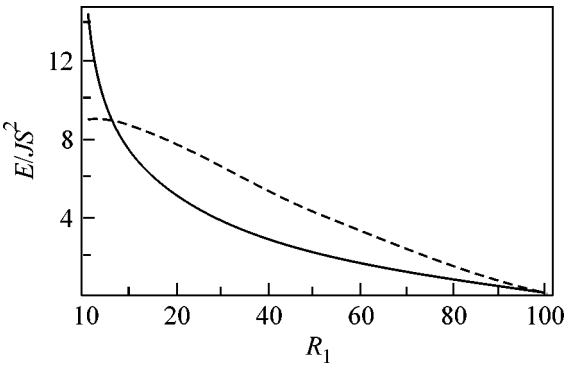

Fig. 3. The energy of a ring with a fixed outer radius (R_2 = 100) and variable inner radius R_1 for the out-of-plane vortex (solid line) and skyrmion (dashed line) solutions.

The angular momentum of the out-of-plane vortex in the ring is quantized (for the fixed values of R_1 and R_2), while the L_z of the skyrmion solution is continuous. The energies of the skyrmion (E_1) and the out-of-plane vortex (E_2) are given by the formulas

$$E_1 = 4\pi JS^2R^2\left(\frac{1}{R^2 + R_1^2} - \frac{1}{R^2 + R_2^2}\right),$$

$$E_2 = JS^2\pi\ln\left(\frac{R_2}{R_1}\right),$$

where R satisfies Eq. (12). As can be seen from Fig. 3, the out-of-plane vortex is energetically favorable for sufficiently large R_1. These considerations are also confirmed by the results of numerical modeling on a square lattice. In addition, this modeling showed that an out-of-plane spiral structure is formed for the boundary conditions $\theta(R_1) = \theta(R_2)$ and $\varphi(R_1) \neq \varphi(R_2)$. Although the energy of such spiral is greater than that of out-of-plane vortex (10), this increase in the energy is rather insignificant and the structure is still more favorable than the skyrmion with the same angular momentum.

The authors are grateful to B.A. Ivanov for fruitful discussions of some questions. This study was supported by the US Civilian Research and Development foundation for Independent Countries of the Former Soviet Union (CRDF grant no. NREC-005) and by the Russian Foundation for Basic Research (project no. 01-03-00100).

REFERENCES

1. J. Shen and J. Kirschner, Surf. Sci. **500**, 300 (2002).
2. R. Cowburn and M. E. Welland, Science **287**, 1466 (2000).
3. R. P. Cowburn, D. K. Koltsov, A. O. Adeyeye, and M. E. Welland, Phys. Rev. Lett. **83**, 1042 (1999).
4. R. Cowburn, A. O. Adeyeye, and M. E. Welland, Phys. Rev. Lett. **81**, 5414 (1998).
5. T. Shinjo, T. Okuno, R. Hassdorf, *et al.*, Science **289**, 930 (2000).
6. X. Zhu, P. Grütter, V. Metlushko, and B. Ilic, Phys. Rev. B **66**, 024423 (2002).
7. A. A. Belavin and A. M. Polyakov, JETP Lett. **22**, 245 (1975).
8. R. Höllinger, A. Killinger, and U. Krey, J. Magn. Magn. Mater. **261**, 178 (2003).
9. G. S. Kandaurova, Dokl. Akad. Nauk **331**, 428 (1993) [Phys. Dokl. **38**, 342 (1993)].
10. G. S. Kandaurova, Phys. Usp. **45**, 1051 (2002).
11. G. S. Kandaurova and A. É. Sviderskiĭ, Zh. Éksp. Teor. Fiz. **97**, 1218 (1990) [Sov. Phys. JETP **70**, 684 (1990)].
12. F. J. Nédélec, T. Surrey, A. C. Maggs, and S. Leibler, Nature **389**, 305 (1997).
13. A. B. Borisov, JETP Lett. **73**, 242 (2001).
14. J. M. Kosterlitz and D. J. Thouless, J. Phys. C: Solid State Phys. **6**, 1181 (1973); J. M. Kosterlitz, J. Phys. C: Solid State Phys. **7**, 1046 (1974).
15. A. M. Tsvelik, *Quantum Field Theory in Physics of Condensed States* (Fizmatlit, Moscow, 2002) [in Russian].
16. I. G. Bostrem and A. S. Ovchinnikov, JETP Lett. **76**, 716 (2002).
17. R. F. Egorov, I. G. Bostrem, and A. S. Ovchinnikov, Phys. Lett. A **292**, 325 (2002).

Translated by P. Pozdeev

JETP Letters, Vol. 80, No. 2, 2004, pp. 109–113. From Pis'ma v Zhurnal Éksperimental'noĭ i Teoreticheskoĭ Fiziki, Vol. 80, No. 2, 2004, pp. 118–123.

Porosity Dependence of Sound Propagation in Liquid-^{4}He-Filled Aerogel¶

K. Matsumoto[1, *], Y. Matsuyama[1], D. A. Tayurskii[1, 2, **], and K. Tajiri[3]

[1] *Department of Physics, Kanazawa University, Kakuma-machi, 920-1192 Kanazawa, Japan*

[2] *Department of Physics, Kazan State University, Kazan, 420008 Russia*

[3] *Ceramics Research Institute, National Institute of Advanced Industrial Science and Technology, 463-8560 Nagoya, Japan*

**e-mail: kmatsu@kenroku.kanazawa-u.ac.jp*

***e-mail: Dmitrii.Tayurskii@ksu.ru*

Received May 27, 2004

Longitudinal sound-wave propagation has been studied in an aerogel–liquid ^{4}He system for various porosities of aerogel. The superfluid transition was identified as the absorption peak, whose magnitude was suppressed by aerogel. The sound velocity was analyzed within a hydrodynamic theory in both normal and superfluid phases. The absorption peak due to phonon–roton interaction around 1 K was not observed even with the most porous aerogel. The low-temperature sound velocity and attenuation show that direct collisions of phonons with aerogel strands play an important role in the acoustic properties. © *2004 MAIK "Nauka/Interperiodica"*.

PACS numbers: 67.40.Pm; 67.40.Hf

Porous media filled with fluid have been intensively studied experimentally and theoretically because of their physical and technological importance. The effect of disordered pore structures on the properties of the fluid can be examined in these systems. There has been considerable interest in the behavior of superfluid ^{4}He in the presence of a random disorder induced by highly open porous media. Recent experiments on the superfluid transition of ^{4}He contained in porous media such as Aerogel, Xerogel, and Vycor glass have revealed that the superfluid transition differs from that of bulk ^{4}He [1, 2]. The superfluid transition of ^{4}He in aerogel has been observed to be sharp [1, 2] and has been suggested to manifest a genuine phase transition. The transition temperature in aerogel T_c has been suppressed with decreasing aerogel porosity.

Understanding the results of acoustic experiments is important when dealing with porous media. The use of liquid ^{4}He offers unique advantages due to the existence of the superfluid phase with more than one sound mode. The bulk fluid displays two propagating modes: first sound (compressional wave) and second sound (temperature wave) [3]. In a porous medium where the normal component is clamped by its viscosity and only the superfluid component can move, fourth sound (relative motion of the superfluid and normal fluids) propagates and can be used to determine the superfluid fraction.

Longitudinal and transverse ultrasound velocities have been measured in ^{4}He-filled Vycor glass [4]. Warner and Beamish [5] studied the transverse sound velocity and attenuation in alumina ceramics with various porosities. They argued that the experimental results in both the low- and high-frequency regimes for normal and superfluid phases can be quantitatively elucidated by the Biot model [6–9].

Silica aerogels are synthesized via a sol-gel process and hypercritical drying which enable the production of tenuous solids with porosity ϕ as large as 99.8% and unique acoustic properties. Silica aerogel is thought of as a network of nanoscale SiO_2 strands. The elastic moduli of aerogels are a few orders of magnitude smaller than that of bulk solids, and the sound speed substantially depends on the porosity. Ultrasound measurements have shown sound speeds as low as 20 m/s for the highest-porosity aerogel [10].

The high-porosity aerogels are so soft that the aerogel matrix and the clamped normal fluid move as the results of pressure and temperature gradients, unlike other porous media. This results in sound modes intermediate between first and fourth sound [11] and a second-like mode [12]. McKenna *et al.* [12] calculated the longitudinal sound velocity for the two modes using modified two-fluid hydrodynamic equations in order to take aerogel motion into consideration. They also observed the propagation of both the fast (intermediate between first and fourth sound) and the slow (second-like sound) modes in ^{4}He in aerogel from 1.1 K to T_c. They found agreement of the model with the observed sound velocity within the experimental temperature range.

¶ This article was submitted by the authors in English.

0021-3640/04/8002-0109$26.00 © 2004 MAIK "Nauka/Interperiodica"

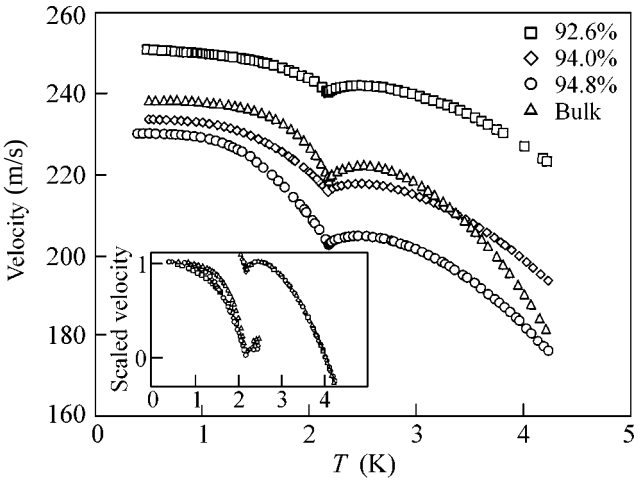

Fig. 1. Sound velocity for various aerogels as a function of temperature. That of bulk helium is also shown for comparison. The inset shows the scaled sound velocity. Velocity is scaled between 2.5 and 4.2 K, and 0.5 K and T_c, in the normal and the superfluid phase.

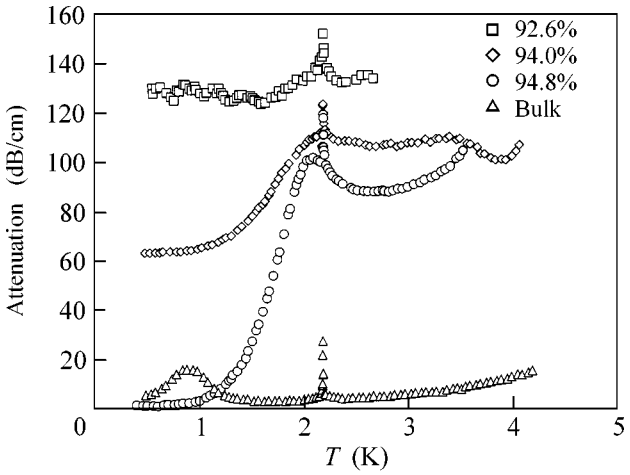

Fig. 2. Attenuation of sound for various aerogels as a function of temperature. That of bulk helium is also shown for comparison. For clarity, those for 94 and 92.6% are shifted +20 and +40 dB/cm, respectively. Those in the normal phase vary due to interference between the ultrasound signal and electrical feedthrough from the transducer and amplifier.

We have observed the 10-MHz longitudinal ultrasound signal with three different porosity (92.6, 94.0, and 94.8%) aerogels from 0.5 to 4.2 K and measured the sound velocity and attenuation in order to study sound propagation in the liquid-^{4}He-filled aerogel system in both the normal and superfluid phases. Preliminary results have been published elsewhere [13]. The viscous penetration depth of liquid ^{4}He at 10 MHz (about 40 nm) is estimated to be longer than the typical SiO_2 strand distance (about 10 nm for 98% aerogel and much shorter for 95%); thus, in the first approximation, the normal fluid in these systems is expected to be completely locked to the aerogel matrix by viscosity. The sound velocity of aerogel largely depends on the porosity, so that we can obtain an aerogel whose sound velocity is larger or smaller than that of bulk fluid. It is interesting to see what would happen if the relation of sound velocities between aerogel and fluid is counterchanged.

Three aerogels were grown by a sol-gel process from tetramethoxysilane (TMOS) as a one-step process. The porosities were determined using a standard dry weight method. We machined aerogels into cylinders (7 mm in diameter), which were enclosed in brass shells of 8.5 mm "outer" diameter and 3.0 mm length.

The porosity ϕ, superfluid transition temperature T_c, and sound velocity of aerogel u_a evaluated from the data in the normal phase

No.	ϕ (%)	T_c (K)	u_a (m/s)
1	92.6	2.165	256
2	94.0	2.168	212
3	94.8	2.168	181

The ends of the samples were polished flat and parallel. The sample cylinder was sandwiched between two $LiNbO_3$ transducers with springs. We used the same pair of transducers for every sample in order to easily compare the signal attenuation among aerogels. Aerogels were immersed in liquid ^{4}He at SVP. Temperatures were measured with a ruthenium oxide resistance thermometer and stabilized using a PI controller. The ultrasonic measurements were made using a standard pulse-transmission and a phase-sensitive detection technique.

We were able to observe the sound signal throughout the temperature range from 0.5 to 4.2 K. The transmitted sound signal through the aerogel in a vacuum, however, could not be observed because of the imperfect connection between the transducers and aerogel or large attenuation results from the aerogel.

Figures 1 and 2, respectively, show the sound velocity u and attenuation α for the three aerogels as a function of temperature; for comparison, those of bulk helium obtained in a different run were plotted as well. The superfluid transitions T_c were identified as a dip in velocity and by an absorption peak for each aerogel. Those in aerogels were as sharp as in bulk, which represented a homogeneous transition in aerogel. T_c in aerogels are listed in the table. The magnitude of T_c suppression and porosity dependence agree with specific heat measurement [1, 2].

The temperature dependence of the sound velocity is similar to that of bulk for each aerogel. The absolute value varies inversely to the porosity. In ordinary porous media, the sound velocity is modified by tortuosity and the acoustic index n decreases with increasing porosity. The absolute value varies in opposition to the porosity dependence of the acoustic index; thus, tortu-

osity may not explain the behavior but may still have an effect. The observed signal results from a compressional wave within liquid helium modified by aerogel.

The similarity of the temperature variation brings a scaled behavior to mind. Velocity for each aerogel and bulk liquid was scaled as $(u(T) - u(4.2\ \mathrm{K}))/(u(2.5\ \mathrm{K}) - u(4.2\ \mathrm{K}))$ and $(u(T) - u(T_c))/(u(0.5\ \mathrm{K}) - u(T_c))$ in normal and superfluid phase, respectively. The scaled temperature variations in the normal phase for each aerogel and for bulk liquid coincide with each other as shown in the inset of Fig. 1. This means the temperature variation is determined mainly by the bulk liquid. However, that in the superfluid phase depends on the porosity. We will discuss this behavior in detail below.

It is useful to compare it with the longitudinal sound velocity in ^{4}He-filled Vycor [4]. In the normal phase, the sound velocity in the Vycor system was almost constant, reflecting the constant sound velocity of Vycor glass. Contrary to the aerogel case, Vycor glass dominated the sound velocity of the composite system.

In a series of papers [6–9], Biot proposed a phenomenological theory of acoustic propagation in porous, fluid-filled, macroscopically homogeneous and isotropic media. In [14], Johnson applied Biot's theory for the superfluid ^{4}He in pores below 1.1 K, when the normal component can be neglected. In the case of silica aerogel filled with liquid ^{4}He, the parameters of that theory appear to be the tortuosity α, the aerogel porosity ϕ (fluid volume fraction), the density of liquid ^{4}He ρ_{He} and solid $\rho_{\mathrm{SiO_2}}$, the bulk modulus of helium K_{He}, the bulk modulus of silica $K_{\mathrm{SiO_2}}$, and the bulk modulus and the shear modulus of the aerogel structure itself K_a and N_a. At frequencies high enough that the viscous penetration depth is much smaller than the pore size, Biot argued that there are two (fast and slow) longitudinal modes in the composite system. The corresponding expressions for them can be found in [14]. In [15, 16], this theory has been generalized in the case of superfluid-saturated porous media, when all damping processes are neglected.

In the low-frequency limit, the expression for fast longitudinal sound velocity is given by

$$u_{\mathrm{fast}}^2 = \frac{(K_a + 4N_a/3) + (1/\phi)(1 - K_a/K_{\mathrm{SiO_2}})^2 K_{\mathrm{He}}}{\rho_a + \phi\rho_{\mathrm{He}}}. \quad (1)$$

In the normal phase, the relationship between the viscous penetration depth and pore size (in our case, the mean separation of SiO_2 strands) is questionable because of the complicated disorder structure of aerogel and the temperature dependence of liquid ^{4}He viscosity. That is why we have attempted to apply Biot's theory in both limit cases. The observed signal in the present study corresponds to the fast mode. In the high-frequency limit, the corresponding mechanical properties of aerogel and the complex system were evaluated by fitting the experimental data for each aerogel. We could fit the temperature dependence with this theory only if the coupling constant was nearly zero or even negative for each aerogel. As is shown by Johnson [14], n is given as square root of the coupling constant, so that this becomes nearly zero. According to this, n as evaluated by the Biot theory in high-frequency limit had no physical meaning. We should note here that the Biot theory is applicable mainly to a situation in which sound propagation is mainly determined by a solid and fluid provides a small perturbation to the system and works well in ^{4}He-filled Vycor [4] and alumina ceramics [5]. The equation which represents the sound velocity [14] has no analytical solution in the case when the sound velocity of solid and liquid is close. The aerogel–liquid ^{4}He system is actually this case. We concluded that the high-frequency limit of Biot's theory is not applicable to the aerogel–liquid ^{4}He case.

In the low-frequency limit, the mechanical properties of aerogel and the complex system can be evaluated by fitting formula (1) to the experimental data for every aerogel. But the structure of silica aerogel is still under study, and, in contrast to usual solids, there is no simple relationship between the bulk modulus and the shear modulus. Hence, the mentioned fitting procedure includes so many parameters in order to get aerogel sound velocity. That is why we present only a very simple phenomenological model for sound propagation in the normal phase; a more complicated theory has been published in [17]. Under the assumption that two different elastic media (the fluid and aerogel) are in parallel, the bulk modulus of the composite medium K_m can be estimated to be $\phi K_{\mathrm{He}} + K_a$ using that of the fluid K_{He} and aerogel K_a. The total density is expressed using the density of aerogel ρ_a, that of liquid helium ρ_{He}, and ϕ as $\rho_a + \phi\rho_{\mathrm{He}}$. Then, the sound velocity u is expressed as

$$u^2 = \frac{\phi K_{\mathrm{He}} + K_a}{\rho_a + \phi\rho_{\mathrm{He}}} = \frac{u_a^2\rho_a + \phi u_{\mathrm{He}}^2\rho_{\mathrm{He}}}{\rho_a + \phi\rho_{\mathrm{He}}}, \quad (2)$$

where u_a and u_{He} are the sound velocity of aerogel and that of liquid helium, respectively.

Equation (2) has been used to estimate the sound velocity of aerogel by fitting the temperature dependence of the observed sound velocity in the normal phase. The aerogel sound velocities are assumed to be constant with temperature, considering other experiments [18, 19]. The best fitting is obtained with the aerogel sound velocities, which are listed in the table. These values are consistent with the sound velocity obtained by Gross *et al.* [10]. We will use these values to analyze the sound mode in the superfluid phase.

For numerical calculations in the superfluid phase, we use two-fluid hydrodynamic equations which take into account the ability of aerogel to move. These equations were introduced for this case by McKenna *et al.* [12] and were investigated partially in [20]. Because of numerous mathematical errors in the last paper, the system of two-fluid hydrodynamic equations for the sound

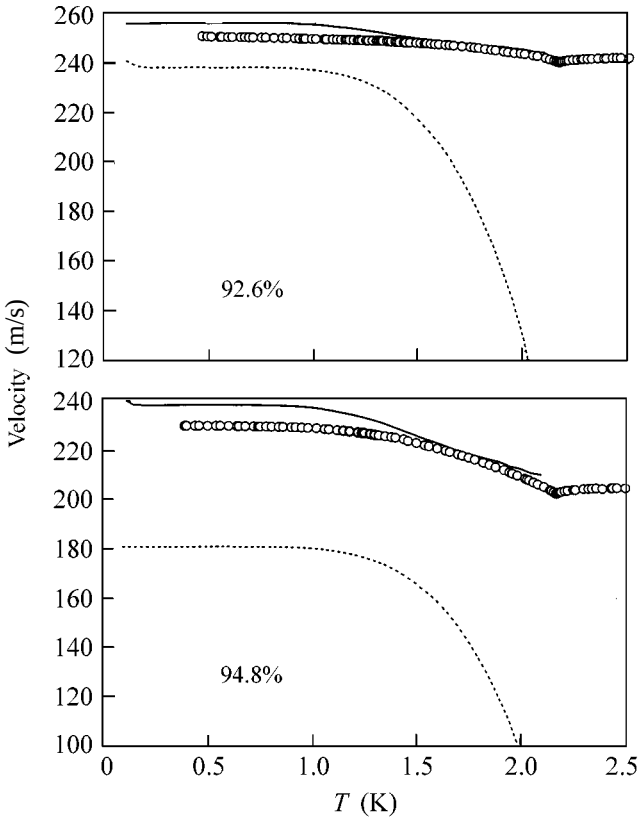

Fig. 3. Comparison between the observed sound velocity and that of the fast mode calculated by the hydrodynamic equations in the superfluid phase. Circles represent experimental points, and lines are theoretically calculated.

propagation in the liquid-^{4}He-filled silica aerogel has been rederived in the present study. In the notations of [20], it appears as

$$p'\left[-\frac{u^2}{u_1^2}+\frac{\rho_s\rho_{na}+\rho_n^2}{\rho\rho_{na}}\right]+T'\left[-u^2\frac{\partial\rho}{\partial T}-\frac{\sigma\rho_s\rho_a}{\rho_{na}}\right] + p_a'\frac{\rho_n}{\rho_{na}} = 0, \quad (3)$$

$$p'\left[-u^2\frac{1}{\rho}\frac{\partial\rho}{\partial T}-\frac{\sigma\rho_s\rho_a}{\rho_{na}}\right] + T'\left[-\frac{u^2}{u_2^2}\frac{\sigma^2\rho\rho_s}{\rho_n}+\frac{\sigma^2\rho_s(\rho+\rho_a)}{\rho_{na}}\right] + p_a'\frac{\sigma\rho_s}{\rho_{na}} = 0, \quad (4)$$

$$p'\frac{\rho_n\rho_a}{\rho\rho_{na}}+T'\frac{\sigma\rho_s\rho_a}{\rho_{na}}+p_a'\left[\frac{\rho_a}{\rho_{na}}-\frac{u^2}{u_a^2}\right] = 0. \quad (5)$$

By neglecting $\partial\rho/\partial T$, the secular equation for this system is reduced to the equation from [12]. Excluding p_a' from (5), we arrive at a two-equation system similar to the one obtained in [20], from which the sound conversion phenomena in superfluid ^{4}He in aerogel can be investigated. The numerical calculations of (3)–(5) give the sound velocity of the two modes, the fast and the slow ones. The velocities of the two sound modes calculated for 92.6 and 94.8% as above are shown in Fig. 3. The solid and dotted lines correspond to fast and slow mode, respectively. The sound velocity of these modes converges to that of bulk helium and aerogel, since there is neither normal component nor viscous coupling between the two media at low temperatures. The slow-mode velocity goes to zero at T_c. It is clearly shown that the experimentally observed sound mode corresponds to the fast mode; they agree well between 1 K and T_c for all aerogels. However, the discrepancy becomes significant below 1 K. The calculated fast mode converges to the greatest sound velocity in the composite system (for 94.0 and 94.8% aerogel, to bulk liquid velocity; for 92.6% aerogel, to aerogel sound velocity). On the other hand, the experimentally observed sound velocities at low temperature are lower than the calculated values. The porosity dependence of the velocity could not result from the tortuosity as in the case of normal phase. Then, the coupling between liquid and aerogel should be considered apart from viscosity of the normal fluid. We compared the mean free path of phonons and rotons and that determined geometrically by aerogel strands. The geometrically limited mean free path becomes shorter than that of phonons and rotons below 1 K. Acoustic phonons are thought to be scattered by aerogel strands and to give rise to the momentum transfer between aerogel and phonons. This means that the simple hydrodynamic theory is not applicable to this temperature range because there is no mechanism of momentum transfer due to there being no viscous fluid. A new theory is necessary in which momentum transfer between aerogel and phonon should be taken into account as in the case of the liquid ^{3}He–aerogel system [21]. We applied the simple idea used in the normal phase to sound velocity at low temperatures, because the ultrasound wavelength was long enough to regard the microstructure of aerogel as homogeneous and there was only one fluid component. The calculated sound velocities using (2) and aerogel sound velocities listed in the table are slower than experimental ones for all aerogels; this may result from weaker coupling compared to the normal phase. A detailed coupling mechanism seems necessary to fit the sound velocity at low temperatures.

The attenuations in the normal phase were so large that the attenuation variations are experimental artifacts resulting from inadvertent interference between the ultrasound signal and electrical feedthrough from the transducer and amplifier. There is no substantial porosity dependence in the normal phase. At T_c, a sharp absorption peak was observed for each aerogel, as was observed in the bulk liquid. In the specific heat mea-

surement [1, 2], two distinct singularities of specific heat were observed. The higher-temperature singularities were verified as coincident with the bulk liquid singularities. In our experiment, the absorption peak which corresponds to the T_λ was not observed for every aerogel. In fact, the temperature resolution of our experiment was not as good as the specific heat measurements [1, 2] but was adequate to distinguish between the peaks at T_c and T_λ. In the sound experiment, the attenuation due to the bulk liquid may be obscured by the large attenuation of the aerogel.

The observed constant attenuation in the superfluid phase below 1 K strongly depends on the porosity (or, in other words, on the density of SiO_2 strands that act as scattering centers), and there is no temperature-dependent contribution from phonons and rotons. This behavior qualitatively agrees with the geometrically limited mean free path picture.

The absorption peak around 1 K which is observed in bulk liquid was not observed in the aerogel system. In the bulk liquid, the absorption peak is due to the phonon–roton interaction and the peak appears at the temperature that corresponds to $\omega\tau \sim 1$, where ω is the angular frequency of sound and τ is the relaxation time. The absence of the attenuation peak is considered to be explained as follows. The phonon mean free path increases with decreasing temperature and finally exceeds the geometrically limited mean free path in the aerogel. The relaxation time is limited by the aerogel and cannot satisfy the relation $\omega\tau \sim 1$, so that the attenuation peak is not observed. Similar peak suppression has been observed in the ^{4}He–^{3}He mixture [22], where the existence of ^{3}He excitations means that there will be more collisions, or, in other words, τ is smaller than that in pure ^{4}He. The peak of the attenuation occurs at lower temperatures compared to pure ^{4}He. Because of the lower temperature, the number of phonons and rotons is lower and the value of the peak attenuation is reduced compared to that of bulk ^{4}He. The same scenario may work in the aerogel–^{4}He system.

In conclusion, we have studied the low-temperature acoustic properties of a liquid-^{4}He-filled aerogel system for aerogels of various porosities and observed a compressional wave in both the normal and the superfluid phase using 10 MHz ultrasound. It has been found that sound velocity and attenuation are strongly influenced by aerogel. The scaling behavior has been found in the normal phase. In the superfluid phase, the two sound modes are calculated from the hydrodynamic model and the observed sound mode has been shown to correspond to the fast mode. The attenuation peak due to the phonon–roton interaction has not been observed in the present system. The geometrical limited phonon mean free path by aerogel strand seems to play an important role in the acoustic properties at low temperature. More detailed theoretical consideration is in progress [17].

This work was partially supported by a Grant-in-Aid for Scientific Research from the Ministry of Education, Culture, Sports, Science, and Technology of Japan, by the Russian Foundation for Basic Research (grant no. 02-04-16800), by the Program "Universities of Russia" (grant no. 01.01.010), by CRDF (grant no. REC-007), and by the Tatarstan Academy of Sciences (grant no. 06-6.2-291). The authors would like to express their appreciation to H. Suzuki and S. Abe for their useful discussions. They also wish to thank T. Higaki for his contribution to the early stage of this study.

REFERENCES

1. G. K. S. Wong, P. A. Crowell, H. A. Cho, and J. D. Reppy, Phys. Rev. Lett. **65**, 2410 (1990).
2. J. Yoon, D. Sergatskov, J. Ma, *et al.*, Phys. Rev. Lett. **80**, 1461 (1998).
3. I. M. Khalatnikov, *An Introduction to the Theory of Superfluidity* (Nauka, Moscow, 1965; Addison-Wesley, Redwood City, 1988).
4. J. R. Beamish, A. Hikata, and C. Elbaum, Phys. Rev. B **27**, 5848 (1983).
5. K. Warner and J. R. Beamish, Phys. Rev. B **50**, 15896 (1994).
6. M. A. Biot, J. Acoust. Soc. Am. **28**, 168 (1956); J. Acoust. Soc. Am. **28**, 179 (1956).
7. M. A. Biot, J. Appl. Phys. **33**, 1482 (1962).
8. M. A. Biot, J. Acoust. Soc. Am. **34**, 1254 (1962).
9. M. A. Biot and D. G. Willis, J. Appl. Mech. **24**, 594 (1957).
10. J. Gross, J. Fricke, and L. W. Hrubesh, J. Acoust. Soc. Am. **91**, 2004 (1992).
11. M. J. McKenna, T. Slawecki, and J. D. Maynard, Physica B (Amsterdam) **165–166**, 581 (1990).
12. M. J. McKenna, T. Slawecki, and J. D. Maynard, Phys. Rev. Lett. **66**, 1878 (1991); Their early work is reported as K. L. Warner and J. R. Beamish, Phys. Rev. B **36**, 5698 (1987).
13. K. Matsumoto, O. Arai, Y. Okuda, and K. Tajiri, Physica B (Amsterdam) **284–288**, 101 (2000); K. Matsumoto, T. Higaki, Y. Matsuyamaa, and K. Tajiri, Physica B (Amsterdam) **329–333**, 335 (2003).
14. D. L. Johnson, Appl. Phys. Lett. **37**, 1065 (1980).
15. T. Buishvili, Sh. Kekutia, O. Tkeshelashvili, and L. Tkeshelashvili, Phys. Lett. A **300**, 672 (2002).
16. Sh. Kekutia and N. D. Chkhaidze, Low Temp. Phys. **28**, 795 (2002).
17. D. Tayurskii and K. Matsumoto, Solids Electron. J. **6**, 213 (2004); http://mrsej.ksu.ru.
18. Y. Xie and J. R. Beamish, Phys. Rev. B **57**, 3406 (1998).
19. D. R. Daughton, J. MacDonald, and N. Mulders, Physica B (Amsterdam) (in press).
20. P. Brusov, J. M. Parpia, P. Brusov, and G. Lawes, Phys. Rev. B **63**, 140507 (2001).
21. T. Ichikawa, M. Yamamoto, S. Higashitani, and K. Nagai, J. Phys. Soc. Jpn. **70**, 3483 (2001).
22. G. O. Harding and J. Wilks, Proc. R. Soc. London, Ser. A **268**, 424 (1962).

JETP Letters, Vol. 80, No. 2, 2004, pp. 114–119. Translated from Pis'ma v Zhurnal Éksperimental'noĭ i Teoreticheskoĭ Fiziki, Vol. 80, No. 2, 2004, pp. 124–129.

Indirect ^{207}Pb–^{207}Pb and ^{17}O–^{207}Pb Nuclear Spin–Spin Interactions in the Metallic Phase of $BaPb_{1-x}Bi_xO_3$ Oxides

A. V. Pogudin[1], V. V. Ogloblichev[1], Yu. V. Piskunov[1], A. P. Gerashchenko[1], S. V. Verkhovskiĭ[1,*], A. Yu. Yakubovskiĭ[2], and A. Trokiner[3]

[1] *Institute of Metal Physics, Ural Division, Russian Academy of Sciences, Yekaterinburg, 620219 Russia*
**e-mail: verkhovskii@imp.uran.ru*
[2] *Russian Research Centre Kurchatov Institute, pl. Kurchatova 1, Moscow, 123182 Russia*
[3] *Laboratoire de Physique du Solide, ESPCI, 75231 Paris, France*

Received June 3, 2004

A ^{207}Pb spin echo signal and a ^{17}O–^{207}Pb spin echo double resonance signal were measured in the metallic phase of $BaPb_{1-x}Bi_xO_3$ oxides ($x < 0.15$). Constants of indirect homonuclear (^{207}Pb–^{207}Pb) and heteronuclear (^{17}O–^{207}Pb) couplings of nuclear spins through the conduction electron system were determined. Evidence was obtained for the development of a microscopically nonuniform spin-density distribution in Bi-containing oxides. © *2004 MAIK "Nauka/Interperiodica".*

PACS numbers: 76.60.Lz; 31.30.Gs

In recent years, the effect of static and dynamic charge nonuniformity in the sublattice of $Pb(Bi)O_6$ octahedra on the electron states of the conduction band of the $BaPb_{1-x}Bi_xO_3$ oxide has been widely discussed [1–3]. The region of superconducting compositions ($0.1 < x < 0.35$) of the metallic phase is adjacent to the concentration ($x_c \approx 0.35$) transition to the semiconducting state of the oxide with an energy gap reaching, according to electron transport data, the value $\Delta \cong 0.3$ eV in $BaBiO_3$ [4]. The relatively low carrier density ($\sim 10^{21}$ cm^{-3}) and charge fluctuations associated with the ambiguity of the valence state of bismuth ions ($Bi^{4+\delta}/Bi^{4-\delta}$) can be favorable to the development of an instability in the state of the electron system in metallic-phase oxides that is uniform over the crystal. The data of measuring the magnetic susceptibility [1] and the mean shift of the ^{207}Pb and ^{17}O NMR lines [5] indicate that the density of states at the Fermi level $N(E_F)$ grows monotonically as the metal–semiconductor transition is approached. Along with the growth of the mean Knight shift $\langle K \rangle$, which is proportional to the uniform ($q = 0$) contribution to the spin susceptibility χ_s, an increase in the width of the shift distribution ΔK has been noted. This width reaches the value of the shift $\langle K \rangle$ itself (Fig. 1). A detailed analysis of the variations of the shape of the magnetic spectral broadenings with the concentration x provided evidence that the local spin susceptibility χ_s grows anomalously in the regions containing Bi atoms with characteristic sizes no higher than the doubled parameter a of the pseudocubic perovskite unit cell [5]. The percolation overlap of such regions should be expected in superconducting compositions of the oxide ($x > 0.12$).

In this work, data on the spatial dispersion $\chi_s(q)$ in the metallic phase of $BaPb_{1-x}Bi_xO_3$ ($x < 0.15$) oxides were obtained from measurements of the indirect Pb–Pb (^{207}J) and O–Pb (^{17}J) nuclear coupling constants and the decay rate of the spin echo signal (T_2^{-1}) of ^{207}Pb as a result of ^{207}Pb spin echo and ^{17}O–^{207}Pb spin echo double resonance (SEDOR) experiments,

$$^{207}\text{Pb}–^{207}\text{Pb}.$$

In the metallic phase, the conduction-band states are formed with the participation of Pb(Bi) 6*s* orbitals. The positive sign of the isotropic part of the ^{207}K Knight shift [5] allows the Fermi contact interaction to be considered as the main hyperfine interaction of ^{201}S nuclei ($S = 1/2$) with conduction band electrons (σ) of the oxide

$$\begin{aligned} H_{\text{en}} &= (8\pi/3)\gamma_S\gamma_{el}\hbar^2(\sigma\mathbf{S})\langle|U_{6s}(r=0)|^2\rangle_{EF} \\ &= -\gamma_S\hbar H_{hf}(\sigma\mathbf{S}), \end{aligned} \quad (1)$$

where $^{207}H_{hf}$ is the contact hyperfine field generated on nuclei S by spin $\sigma = 1/2$ and γ_S is the gyromagnetic ratio of the ^{207}Pb. The high value of $^{207}H_{hf}$ leads to the fact that the nuclear spin–spin interaction of heavy lead atoms ($z = 82$) is mainly determined by the scalar indirect interaction through conduction electrons $\hbar\Sigma_{i<j}^{207} J_{ij}(\mathbf{S}_i, \mathbf{S}_j)$, which substantially exceeds the dipole interaction of the magnetic moments of lead nuclei in intensity. Given the local magnetic nonuniformities $\hbar\Sigma_i \delta\omega_i S_{iz}$, which lead to an inhomogeneously broadened ^{207}Pb NMR line ($^{207}\text{Pb}(|\delta\omega_i - \delta\omega_j| \gg |^{207}J_{ij}|)$), the

scalar indirect interaction of nuclear spins $\mathbf{S}_i(\mathbf{r}_i)$ and $\mathbf{S}_j(\mathbf{r}_j)$ of one sort separated from each other by the distance $\mathbf{R}_{ij} = \mathbf{r}_i - \mathbf{r}_j$ is determined by the secular part and has the form

$$H_{\text{ind},ij} = \hbar^{207}J_{ij}S_{iz}S_{jz} = \gamma_S^2\hbar^2H_{hf}^2(6s)\chi_s'(\mathbf{R}_{ij})S_{iz}S_{iz}. \quad (2)$$

The indirect coupling constant $^{207}J_{ij}$ is related to the actual part of the nonlocal spin susceptibility $\chi_s'(\mathbf{R})$, which in turn has the following form for the electron gas in a metal in units of electron density of states:

$$\begin{aligned}\chi_s'(\mathbf{R}) &= N(E_F)\Sigma_{q>0}F_L(q)\exp(-i\mathbf{qR}) \\ &= N(E_F)\mathbf{\Phi}(\mathbf{R}),\end{aligned} \quad (3)$$

where $F_L(q)$ is the Lindhard function, which determines the static permittivity of the metal, and $N(E_F)$ is the density of states at the Fermi level.

^{207}Pb spin echo experiments were carried out in the temperature range (10–100) K in the magnetic field $H_0 \sim$ 94 kOe with single-phase polycrystalline $BaPb_{1-x}Bi_xO_3$ samples (x = 0.00, 0.09, and 0.12) differing in the concentration of the NMR lead isotope ^{207}C = 0.226 and 0.95. The synthesis and the detailed structural characterization of the samples were described previously in [5, 6]. The spin echo signal $E(2t)$ was formed with the use of a $\pi/2$–t–π–t–echo sequence of two coherent radio-frequency pulses generating an alternating magnetic field with a circular component amplitude $H_1 \sim 200$ Oe in the resonance coil with a sample. The duration of the $\pi/2$ pulse, which performs a rotation in the spin space of S spins by an angle of $\pi/2$, did not exceed 1.4 μs. This allowed the sign of the nuclear spin polarization to be inverted within the linewidth in the starting $BaPbO_3$ oxide and various regions of the significantly wider NMR spectrum in oxides with $x > 0$ to be selectively excited.

The spin echo signal $E(2t) \sim \text{Sp}\{\rho(2t)S_x\}$ reaches a maximum at the instant of time $2t$. The density matrix $\rho(t)$ of the spin system (S), which describes the time evolution of the spin operators $S_x = \Sigma_j S_{jx}$ in the rotating (ω_{0S}) coordinate system, $\rho(t-0) \sim S_z$. At the instant of time $2t$, the density matrix $\rho(t)$ has the form [7]

$$\begin{aligned}\rho(2t) \sim \exp(-iHt)\exp(-i\hat{H}t)S_x \\ \times \exp(i\hat{H}t)\exp(iHt),\end{aligned} \quad (4)$$

$$H = \hbar\Sigma_i\delta\omega_iS_{iz} + \hbar\Sigma_{i<j}^{207}J_{ij}S_{iz}S_{jz}, \quad (5)$$

where $\hat{H} = R(\pi)$, $H = R^{-1}(\pi)$ is the Hamiltonian of spin–spin interactions of lead nuclei transformed as a result of the action of the second π pulse at the instant of time t and $R(\pi)$ is the operator of the corresponding unitary transformation. According to Eqs. (4) and (5), only the secular part of the indirect interaction, which is the quadratic form in the spin Hamiltonian (Eq. (5)), determines the behavior of $E(2t)$ as a function of the time interval t between the pulses forming the echo signal [7–9]

$$E(2t) \sim \Pi_{i,j}\cos(J_{ij}t). \quad (6)$$

At starting times ($J_{ij}t < 1$), the variation of the echo amplitude $E(2t)$ follows a Gaussian curve with the characteristic decay rate [7]

$$T_{2,\text{gauss}}^{-1} = \{^{207}c1/3S(S+1)\Sigma_j(^{207}J_{ij})^2\}^{1/2} \quad (7)$$

proportional to the contribution of the indirect nuclear interaction to the homogeneous ^{207}Pb NMR linewidth. From the $E(2t)$ data given in Fig. 2 for oxides with x = 0 and 0.09, it is evident that the irreversible echo decay rate is high. Its value T_2^{-1} (^{207}c = 0.226) = 18(3) ms^{-1}) considerably exceeds the contribution determined by the dipole interaction of nuclear magnetic moments $(T_2^{-1})_{\text{dip}}(^{207}c = 0.226) \approx 0.3$ ms^{-1}. This justifies the use of the spin–spin interaction Hamiltonian of lead nuclei in form (5). Moreover, for the starting $BaPbO_3$ oxide, it is found that the value of T_2 does not depend on temperature in the region $T < 100$ K and also remains constant as the amplitude of the radio-frequency field in the pulse decreases to $H_1 \sim 50$ Oe.

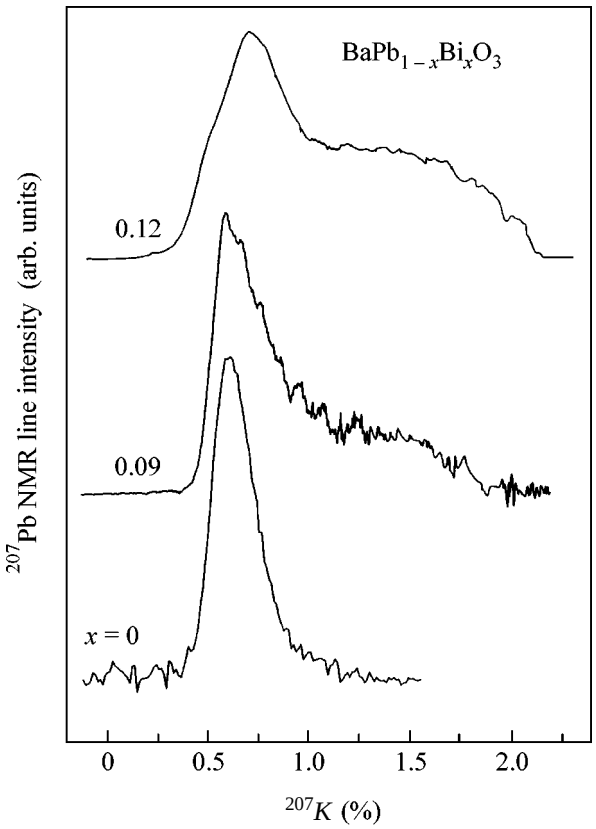

Fig. 1. NMR spectra of ^{207}Pb in the metallic phase of $BaPb_{1-x}Bi_xO_3$ oxides at T = 20 K. $^{207}K_s$ is the Knight shift.

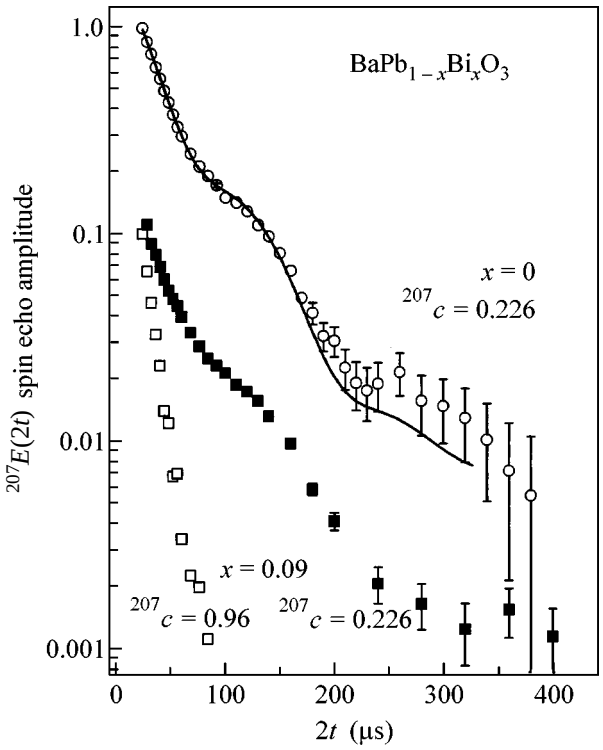

Fig. 2. Spin echo amplitude decay for lead nuclei $^{207}E(2t)$ in $BaPb_{1-x}Bi_xO_3$ oxides with increasing time delay interval t in the pulse sequence $\pi/2$–1–π forming the echo signal in a magnetic field of 94 kOe at $T = 20$ K: (○) $x = 0.00$ and $^{207}c = 0.226$, (■) $x = 0.09$ and $^{207}c = 0.226$, and (□) $x = 0.09$ and $^{207}c = 0.96$. Solid line is the result of an approximation of the $^{207}E(2t; x = 0.00)$ data using the expression in the form $\exp(-2t/T_2)\cos(2\omega_{osc}t)$.

When the time interval $2t$ for the oxides with the natural concentration of the NMR isotope ($^{207}c = 0.226$) studied in this work was extended, oscillations were detected in the decay of the spin echo amplitude. The modulated behavior of $E(2t)$ was satisfactorily approximated by the expression of the form

$$E(2t) \propto \exp\left(\frac{-2t}{T_2}\right)(1 + a\cos(\omega_{osc}2t)), \qquad (8)$$

which contained only one harmonic with the frequency ω_{osc}. The result of the approximation for $x = 0.00$ is shown by a solid line in Fig. 2 with the parameters $T_2 = 45(5)$ μs and $\omega_{osc} = 45(5) \times 10^3$ s^{-1}. If the NMR ^{207}Pb isotope is randomly distributed over the positions of lead atoms in the oxide, the oscillating contribution $E(2t)$ is due to the factor $\cos(J_{1nn}t)$ with the maximum constant $^{207}J_{1nn} = 2\omega_{osc} = 90(10) \times 10^3$ s^{-1}, which corresponds to a pair of neighboring spins $\mathbf{S}_1$ and $\mathbf{S}_2$ separated by the minimum possible distance ($R_{12} = a$) and coupled with each other by an indirect interaction through conduction electrons. Thus, the observation of oscillations of the echo amplitude allowed a direct estimate to be obtained for the indirect nuclear spin-spin coupling constant of neighboring lead atoms in oxides. The corresponding theoretical estimation of $^{207}J_{1nn}$ performed for $BaPbO_3$ within the Ruderman–Kittel model [7, 10] using Eqs. (2) and (3) at $2k_Fa = 0.75\pi$ [11] and $^{207}H_{hf} = 4.2(4) \times 10^6$ Oe [12] gives the value of the constant $^{207}J_{1nn,\,calc} = 95 \times 10^3$ s^{-1}, which is surprisingly close to that obtained from measurements of the frequency of $E(2t)$ oscillations. Estimations of the indirect coupling constants for more distant Pb atoms located in the second ($^{207}J_{2nn,\,calc} = 20 \times 10^3$ s^{-1}) and third ($^{207}J_{3nn,\,calc} \approx 9 \times 10^3$ s^{-1}) cation spheres performed using the same approach point to the short-range character of the indirect interaction between lead nuclei in the oxide.

With increasing ^{207}c, the decay of the echo amplitude acquires an aperiodic character. Simultaneously, the decay rate increases. The ratio of the echo decay rates measured for two oxide samples with $x = 0.09$ differing in the concentration of the ^{207}Pb isotope (Fig. 2)

$$\frac{T_2^{-1}(^{207}c = 0.95)}{T_2^{-1}(^{207}c = 0.226)} = 2.5(6)$$

is in good agreement with the increase in $T_2^{-1} \sim (^{207}c)^{1/2}$ by a factor of 2.2 in the more enriched sample as expected according to Eq. (7). The restriction associated with the so-called "dead time" of the reception path of the pulse NMR spectrometer prevented the initial evolution of $E(2t)$ from being followed in detail at $t < 8$ μs. In the results given below, the value of T_2 was estimated as the time interval in the course of which the echo amplitude decreased by a factor of e, assuming an exponential form of the decay $E(2t) \sim \exp(-2t/T_2)$). In defense of the selected measurement procedure, it should be noted that the calculation of the contribution of H_{ind} to the second moment of the ^{207}Pb NMR line leads for $BaPbO_3$ to the estimate $T_{2,\,calc} = 1.4T_{2,\,gauss} \approx 35$ μs, which is rather close to the measured value $T_2 = 45(5)$ μs.

Figure 3 gives the values of the $^{207}J_{1nn}$ constant (□) and the characteristic echo decay time $^{207}T_2^{-1}$ (■) measured for the $BaPb_{0.88}Bi_{0.12}O_3$ oxide in the regions of the inhomogeneously broadened line differing in the Knight shift $^{207}K_s$. The growth of $^{207}J_{1nn} \sim K_s$ according to Eq. (2) points to the fact that the nearest neighboring lead atoms determining the oscillating contribution to the decay of the echo amplitude $E(2t)$ are located in the region with a close value of the local spin susceptibility $\chi_{s,\,loc} \sim K_s$. On the other hand, for oscillations to appear, it is necessary that the resonance frequencies ($\delta\omega_i - \delta\omega_j$) excited by the radio-frequency pulse of a pair of "similar" neighboring spins S_i and S_j should be different: $|(\delta\omega_i - \delta\omega_j)| \gg |^{207}J_{1nn}|$ [7–9]. The difference in the

resonance frequencies is due to the change $\Delta\chi_{s,\,\mathrm{loc}}$ in the local spin susceptibility of the oxide conduction band electrons. Its relative change $|\Delta\chi_{s,\,\mathrm{loc}}|/\chi_s(q=0)$ at a distance of the order of the interatomic distance $|\Delta\chi_{s,\,\mathrm{loc}}|/\chi_{s,\,\mathrm{loc}} \gg \max|^{207}J_{1nn}|/\langle K_s\rangle\omega_0 \approx 0.07$ is a lower estimate of the characteristic microinhomogeneities in the ground state of the electron system in the $BaPb_{0.88}Bi_{0.12}O_3$ oxide. It was revealed previously that an increase in the short-wavelength contributions to χ_s compared to its mean value over the crystal occurs in the crystal microregions containing Bi [5]. ^{207}Pb spin echo experiments provided direct evidence in favor of the microscopic character of the inhomogeneous state of the electron system in oxide samples for which, according to x-ray diffraction data, there is no indications of macroscopic phase separation.

^{17}O–^{207}Pb.

The magnetic nonuniformity developed in $BaPb_{1-x}Bi_xO_3$ oxides at $x \geq 0$ is also manifested in the distribution of ^{17}O NMR line shifts [5]. Oxygen atoms in the $BaPb_{1-x}Bi_xO_3$ compound are located at the vertices of the octahedra at the center of which Pb(Bi) cations are located. The ^{17}O isotope nucleus has spin $^{17}I = 5/2$ and electric quadrupole moment $^{17}Q = -0.27 \times 10^{-25}$ cm^2. As a result, the resonance frequency of ^{17}O is determined not only by the hyperfine magnetic interactions, as is the case with lead atoms, but also by the interaction H_Q of the quadrupole moment of the nucleus with the electric field gradient eV_{ii} induced by the electron and ion environment. At small Bi concentrations, the symmetry of the charge environment of oxygen atoms is close to axial. Therefore, for polycrystalline samples, the NMR line of the central transition $m = 1/2 \longleftrightarrow -1/2$ in the strong magnetic field $\mu_I H_0 \gg |H_Q|$ has a characteristic double-humped shape (Fig. 4a) due to the quadrupole splitting $\sim|H_Q|^2/\mu_I H_0$. For the $BaPbO_3$ composition, the spectrum is satisfactorily described under the assumption that the positions of oxygen atoms in the crystal are magnetically equivalent. In the $BaPb_{0.91}Bi_{0.09}O_3$ composition, the magnetic equivalence of the positions of oxygen atoms is disturbed. The spectrum of the central transition measured at room temperature (Fig. 4b) exhibits a fine structure. At the ^{17}O isotope concentration $^{17}c \approx 0.15$, the fine structure of lines and the relaxation properties of ^{17}I nuclei are due to the distribution of local magnetic fields generated by the neighboring Pb(Bi) cations. Correspondingly, the heteronuclear interaction H_{IS} between the nuclear spin I and the spins S belonging to heavier Pb(Bi) atoms involves two main contributions:

$$H_{IS} = \Sigma_j\{\gamma_I\gamma_S\hbar^2/2r_j^3\}(3\cos^2\theta_j - 1)I_zS_{jz} + \Sigma_j\hbar\,{}^{17}J_{1j}I_zS_{jz}. \quad (9)$$

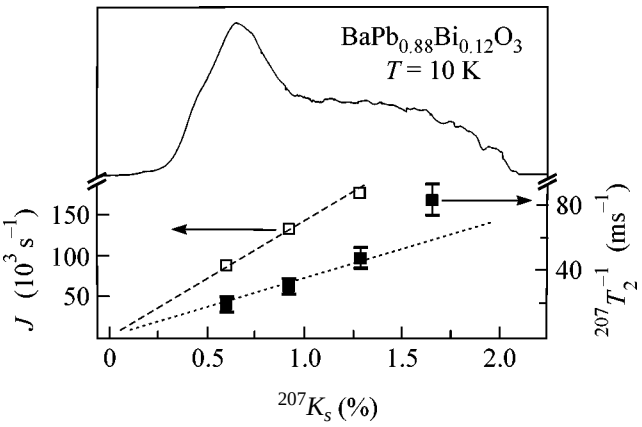

Fig. 3. Indirect nuclear ^{207}Pb coupling constant $^{207}J_{1nn}$ for the nearest neighboring lead cations and the irreversible spin echo decay rate $^{207}T_2^{-1}$ as functions of the Knight shift $^{207}K_s$ in $BaPb_{0.88}Bi_{0.12}O_3$. The data correspond to the regions (K_s) of the inhomogeneously broadened ^{207}Pb NMR line presented in the upper part of the figure.

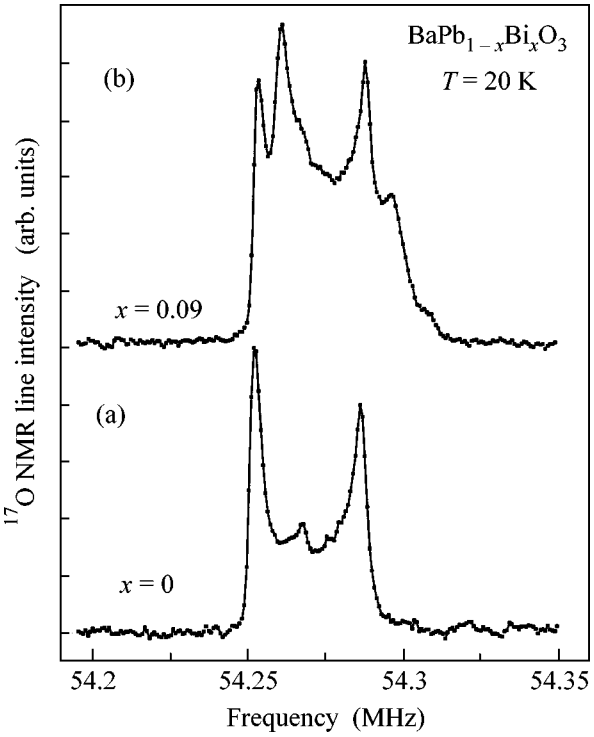

Fig. 4. ^{17}O NMR spectra in $BaPb_{1-x}Bi_xO_3$ oxides of the metallic phase with $x = 0.00$ and 0.09. Measurements were performed in a magnetic field of 94 kOe at $T = 20$ K. The position of the ^{17}O NMR line peak in H_2O corresponds to a frequency of 54.270 MHz.

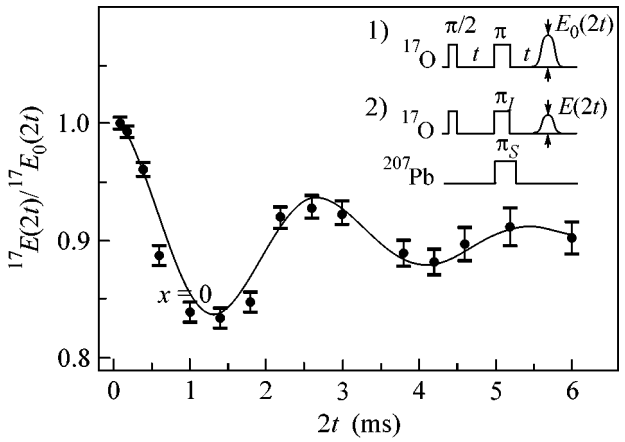

Fig. 5. SEDOR signal $m(2t) = {}^{17}E(2t)/{}^{17}E_0(2t)$ in the $BaPbO_3$ oxide at $T = 20$ K; solid line is the result of an approximation of the $m(2t)$ data by the expression in the form $m(2t) \sim \exp(-2t/T_2)\cos(\omega_{osc}2t) + c$. The inset in the upper part of the figure displays the sequence of radio-frequency pulses exciting the $I(^{17}O)$ and $S(^{207}Pb)$ spin systems in the course of SEDOR experiments.

The first term in Eq. (9) takes into account the classical dipole interaction of the magnetic moments of the I and S spins having different Larmor frequencies ω_{0I} and ω_{0S}, respectively. The dipole contribution depends on the angle θ between the magnetic field direction and the vector $\mathbf{r}$ connecting the interacting nuclei of O and Pb atoms. The second term describes the indirect interaction $H_{IS,\,ind}$ of the nuclear spins I and S. This interaction is assumed to be isotropic, because, as was found previously in [5], the anisotropy of hyperfine magnetic interactions of oxygen in the oxide is insignificant ($|{}^{17}K_{anis}|/|{}^{17}K_{iso}| \sim 0.1$). The following equation can be written for the ${}^{17}J_{1j}$ constant:

$$^{17}J_{1j} = \gamma_I\gamma_S\hbar\Sigma_j^{17}H_{hf}^{207}H_{hf}\chi'(\mathbf{r}_j), \qquad (10)$$

where ${}^{17}H_{hf} = 80(10)$ kOe is the transferred hyperfine field induced on the ${}^{17}I$ nucleus [5, 12] by the neighboring cation environment.

In contrast to lead, the characteristic time ${}^{17}T_2 = (0.5–4)$ ms of the decay of the spin echo signal of oxygen nuclei ${}^{17}E(2t)$ is mainly determined by time fluctuations of the z components of the local fields associated with the flip–flop processes of spin–lattice relaxation ($T_1 \sim T^{-1}$) in the spin dynamics of spins S of the neighboring cations. The evolution of the nuclear magnetization of spins I under the action of the static part of the heteronuclear interaction given by Eq. (10) was investigated in the course of ${}^{17}O$–${}^{207}Pb$ SEDOR experiments [7, 13] in the region of low temperatures $T \le 20$ K, where the inequality ${}^{17}T_2 \le {}^{207}T_1$ was true. The SEDOR experiments were performed in two stages. At the first stage (the inset in Fig. 5), a sequence of radio-frequency pulses $(\pi/2)_I - t - \pi_I$ was applied to spins I at the frequency $\omega_{0I}/2\pi = 56.4$ MHz. Then, at the instant of time $2t$, the spin echo amplitude ${}^{17}E_0(2t)$ was measured. Because the Hamiltonian in Eq. (10) does not explicitly depend on time in the $(0; 2t)$ interval, the action of the π_I pulse gives $H_{IS}(t - 0) = -H_{IS}(t + 0)$. In this case, the effect of the defocusing of the nuclear magnetization of spins I in the static local fields of spins S in the $(0; t)$ interval is accompanied by the subsequent refocusing of the nuclear magnetization of spins I in the $(t; 2t)$ interval, which precedes the formation of the echo signal. At the second stage, simultaneously with the π_I pulse, an additional π_S pulse is applied at the frequency $\omega_{0S}/2\pi = (84–86)$ MHz. This pulse inverts the direction of the local fields generated by spins S and retains the sign of $H_{IS}(t - 0) = H_{IS}(t + 0)$ unchanged in the course of the evolution time $2t$. As a result, the spin echo amplitude ${}^{17}E(2t)$ at the moment $2t$ must decrease compared to ${}^{17}E_0(2t)$ because of the additional decay introduced at the second stage by H_{IS}, whose time dependence was monitored in the experiment. The SEDOR signal m is determined by the ratio $m(2t) = {}^{17}E(2t)/{}^{17}E_0(2t)$. The results of measuring $m(2t)$ at $T = 20$ K for a polycrystalline sample of the starting $BaPbO_3$ oxide ($^{207}c = 0.226$; $^{17}c \approx 0.15$). The dependence $m(2t)$ has a well-defined oscillating character with the frequency $\omega_{osc,\,exp}/2\pi = 350(20)$ Hz, which is expected for almost isolated ${}^{17}O$–${}^{207}Pb$ pairs of nuclei at small concentrations of NMR isotopes excited in SEDOR.

An estimation of the heteronuclear dipole interaction in Eq. (9) for a pair of the nearest O–Pb neighbors leads to a contribution to the SEDOR signal oscillating with the frequency $\omega_{osc,\,dip}/2\pi = 180$ Hz, which is half as large as the frequency observed experimentally. The difference $\omega_{osc,\,exp} - \omega_{osc,\,dip} = \omega_{osc,\,ind} = 1070(100)$ s^{-1} corresponds to the oscillation frequency of the SEDOR signal associated with the contribution of the indirect nuclear ${}^{17}O$–${}^{207}Pb$ interaction of the nearest neighboring oxygen and lead atoms in the oxide structure. The corresponding indirect nuclear coupling constant of the neighboring O–Pb atoms equals twice the value of $\omega_{osc,\,ind}$ and comprises ${}^{17}J_{1nn} = 2140(200)$ s^{-1}. It is interesting to note that the ratio of the measured constants $|{}^{207}J_{1nn}/{}^{17}J_{1nn}| = 40(10)$ is very close to the ratio of the corresponding hyperfine fields ${}^{207}H_{hf}/{}^{17}H_{hf} = 50$ [5]. This in many instances justifies the form of the indirect interactions of ${}^{17}O$ and ${}^{207}Pb$ nuclei considered above for the metallic phase of $BaPb_{1-x}Bi_xO_3$ oxides.

Thus, the results of measurements and the subsequent analysis of the irreversible decay of the Pb spin echo signal and the ${}^{17}O$–${}^{207}Pb$ SEDOR signal presented in this article revealed specific features of the indirect homonuclear (${}^{207}Pb$–${}^{207}Pb$) and heteronuclear (${}^{17}O$–${}^{207}Pb$) spin–spin interactions through the conduction

electron system for the metallic phase of $BaPb_{1-x}Bi_xO_3$ oxides. Direct estimations of the indirect coupling constants for the nearest neighboring O–Pb and Pb–Pb atoms provide convincing evidence in favor of the development of the ground state of the electron system in the metallic phase of the oxides that is microscopically nonuniform over the crystal.

This work was supported by the Russian Foundation for Basic Research, project no. 02-02-17762.

REFERENCES

1. S. Uchida, H. Hasegawa, K. Kitazawa, and S. Tanaka, Physica C (Amsterdam) **156**, 157 (1988).
2. U. Hahn, G. Vielsack, and W. Weber, Phys. Rev. B **49**, 15936 (1994).
3. T. Rice and L. Sneddon, Phys. Rev. Lett. **47**, 689 (1981).
4. S. Uchida, H. Namatame, C. Fuggle, *et al.*, Phys. Rev. B **48**, 16917 (1993).
5. Yu. Piskunov, A. Gerashenko, A. Pogudin, *et al.*, Phys. Rev. B **65**, 134518 (2002).
6. K. Kumagai, Yu. Piskunov, Yu. Zhdanov, *et al.*, Physica C (Amsterdam) **274**, 209 (1997).
7. C. R. Slichter, *Principles of Magnetic Resonance*, 3rd ed. (Springer, New York, 1996; Mir, Moscow, 1967).
8. H. Alloul and C. Froidevaux, Phys. Rev. **163**, 324 (1967).
9. C. Froidevaux and M. Weger, Phys. Rev. Lett. **12**, 123 (1964).
10. J. Winter, *Magnetic Resonance in Metals* (Clarendon Press, Oxford, 1971; Mir, Moscow, 1976).
11. K. Kitazawa, M. Naito, and T. Itoh, J. Phys. Soc. Jpn. **54**, 2682 (1985).
12. Yu. V. Piskunov, A. Yu. Yakubovskiĭ, A. V. Anan'ev, *et al.*, in *Proceedings of XXXI Workshop on the Low Temperature Physics* (Mosk. Gos. Univ., Moscow, 1998), p. 262.
13. V. Herzog and E. L. Hahn, Phys. Rev. **103**, 148 (1956).

Translated by A. Bagatur'yants

JETP Letters, Vol. 80, No. 2, 2004, pp. 120–123. Translated from Pis'ma v Zhurnal Éksperimental'noĭ i Teoreticheskoĭ Fiziki, Vol. 80, No. 2, 2004, pp. 130–133.

Spin Splitting of *X*-Valley-Related Donor Impurity States in an AlAs Barrier

Yu. N. Khanin and E. E. Vdovin*

Institute of Microelectronic Technology and High-Purity Materials, Russian Academy of Sciences, Chernogolovka, Moscow region, 142432 Russia

**e-mail: vdovin@ipmt-hpm.ac.ru*

Received May 31, 2004; in final form, June 8, 2004

Magnetotunneling spectroscopy is used to reveal the spin splitting of the ground state of Si donors related to the *X* valley in an AlAs barrier. The absolute effective values of the longitudinal and transverse *g* factors in the AlAs barrier are found to be equal to 1.82 ± 0.15 and 1.11 ± 0.12, respectively. © *2004 MAIK "Nauka/Interperiodica".*

PACS numbers: 71.70.Ej; 73.20.Hb; 73.40.Gk; 71.55.Eq

In recent years, the effect of spin on electron transport has attracted considerable interest from both applied and fundamental points of view. The resonant tunneling through self-organized quantum dots (and localized impurity states physically similar to them) in semiconductor structures is a convenient tool for studying the spin-dependent electron transport. Such tunneling experiments have made it possible to directly observe the spin splitting of zero-dimensional impurity states in GaAs quantum wells [1–3] or in single InAs quantum dots [4–6] and to measure the absolute values of the *g* factor of zero-dimensional states. In addition, they provided the opportunity for the observation of mesoscopic fluctuations of the spin splitting in such systems [7].

In this paper, we report on the first observation of the spin splitting of the *X*-valley-related donor impurity states in an AlAs barrier (*X* donors) by means of magnetotunneling spectroscopy. Such donor states are formed in AlAs as a result of the penetration of silicon impurity atoms from the adjacent doped δ layers. We obtain the absolute values of the *g* factor of different zero-dimensional donor *X* states in magnetic fields applied across and along the current: $g_\perp = 1.11 \pm 0.12$ and $g_\parallel = 1.82 \pm 0.15$.

An isolated donor impurity in the region of the quantum well of a large-area resonance-tunneling diode forms a localized (~10 nm) hydrogen-like state belonging to the two-dimensional states in the quantum well. The current–voltage (*I–V*) characteristics of the tunneling structures exhibit sharp resonance features in the presence of a bias voltage at the instants when the energy of each single impurity state coincides with the Fermi energy of the emitter. The presence of multiple closely spaced impurity levels leads to multiple overlapping features in the *I–V* characteristic. In our previous work, the resonance tunneling through individual *X* donors in a relatively thin (5 nm) AlAs barrier (i.e., a quantum well for the electrons of the *X* valley) manifested itself as a fine structure of the main impurity resonance [8]. This fine structure had the form of a series of weak and rather spread resonance features associated with the tunneling through the donors localized in different positions within the AlAs layer. The effect of random fluctuations of the electrostatic potential on the energies of the donor impurities proved to be insignificant in this case. However, in the situation described in the present paper, where the donors occur in a relatively thick (11.2 nm) barrier, the effect of random fluctuations of the electrostatic potential is strong and the tunneling through the donors manifests itself as sharp, well-resolved peaks in the *I–V* characteristic, which makes it possible to study each peak separately. This fact allowed us to observe the spin splitting of the donor resonances and to directly determine the value of the *g* factor. In this case, the important role of random fluctuations of the electrostatic potential is related to the presence of doped δ layers near the barrier and to the weak dependence of the binding energy of donors on their position within the thick barrier [9].

In our experimental samples, the active part was a single 11.2-nm-thick AlAs barrier lying between two 2D electron gas layers. To form the 2D electron gas, we used δ layers with a concentration of 3×10^{11} cm^{-2}, which were formed on each side of the barrier, 2.8 nm away from it. The AlAs barrier was not doped during the growth process, but the donor states were formed in AlAs as a result of the diffusion of Si atoms from the adjacent doped δ layers. Figure 1 shows the calculated profiles of the Γ and *X* bands of the active part of the device at zero bias voltage. The measurements of the Shubnikov–de Haas oscillations in the structures showed that the electron concentration in the 2D elec-

tron gas coincided with the technologically intended Si concentration in the δ layers.

The samples studied in our experiment were single-barrier heterodiods grown by molecular beam epitaxy on highly doped N^+–GaAs substrates with the (100) orientation at a temperature of 570°C. The doping impurity was silicon, whose concentration in the substrates was 2×10^{18} cm^{-3}.

Each symmetric heterostructure consisted of the following sequence of layers: a 0.5-μm-thick 2×10^{18} cm^{-3} N^+–GaAs buffer, a 60-nm-thick 3×10^{17} cm^{-3} N^-–GaAs layer, a 21.6-nm-thick GaAs layer, a 5.6-nm-thick $Ga_{0.9}Al_{0.1}As$ layer, a 28-nm-thick undoped GaAs layer, a doped δ layer with a Si concentration of 3×10^{11} cm^{-2}, a 2.8-nm-thick undoped GaAs layer, an 11.2-nm-thick undoped AlAs barrier, a 2.8-nm-thick undoped GaAs layer, a doped δ layer with a Si concentration of 3×10^{11} cm^{-2}, a 28-nm-thick undoped GaAs layer, a 5.6-nm-thick undoped $Ga_{0.9}Al_{0.1}As$ layer, a 21.6-nm-thick undoped GaAs layer, a 60-nm-thick 3×10^{17} cm^{-3} N^-–GaAs layer, and a 0.5-μm-thick 2×10^{18} cm^{-3} N^+–GaAs contact layer.

The ohmic contacts were made by a sequential deposition of AuGa/Ni/Au layers with the following annealing at T = 400°C. To form a mesostructure 50–200 μm in diameter, we used the conventional chemical etching technique. The *I–V* characteristics were measured using the standard constant current method with a noise current below 50 fA. The measurements were performed at a temperature of 4.2 K in magnetic fields up to 8 T.

Figure 2 shows the *I–V* characteristics of two typical experimental samples, A and B, in a magnetic field of 8 T oriented across and along the direction of the current and in the absence of magnetic field at a temperature of 4.2 K. The dotted lines show the *I–V* characteristics in the absence of magnetic field. They exhibit series of sharp peaks in the bias voltage interval from 10 to 60 mV. The positions and amplitudes of the peaks are different for different samples, but they are completely reproducible for each individual sample even after a thermal cycling. We believe that these peaks appear in the *I–V* characteristics as a result of the resonance tunneling of electrons through individual impurity states in the AlAs barrier. Earlier, similar resonance features associated with the tunneling through individual zero-dimensional states were observed in the *I–V* characteristics of two-barrier heterostructures with GaAs quantum wells [1, 2, 10]. In our experiments, for both directions of magnetic field, the peaks corresponding to the tunneling of electrons through impurity states exhibit a splitting. In our opinion, the splitting of the peaks is caused by the lifting of the spin degeneracy of the impurity states in magnetic field. The positions and amplitudes of the peaks vary with increasing $B \parallel J$ because of the modulation of the parameters of 2D electron gas (the Fermi energy E_f and the bottom of the two-

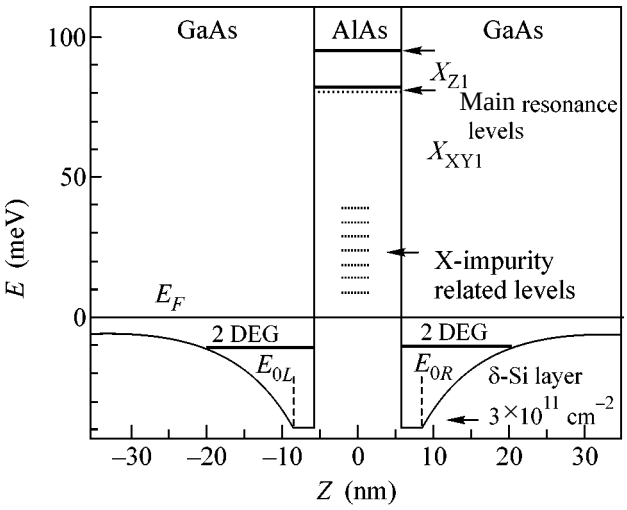

Fig. 1. Calculated potential profile of the active part of the experimental structure at zero bias voltage. The positions of the Fermi level, E_F, and the dimensional quantization levels, E_{0L} and E_{0R}, in GaAs and the positions of the dimensional quantization levels of X_Z and X_{XY} subbands and the *X* donors in AlAs are indicated in the plot.

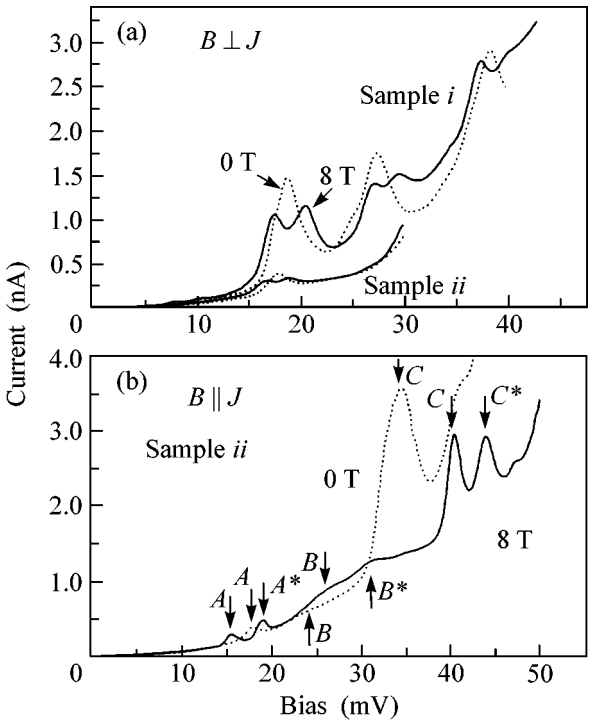

Fig. 2. (a) Current–voltage characteristics of two typical samples, A and B, in zero magnetic field (the dotted curve) and in a magnetic field of 8 T perpendicular to the tunnel current (the solid curve) at 4.2 K. (b) Current–voltage characteristics of sample B in zero magnetic field (the dotted curve) and in a magnetic field of 8 T parallel to the tunnel current (the solid curve) at 4.2 K.

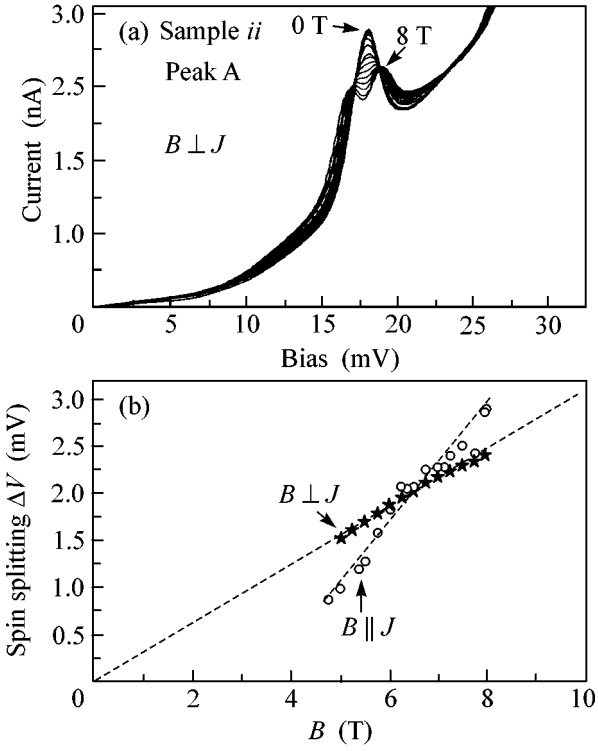

Fig. 3. (a) Evolution of the resonance peak with an increase from 0 to 8 T in the magnetic field perpendicular to the current at 4.2 K. The measurements were performed at a magnetic field step of 0.5 T. (b) The voltage difference corresponding to the splitting of maxima in the current–voltage characteristic as a function of magnetic field.

dimensional band E_0) due to the Landau quantization. However, the latter does not affect the measured value of the peak splitting.

Figure 3a shows the evolution of one of the resonance peaks with increasing magnetic field in the direction perpendicular to the current for the fields up to 8 T at a temperature of 4.2 K. The splitting of the experimental peaks is observed in this figure starting from a magnetic field of about 5 T because of the finite width of the peaks due to the temperature spread. Figure 3b shows the voltage difference corresponding to the split maxima of the *I–V* characteristic as a function of magnetic field. This dependence is of a linear character, which fits the simple Zeeman splitting model. The line approximating the experimental points passes through the origin of coordinates $B = 0$, $\Delta V = 0$, and has a slope equal to $g_\perp \mu_B/\alpha$, where μ_B is the Bohr magneton, $g_\perp$ is the effective value of the *g* factor in magnetic field perpendicular to the current, and α is the conversion factor for converting the measured voltage to energy. From self-consistent calculations of the potential profile along the experimental structure in the voltage interval of interest, 0–100 mV, it was found that the value of α remained approximately constant and equal to 0.19. A self-consistent solution to the set of Poisson–Schrödinger nonlinear equations was obtained by the numerical method similar to that described in [12]. As a result, the value of the transverse *g* factor was found to be $g_\perp = 1.08$. The values of $g_\perp$ obtained in the same way for different peaks corresponding to the tunneling through impurity states were found to lie within the interval from 0.98 to 1.23.

The dependence of the splitting ΔV on $B_\parallel$ is also of a linear character (see Fig. 3b) but is not extrapolated to 0 at $B = 0$, which, presumably, means that the simple Zeeman splitting model is inapplicable to the impurity states in the given interval of magnetic fields. A similar behavior was observed earlier in the study of the *g* factor in GaAs quantum wells [13], where it did not find any unique explanation. In our opinion, other possible manifestations of $B_\parallel$, such as the Landau quantization or the Zeeman splitting of states in the 2D electron gas, do not contribute to the measured splitting of the peaks but can only modify the decaying tails of the resonance features and shift the peaks in voltage. This allows us to believe that the slope of the dependence of ΔV on $B_\parallel$ immediately represents the spin splitting of the impurity and is determined by $g_\parallel$. The values of the *g* factor obtained by us from the slope of the approximating straight line for magnetic fields perpendicular and parallel to the current are noticeably different: $g_\perp = 1.08$ and $g_\parallel = 1.93$. Theoretical calculations and optical studies of magnetic resonance in bulk AlAs layers reveal a small anisotropy of the *g* factor and yield the following sets of values of its transverse and longitudinal components: 2.004 and 1.915, respectively, and 1.976 and 1.917, respectively. The much greater difference between $g_\perp$ and $g_\parallel$ observed in our experiments may be related to the penetration of the electron wave function into the adjacent GaAs layers, where the *g* factor is equal to 0.44.

Thus, using magnetotunneling spectroscopy, we revealed the spin splitting of the ground state of the *X*-valley-related Si donors in the AlAs barrier. We determined the absolute effective values of the longitudinal and transverse *g* factor in the AlAs barrier: 1.82 ± 0.15 and 1.11 ± 0.12, respectively. The origin of the anomalously large anisotropy of the *g* factor is likely to be the penetration of the electron wave function into the adjacent GaAs layers. Note that it is the large value of the *g* factor in AlAs that makes it possible to observe the spin splitting of the impurity states at a relatively high temperature of 4.2 K, whereas, for the impurity in GaAs quantum wells, where the value of the *g* factor is as small as 0.14–0.3, the spin splitting can be observed only in the millikelvin temperature range [1–3].

We are grateful to M. Henini for supplying us with heterostructures, to Prof. L. Eaves for many useful discussions, and to Yu.N. Dubrovskii for the interest in this work. The work was supported in part by the Russian Foundation for Basic Research, project no. 03-02-17693.

REFERENCES

1. M. R. Deshpande, J. W. Sleight, M. A. Reed, *et al.*, Phys. Rev. Lett. **76**, 1328 (1996).
2. J. W. Sakai, N. La Scala, Jr., P. C. Main, *et al.*, Solid-State Electron. **37**, 965 (1994).
3. J. Könemann, P. König, and R. J. Haug, Physica E (Amsterdam) **13**, 675 (2002).
4. A. S. G. Thornton, T. Ihn, P. C. Main, *et al.*, Appl. Phys. Lett. **73**, 354 (1998).
5. I. Hapke-Wurst, U. Zeitler, H. Frahm, *et al.*, Phys. Rev. B **62**, 12621 (2000).
6. I. Hapke-Wurst, U. Zeitler, R. J. Haug, and K. Pierz, Physica E (Amsterdam) **13**, 802 (2002).
7. P. König, T. Schmidt, and R. J. Haug, Europhys. Lett. **54**, 495 (2001).
8. Yu. N. Khanin, E. E. Vdovin, Yu. V. Dubrovskii, *et al.*, Phys. Rev. B **66**, 073302 (2002).
9. G. Weber, Appl. Phys. Lett. **67**, 1447 (1995).
10. J. W. Sakai, P. C. Main, P. H. Beton, *et al.*, Appl. Phys. Lett. **64**, 2563 (1994).
11. E. R. Glaser, T. A. Kennedy, B. Molnar, *et al.*, Phys. Rev. B **43**, 14540 (1991).
12. H. Tan, G. L. Snider, L. D. Chang, and E. L. Hu, J. Appl. Phys. **68**, 4071 (1990).
13. N. La Scala, Jr., P. McDonnell, J. W. Sakai, *et al.*, in *Proceedings of 23rd International Conference on Physics of Semiconductors* (Berlin, 1996), p. 2419; J. W. Sakai *et al.*, Solid-State Electron. **37**, 965 (1994).

Translated by E. Golyamina

JETP Letters, Vol. 80, No. 2, 2004, pp. 124–129. Translated from Pis'ma v Zhurnal Éksperimental'noĭ i Teoreticheskoĭ Fiziki, Vol. 80, No. 2, 2004, pp. 134–139.

Collective Magnetoplasma Excitations in Two-Dimensional Electron Rings

S. I. Gubarev[1], V. A. Koval'skiĭ[1,*], D. V. Kulakovskiĭ[1], I. V. Kukushkin[1], M. N. Khannanov[1], J. Smet[2], and K. von Klitzing[2]

[1] *Institute of Solid State Physics, Russian Academy of Sciences, Chernogolovka, Moscow region, 142432 Russia*

**e-mail: koval@issp.ac.ru*

[2] *Max-Planck-Institut für Festkörperforschung, 70569 Stuttgart, Germany*

Received June 10, 2004

The spectra of magnetoplasma excitations in two-dimensional electron disks and rings are studied by optical detection of resonance microwave absorption. For ring-shaped structures, two types of edge magnetoplasma modes localized along the inner and outer boundaries of the ring are observed. It is shown that the interaction between these modes leads to a strong modification of their magnetic-field dependences as compared to disks. In addition to the longitudinal edge magnetoplasma excitations, transverse plasma modes associated with the electron density oscillations along the ring radius are revealed. The spectra of magnetoplasma excitations are calculated in terms of the electrodynamic theory for both ring-shaped and disk-shaped structures. The classification of all modes of collective magnetoplasma excitations observed in the experiment is performed on the basis of the comparison between experimental and theoretical results. © *2004 MAIK "Nauka/Interperiodica".*

PACS numbers: 73.20.Mf; 71.35.Cc

Low-dimensional electron systems in semiconductor structures are the object of numerous experimental and theoretical studies. Specifically, considerable interest has been expressed in studying magnetoplasma excitations in two-dimensional electron systems confined to a certain geometry. Most publications concerned with this subject consider the properties of 2D and 1D magnetoplasma excitations in structures shaped as disks, quantum dots, antidots, and quantum wires [1–6]. Meanwhile, structures with the ring geometry were relatively poorly investigated from both theoretical and experimental points of view. In this geometry, by varying the ratio of the outer a and inner b diameters of the ring, one can study the transition from two-dimensional ($a/b \gg 1$) to one-dimensional ($a/b \sim 1$) plasma excitations. Another attractive feature of the ring geometry is the possibility to study the interaction between two spatially close magnetoplasma edge modes and the dependence of this interaction on distance, electron density, and magnetic field. The few experimental [7] and theoretical [8] attempts to study 2D structures with a ring geometry did not clarify the question about the modification of plasma excitations at the transition from the one-dimensional to two-dimensional case, because these studies included no comparative analysis of rings with different ratios a/b and no comparison between the spectra of plasma excitations in disks and rings. In addition, in the experiment [7], not all magnetoplasma excitation modes characteristic of the ring geometry were observed and the dependence of the energy of these modes on the 2D carrier concentration was not investigated.

The present paper reports on the study of the collective excitation spectrum of a ring-shaped 2D electron system. A comparative analysis of the excitation spectra measured for a ring and a disk with the same outer diameter is performed, and the modification of the magnetoplasma excitation modes depending on the dimensions, magnetic field, and 2D electron concentration is investigated.

The measurements were carried out on two n-type GaAs/AlGaAs structures (300-Å-wide single quantum wells) with electron densities of 2.5×10^{11} and 0.8×10^{11} cm^{-2}. On these substrates, mesas were fabricated (by photolithography) in the form of rings with the outer diameter a = 0.6 mm and the inner diameter b = 0.2 mm. For comparison, disks with a diameter of 0.6 mm coinciding with the outer diameter of the rings were fabricated on the same substrates. The spectra of the dimensional magnetoplasma resonances were measured by the method of optical detection of microwave absorption [9, 10], which provides a high sensitivity. We studied differential (with respect to the microwave power) spectra of recombination radiation of 2D electrons at a temperature T = 1.5–4.2 K in the frequency range of microwave excitation from 4 to 50 GHz. The photoexcitation and the reception of the recombination radiation were performed via a quartz optical fiber, which led directly to the sample. The optical signal was

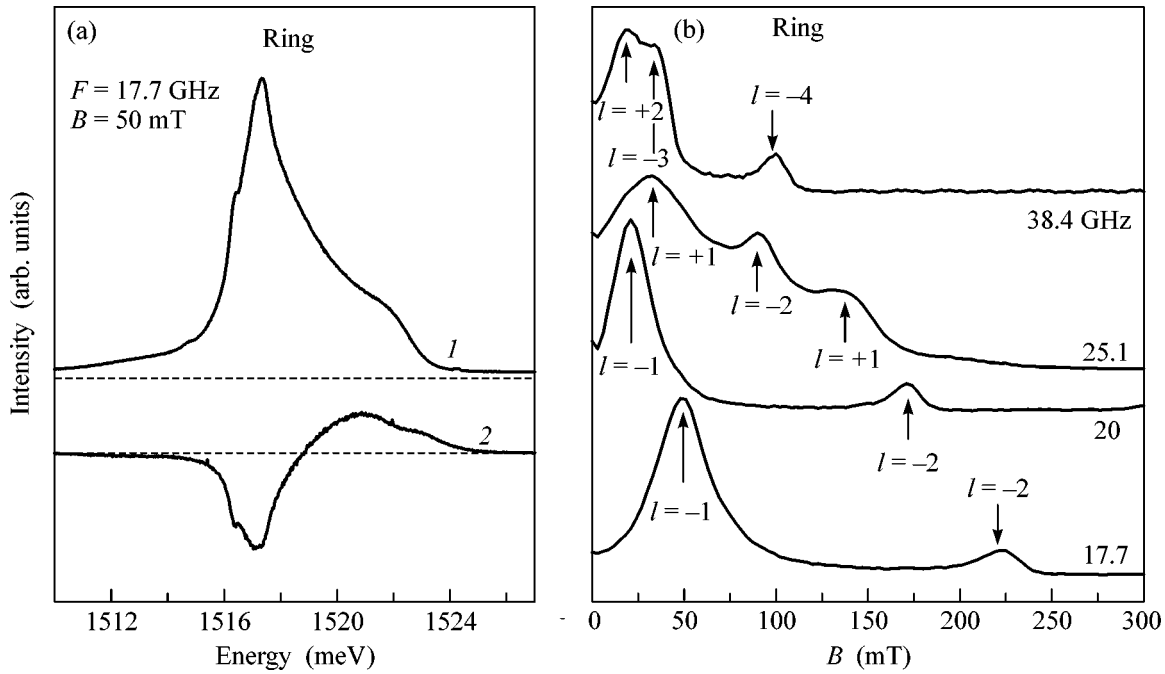

Fig. 1. (a) (*1*) Experimental luminescence spectrum of radiation and (*2*) the differential spectrum with respect to the microwave power for a structure with a ring geometry (a = 0.6 and b = 0.2 mm) in the resonance magnetic field B = 50 mT at a microwave excitation frequency of 17.7 GHz. (b) Typical magnetic-field dependences of resonance absorption measured for the same structure with different microwave radiation frequencies. The 2D electron concentration is 2.6×10^{11} cm^{-2}.

received by a high-sensitivity CCD camera and analyzed by a double spectrometer with a spectral resolution of 0.03 meV. The microwave radiation was supplied to the sample either through the microwave channel or through a coaxial microwave cable providing the high-frequency power transmission in the frequency range of 0–50 GHz with an attenuation smaller than 5 dB. The absolute value of the difference signal was integrated over the whole spectrum of the recombination radiation, and the resulting integral intensity of the differential spectrum served as a measure of the intensity of microwave absorption. Thus measured, the intensity of microwave absorption was studied as a function of magnetic field for different microwave excitation frequencies.

Figure 1a shows a typical radiation recombination spectrum of 2D electrons (the upper curve) and the corresponding differential spectrum with respect to the microwave power (the lower curve); the spectra were obtained at T = 1.5 K and a 2D electron concentration of 2.6×10^{11} cm^{-2} under the resonance conditions (f = 17.7 GHz) in magnetic field B = 50 mT. According to this figure, the resonance microwave absorption leads to a change in the shape of the recombination radiation line because of the heating of the electron system due to the resonance absorption of the microwave power. Figure 1b shows the dependences of the resonance absorption on magnetic field for a ring structure (a = 0.6 mm and b = 0.2 mm) with a 2D electron concentration of 2.6×10^{11} cm^{-2} under different microwave excitation frequencies. The arrows indicate the magnetoplasma modes observed in the experiment and classified according to the theoretical calculation (see below). The dependences of the resonance magnetic field measured in this manner on the microwave radiation frequency are shown in Fig. 2a. For comparison, Fig. 2b presents the magnetic-field dependence of the resonance modes for a structure fabricated in the form of a disk with a diameter equal to the outer diameter of the ring on the same substrate. From Figs. 2a and 2b, one can see that, although the electron concentrations and the outer diameters of the structures are equal, their magnetoplasma excitation spectra are radically different.

For the classification of the resonances observed in the experiment, it is convenient to use two quantum numbers that completely describe all resonance modes for both the ring geometry and the disk. One of these numbers is n = 0, 1, 2, …, which corresponds to the number of nodes that occur in the radial direction for the distribution of the charge density perturbation. The other is the azimuthal number l, which describes the angular distribution of the induced charge density and takes on the values 0, ±1, ±2, ±3, …. Applying this terminology to the magnetic-field dependences shown in Figs. 2a and 2b, we can state that the resonance modes observed in our experiment belong to the series of excitations with n = 0 and different l. Specifically, for the

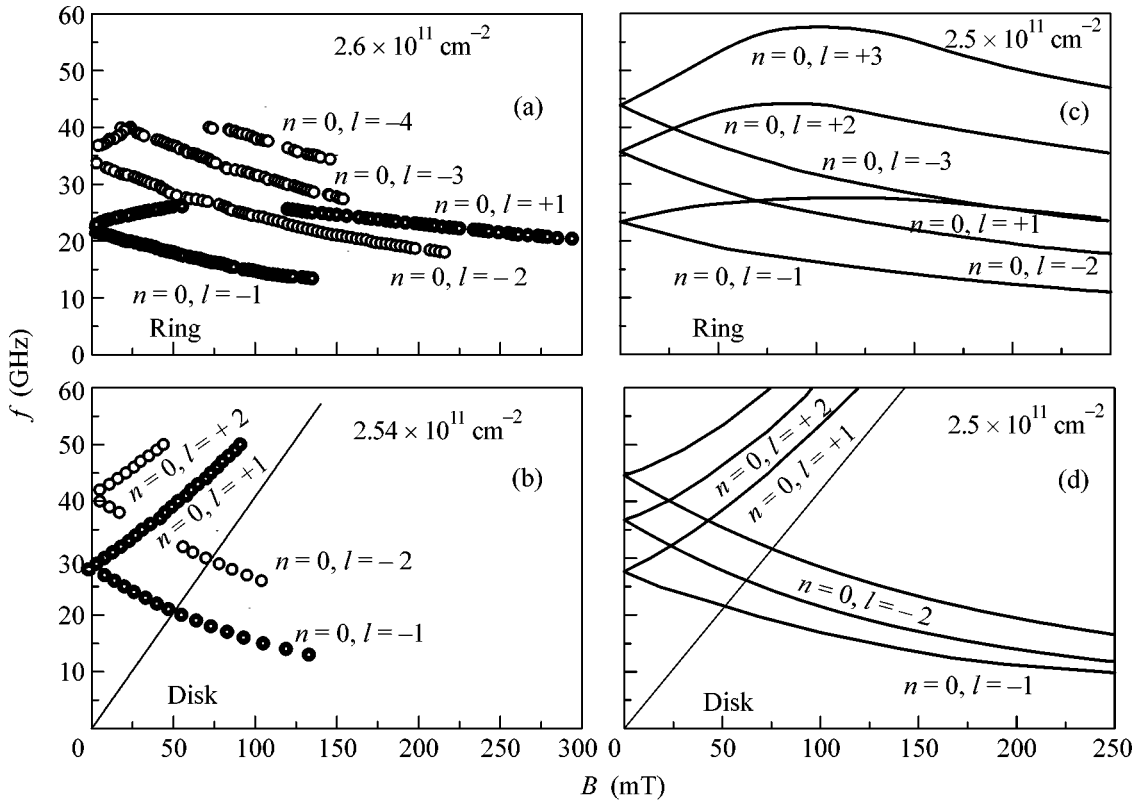

Fig. 2. Experimental magnetic-field dependences of the resonance excitation frequencies of different magnetoplasma modes for (a) a ring structure with $a = 0.6$ mm and $b = 0.2$ mm and (b) a disk with a diameter of 0.6 mm at $n_s = 2.6 \times 10^{11}$ cm^{-2}. Theoretical dependences $f(B)$ for the (c) ring and (b) disk geometries with the same parameters.

ring geometry, modes with $l = \pm 1, \pm 2, -3$, and -4 manifest themselves, and for the disk geometry, we have modes with $l = \pm 1$ and ± 2. Despite the identical symmetries and similar choices of quantum numbers, the behavior of magnetoplasma resonances in the case of the ring geometry qualitatively differs from that in the disk. The difference is most pronounced for the upper branch of the lower doublet of the resonance modes (curve $n = 0$, $l = +1$ in Fig. 2a). In the region of low magnetic fields, this mode has a positive magnetodispersion, as well as the corresponding mode in the disk geometry (curve $n = 0$, $l = +1$ in Fig. 2b). However, unlike the case of the disk, where the dependence is monotonic and asymptotically tends to the cyclotron resonance frequency in the region of high magnetic fields, in the case of the ring geometry, it reaches a maximum near 80 mT and then decreases with increasing magnetic field. Simultaneously, a sharp decrease occurs in the oscillator strength of the corresponding resonance. Such a behavior of the resonance mode testifies to its localization near one of the ring edges starting from a certain magnetic field and, hence, points to the edge character of this mode. A similar behavior in high magnetic fields is observed for the lower resonance branch (curve $n = 0$, $l = -1$ in Fig. 2a). This mode initially has a negative magnetodispersion and, as the magnetic field increases, it becomes localized along the outer edge of the ring representing an analogue of the edge magnetoplasma mode with $n = 0$, $l = -1$ in the disk. Proceeding from this fact, we can assume that, in high magnetic fields, the mode with $n = 0$, $l = +1$ is localized and propagates along the inner boundary of the ring, because its excitation energy in these fields considerably exceeds the excitation energy of the lower resonance mode with $n = 0$, $l = -1$ propagating along the outer boundary. In addition to the aforementioned resonances, the magnetoplasma spectrum of the ring contains other edge modes, namely, modes with quantum numbers $l = -2, -3$, and -4. These excitations also propagate along the outer edge of the ring but possess higher energies.

We also carried out the measurements for a ring with the same dimensions but with a lower concentration of 2D carriers: 0.8×10^{11} cm^{-2}. The resulting dependences of the energies of resonance mode excitation on magnetic field are shown in Fig. 3a. As in the case of Fig. 2, Fig. 3b shows the corresponding magnetic-field dependences for a disk with the same concentration of 2D carriers. In addition to the lower resonance modes with $n = 0$, $l = \pm 1$, excitations corresponding to $n = 1$ appear in ring-shaped structures with lower charge carrier con-

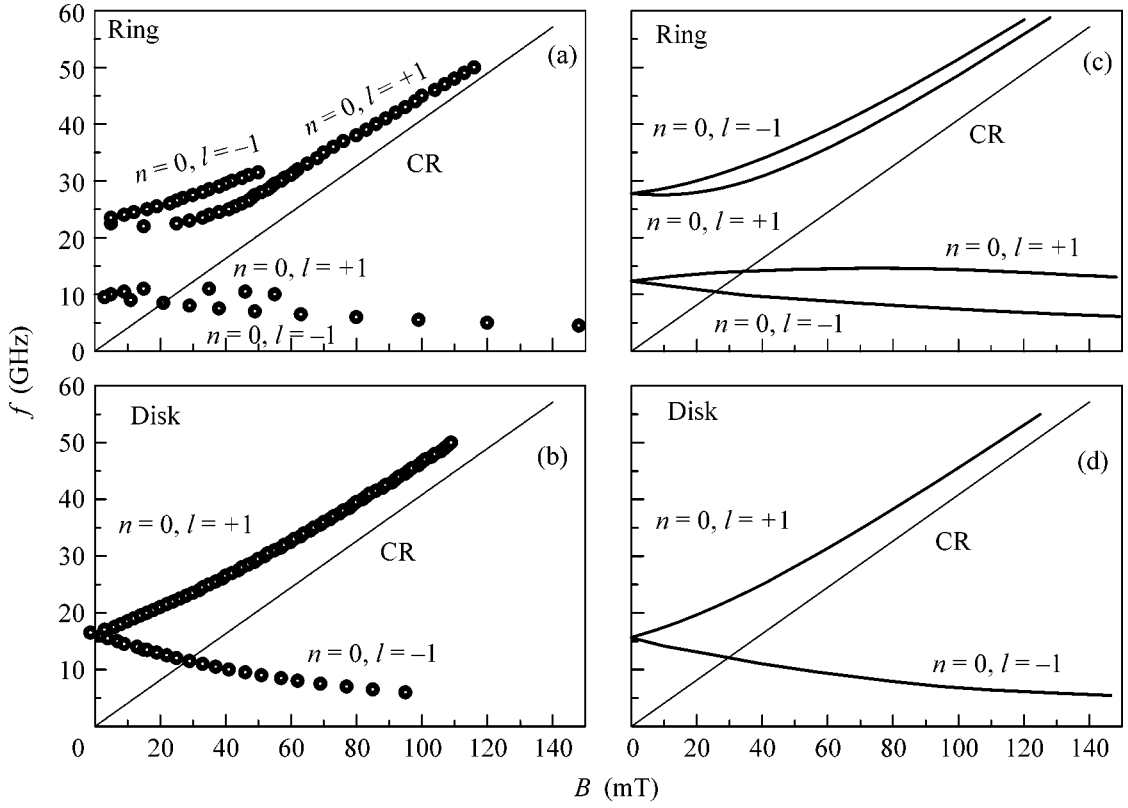

Fig. 3. Experimental magnetic-field dependences of the resonance excitation frequencies of different magnetoplasma modes for (a) a ring structure with $a = 0.6$ mm and $b = 0.2$ mm and (b) a disk with a diameter of 0.6 mm at $n_s = 0.8 \times 10^{11}$ cm^{-2}. Theoretical dependences $f(B)$ calculated for the (c) ring and (d) disk geometries with the same parameters.

centrations. The fundamental difference between these excitations and the resonances with $n = 0$ lies in their behavior in high magnetic fields. The resonance modes with $n = 0$ are localized along the inner and outer edges of the ring, while the upper resonances with $n = 1$ behave in a radically different way. As is seen from Fig. 3a, the lower branch of the resonance doublet with $n = 1$, $l = +1$ has a negative magnetodispersion in low magnetic fields; as the field increases, this branch exhibits a growth and, in high magnetic fields, it tends to the cyclotron resonance frequency, thus displaying the features of a "bulk" magnetoplasmon. By contrast, the upper branch of this doublet with $n = 1$, $l = -1$ initially has a positive magnetodispersion but rapidly decays with increasing magnetic field and, therefore, is only observed in the fields below 50 mT. Note that, unlike the edge modes with $n = 0$, $l = \pm 1$, which are related to the charge density oscillations along the perimeter of the ring, the modes with $n = 1$, $l = \pm 1$ are related to the charge density oscillations along the radius of the ring, and the quantity $\omega_{n=1}(B = 0) = \Omega$ is the corresponding plasma frequency.

In addition to the aforementioned difference between the magnetic-field dependences of resonances in the ring- and disk-shaped structures, the behavior of the magnetoplasma modes exhibit other distinctive features, which testify to the transition from the purely two-dimensional case (disk) to the quasi-one-dimensional case (ring). Primarily, this refers to the lower edge resonance mode in the ring, which exhibits a magnetic-field dependence different from the one characteristic of the disk geometry. Such a behavior can be explained by the strong interaction of the two edge modes corresponding to the outer and inner edges of the ring. This interaction is almost completely absent in the ring with a small inner diameter ($a/b \gg 1$)), and, as a consequence, the plasma frequency at $B = 0$ and the dependence of the resonance frequencies on magnetic field should in this case only slightly differ from those obtained for the disk geometry. Figure 4a illustrates the comparison of the magnetic-field dependences obtained for the frequencies of the lower edge magnetoplasma modes, $n = 0$, $l = -1$, localized at the outer perimeter of the structures in the case of the disk geometry with the diameter $d = 0.6$ mm and in the case of the ring geometry with $a = 0.6$ mm and $b = 0.2$ mm at a 2D electron concentration of 0.8×10^{11} cm^{-2}. As one can see from this figure, in the case of the ring, the plasma frequency at $B = 0$ is almost two times smaller and the field dependence is weaker than in the case of the disk.

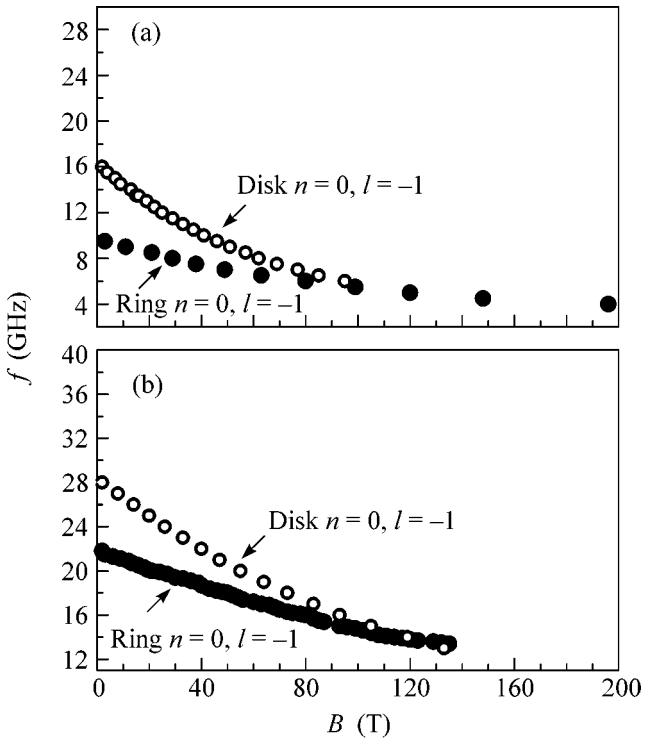

Fig. 4. Comparison of the experimental magnetic-field dependences of the lower resonance mode with $n = 0$, $l = -1$ for a disk with a diameter of 0.6 mm and a ring with a = 0.6 mm and b = 0.2 mm; the 2D electron density concentration is (a) 0.8×10^{11} and (b) 2.6×10^{11} cm^{-2}.

In addition, the characteristic magnetic field at which the resonance frequency decreases by half is greater in the case of the ring: 0.14 T instead of 0.06 T in the case of the disk. Such a dependence of the frequency of the lower resonance mode on magnetic field testifies to a considerable interaction between the inner and outer edge modes. Indeed, according to the theoretical calculations [6], the closer the edge modes, the higher the frequency Ω and the weaker the magnetic-field dependence $\omega(B) \sim \Omega\left(\frac{\Omega^2}{\Omega^2 + \omega_c^2}\right)^{1/2}$. A similar effect of the edge mode interaction is observed for a 2D electron concentration of 2.5×10^{11} cm^{-2} (Fig. 4b).

Our assumptions concerning the classification and character of the magnetoplasma modes observed in the experiment are confirmed by theoretical calculations in terms of the classical electrodynamics [11]. In these calculations, a self-consistent solution is found to the Poisson equation and the continuity equation for the induced density of 2D charge carriers with additional boundary conditions for the radial component of the current. The problem is solved by expanding the concentration in the orthonormal basis of Bessel functions of the first and second kinds, $J_l(\mu_{n,l}r)$ and $Y_l(\mu_{n,l}r)$, in a ring with a sharp potential profile.[1] We used this method to calculate the energies of the eigenmodes of electron density in the ring geometry for different quantum numbers (n, l). Specifically, for modes with $n = 0$ and $l = \pm 1$, ± 2, and ± 3, the corresponding calculated magnetic-field dependences are shown in Fig. 2c. For comparison, Fig. 2d shows the magnetoplasma excitation spectrum calculated for the disk geometry. Figure 3c displays dependences of magnetoplasma resonances on magnetic field that are calculated in a similar way for a ring with a = 0.6 mm and b = 0.2 mm and with an electron concentration of 0.7×10^{11} cm^{-2} and for a disk with a diameter D = 0.6 mm and with a 2D electron concentration of 0.8×10^{11} cm^{-2}. From Figs. 2 and 3, one can see that the experimental and theoretical results are in good agreement, which determines the classification of all magnetoplasma modes observed in the experiment.

Thus, by employing the optical detection method, we experimentally studied the magnetic-field dependences of the resonance excitation frequencies in 2D electron rings. The resonance spectra of rings exhibit two types of modes: the high-frequency "bulk" magnetoplasma excitations, which tend to the cyclotron resonance frequency in high magnetic fields, and a set of edge magnetoplasma modes with lower energies, which propagate along the inner and outer boundaries of the ring. We carried out a classification of the resonances observed in the experiment on the basis of the radial and azimuthal quantum numbers. For comparison with the ring geometry, we used the same method to measure the excitation spectra for a disk with a diameter equal to the outer diameter of the ring. We have shown that a change in the geometry of the structure under study leads to a qualitatively different resonance excitation spectrum. In terms of the electrodynamic theory, we calculated the magnetic-field dependences of resonance excitations for both the ring and the disk. The resulting energies of plasma and magnetoplasma excitations coincide with the resonances observed in the experiment, which testifies to the applicability of the given approximation. All this allows us to construct a full picture of collective excitations of the electron gas in a ring and opens up new possibilities for further studies of 2D edge plasmons. In this respect, the phenomenon of special interest is the transition from 2D to 1D magnetoplasma excitations, which occurs in the ring geometry when the ratio of the outer diameter to the inner one decreases.

This work was supported by the Russian Foundation for Basic Research and by the INTAS (project no. 03-51-6453).

REFERENCES

1. S. J. Allen, Jr., H. L. Stormer, and J. C. M. Hwang, Phys. Rev. B **28**, 4875 (1983).

[1] The numbers $\mu_{n,l}$ are determined from the boundary conditions.

2. T. Demel, D. Heitmann, P. Grambow, and K. Ploog, Phys. Rev. Lett. **64**, 788 (1990); **66**, 2657 (1991).
3. A. Lorke, J. P. Kotthaus, and K. Ploog, Phys. Rev. Lett. **64**, 2559 (1990).
4. D. B. Mast, A. J. Dahm, and A. L. Fetter, Phys. Rev. Lett. **54**, 1706 (1985).
5. D. C. Glattli, E. Y. Andrei, G. Deville, *et al.*, Phys. Rev. Lett. **54**, 1710 (1985).
6. I. L. Aleiner, Dongxiao Yue, and L. I. Glazman, Phys. Rev. B **51**, 13467 (1995).
7. C. Dahl, J. P. Kotthaus, H. Nickel, and W. Schlapp, Phys. Rev. B **48**, 15480 (1993).
8. F. A. Reboredo and C. R. Proetto, Phys. Rev. B **53**, 12617 (1996).
9. B. M. Ashkinadze *et al.*, Phys. Status Solidi A **164**, 523 (1997).
10. I. V. Kukushkin, J. H. Smet, S. A. Mikhailov, *et al.*, Phys. Rev. Lett. **90**, 156801 (2003).
11. A. L. Fetter, Phys. Rev. B **33**, 5221 (1986).

Translated by E. Golyamina

JETP Letters, Vol. 80, No. 2, 2004, pp. 130–132. From Pis'ma v Zhurnal Éksperimental'noĭ i Teoreticheskoĭ Fiziki, Vol. 80, No. 2, 2004, pp. 140–142.

Electronic Spectrum and Ballistic Transport in Bent Nanotubes¶

A. V. Chaplik

Institute of Semiconductor Physics, Novosibirsk, 630090 Russia
University of Aizu, Aizu–Wakamatsu City, Fukushima, 965-80 Japan

Received June 17, 2004

It is shown that bending of a nanotube leads to splitting of the electron energy levels due to breaking of the azimuthal symmetry. The bent section of the nanotube acts as a scatterer for ballistic carriers, resulting in qualitative changes in the dependence of conductance on the Fermi energy. © *2004 MAIK "Nauka/Interperiodica".*

PACS numbers: 73.21.-b; 73.23.Ad

The past few years were marked by growing interest in electro-nanomechanical structures. These are freely suspended objects of a nanoscale size in which it becomes possible to affect the electron motion by making use of mechanical degrees of freedom of the structures: bending, twisting, folding in a roll, etc. In such situations, one deals with electronic waves propagating in curvilinear waveguides and electrons are subjected to the action of the so-called geometric potential (see, e.g., [1] and references therein).

In a strictly 1D case (curved quantum wire), the geometric potential attracts particles, independent of their charge, to the point of maximal curvature, and the formation of a bound state is, in principle, possible. A more complicated situation occurs for electrons confined to move upon the surface of a hollow cylinder (nanotube). This very case is analyzed in the present paper.

1. General relations. Consider a nanotube with the semiconductor type of the electron energy spectrum:

$$\varepsilon_m(k) = Bm^2 + \frac{\hbar^2 k^2}{2\mu}, \qquad (1)$$

where $m = 0, \pm 1, \pm 2, \ldots$ is the azimuthal quantum number, k is the longitudinal momentum, B is the rotational constant, $B = \hbar^2/2\mu a^2$, a is the nanotube radius, and μ is the effective mass. All states with $m \neq 0$ are doubly degenerate, since energy is independent of the sign of azimuthal moment $\pm m$. If the nanotube is bent, its cylindrical symmetry breaks down, and this should result in splitting of the states $\pm m$ as well as in a shift of all the energy levels. The reason for such changes in the energy spectrum stems from the geometric potential and, moreover, the kinetic energy operator is modified (see [2, 3] and more recent works [4, 5]). Both these factors also cause the electron scattering and, hence, affect the ballistic conductivity of a nanotube. In the situation in question, we deal with 2D carriers moving on a bent cylinder. The geometric potential has the form [2, 3]

$$U = -\frac{\hbar^2}{8\mu}\left(\frac{1}{R_1} - \frac{1}{R_2}\right)^2. \qquad (2)$$

Here, R_1, R_2 are the principal radii of curvature at the point on a surface where an electron resides. The operator of kinetic energy is, of course, the Laplacian presented in the proper curvilinear orthogonal coordinates u and v:

$$\hat{T} = -\frac{\hbar^2}{2\mu}\frac{1}{\sqrt{g}}\sum_{\alpha,\beta=1}^{2}\frac{\partial}{\partial u_\alpha}\left(\sqrt{g}g^{\alpha\beta}\frac{\partial}{\partial u_\beta}\right), \qquad (3)$$

where g is the determinant of the metric tensor. For the situation in question, $R_1 = a$ is the "eigenradius" of the nanotube, while $R_2 \equiv R$ is the curvature radius of the bent nanotube.

Suppose the nanotube is bent without twisting; in other words, its axis remains a plane curve. Then, each small part of the nanotube can be considered as an arc of torus with the local big radius $R(s)$, where s is the length of the nanotube axis counted from an arbitrary origin. As for the small radius of the torus, it remains constant for any s and equals a. The pair of coordinates u, v can be chosen as $u = a\varphi$, $v = s$, where φ is the azimuthal angle in the torus cross section. Then, the squared element of length on the torus surface takes the form

$$dl^2 = a^2 d\varphi^2 + (1 + a\cos\varphi/R(s))^2 ds^2, \qquad (4)$$

¶ This article was submitted by the author in English.

0021-3640/04/8002-0130$26.00 © 2004 MAIK "Nauka/Interperiodica"

while the Laplace operator reads

$$\hat{\Delta} = \frac{1}{ah}\left(\frac{\partial}{\partial\varphi}\frac{h}{a}\frac{\partial}{\partial\varphi}\right) + \frac{1}{h}\frac{\partial}{\partial s}h\frac{1}{h}\frac{\partial}{\partial s}, \qquad h = h(s,\varphi) \equiv 1 + \frac{a\cos\varphi}{R(s)}. \tag{5}$$

The geometric potential in the coordinates φ, s is

$$U = -\frac{\hbar^2}{8\mu}\left[\frac{1}{a} - \frac{\cos\varphi}{R(s) + a\cos\varphi}\right]^2. \tag{6}$$

By introducing the function $\chi(\varphi, s)$ instead of the wave function ψ in accord with the relation $\psi = \chi/\sqrt{h}$, one can eliminate the first derivative $\partial/\partial\varphi$ and obtain the Schrödinger equation

$$-B\left[\frac{\partial^2}{\partial\varphi^2} + \frac{a\cos\varphi}{2Rh} + \frac{a^2\sin^2\varphi}{4R^2h^2}\right]\chi - \frac{\hbar^2}{8\mu a^2}\left(1 - \frac{a\cos\phi}{Rh}\right)^2\chi - \frac{\hbar^2}{2\mu\sqrt{h}}\frac{\partial}{\partial s}\frac{1}{h}\frac{\partial}{\partial s}\frac{\chi}{\sqrt{h}} = E\chi. \tag{7}$$

In what follows, two effects will be considered in which the bending of the nanotube is manifested.

2. Spectrum of a torus arc. Consider the simplest case: $R(s) = \text{const}$ for $0 < s < L$, so we deal with a piece of torus of the lengths L. The boundary conditions are $\psi(0) = \psi(L) = 0$. Equation (7) gives immediately $\chi = F(\varphi)\sin\kappa_n s$ with $\kappa_n = n\pi/L$, n is an integer, and we obtain a 1D Schrödinger equation with a rather complicated effective potential energy $U_{\text{eff}}(\varphi)$. It is reasonable to suppose the condition $a \ll R$ is satisfied and to look for the energy spectrum in the frame of perturbation theory. To do this, one has to expand $U_{\text{eff}}(\varphi)$ up to terms of the order of $(a/R)^2$, because these terms contain the factor $\cos 2\varphi$, which gives splitting of the states $m = \pm 1$ in the first order of perturbation approach, while terms of the type $a\cos\varphi/R$ give the same splitting in the second order.[1] The splitting is determined by the combined matrix element

$$V = V^{(2)}_{1,-1} + \frac{V^{(1)}_{1,0}V^{(1)}_{0,-1}}{\varepsilon_1 - \varepsilon_0}, \tag{8}$$

where $V^{(1)}$ and $V^{(2)}$ denote the contributions from $\cos\varphi$ and $\cos 2\varphi$, respectively. The results of calculations give for the three lowest subbands of the toroidal segment of nanotube

$$\varepsilon_{0n} = \frac{\hbar^2\kappa_n^2}{2\mu} - \frac{\hbar^2}{8\mu R^2} + \frac{\hbar^2}{2\mu R^2}\left(\frac{3}{2}\kappa_n^2a^2 - \kappa_n^4a^4\right), \tag{9}$$

$$\varepsilon_{\pm n} = B + \varepsilon_{0n} \pm \frac{\hbar^2}{2\mu R^2}\left(\kappa_n^4a^4 + \frac{3}{4}\kappa_n^2a^2 - \frac{3}{16}\right). \tag{10}$$

[1] It is easy to see a similarity of the problem in question with Λ doubling in the spectra of biatomic molecules.

Thus, the absorption line of inter- or intraband transitions in which the subband $m = \pm 1$ is involved splits in accord with Eq. (10) if the nanotube is bent. The splitting rapidly increases with increasing quantum number of the longitudinal motion n (as n^4). Of course, the perturbative approach should be valid, i.e., $\kappa_n^2a^2 \ll R/a$.

3. Ballistic transport in bent nanotubes. It is clear from the previous consideration that any bent part of a nanotube acts as a scatterer for mobile electrons. In quasi-1D objects, scattering simply means nonzero reflection coefficient R and the transmission coefficient T not equaled to 1. Hence, the well-known staircase-like dependence of conductance on the Fermi energy should be modified for a bent nanotube.

Suppose the nanotube is asymptotically rectilinear, i.e., $R(s) \longrightarrow \infty$ for $s \longrightarrow \pm\infty$, and suppose, in addition, that $R(s)$ changes slowly as a function of its argument s: $dR/ds \ll 1$. Then, the adiabatic approach to the problem can be developed: at first, to omit the term with derivatives $\partial/\partial s$ in Eq. (7) and to find the "momentary" eigenfunctions $\chi_i(\varphi, s)$, where s is treated as a parameter, then, to search for the total wave function as the expansion $\sum c_i(s)\chi_i(\varphi, s)$. An interesting feature of the situation in question is the dependence of the coefficient at the "slow" part of the Hamiltonian (with derivatives $\partial/\partial s$) on the "fast" variable φ: h depends on φ. Hence, even if one neglects the terms $\partial\chi_i/\partial s$ and $\partial^2\chi_i/\partial s^2$ (the zeroth adiabatic approximation), the system of equations for slow amplitudes $c_i(s)$ will not become decoupled, as is usually the case in other adiabatic problems. Actually, the effective mass in our case is a matrix (depending, of course, on s)

$$-\frac{\hbar^2}{2}\sum_k\left\langle\frac{1}{\mu}\right\rangle_{ik}\frac{\partial^2c_k}{\partial s^2} + \varepsilon_i(s)c_i(s) = Ec_i(s), \tag{11}$$

where ε_i are given by Eqs. (9) and (10) with $\kappa_n = 0$ and

$$\left\langle\frac{1}{\mu}\right\rangle_{ik} = \frac{1}{\mu}\int\chi_i^*\left(1 + \frac{a\cos\varphi}{R}\right)^{-2}\chi_k d\varphi. \tag{12}$$

In what follows, an example is considered when only three states χ_0 and $\chi_\pm$ contribute to the total conductance. In other words, the Fermi energy lies below the bottom of the subband $m = \pm 2$: $0 < E_F < 4B$.

If $E_F < B$, only the state $m = 0$ is involved and the bending results merely in an arising potential well of depth $\hbar^2/8\mu R^2$ (see Eq. (9)). For small Fermi energy $E_F \ll \alpha^2B$, $\alpha \equiv a/R$, the transmission coefficient in the channel $m = 0$ tends to zero in accord with the well-known formula

$$T_{00} = \frac{E}{E + W}, \quad E = E_F, \tag{13}$$

where W depends on the potential shape but is independent of E. Thus, the conductance G of the bent nano-

tube depends linearly on E_F for very small E_F, in contrast with the ideal (rectilinear) nanotube. In the latter case, $G = G_0 = e^2/2\pi\hbar$ (per one spin projection) right from zero Fermi energy, because, in nanotubes, there exists a nontrivial solution of the Schrödinger equation for $E = 0$: $\psi_0 = 1/\sqrt{2\pi}$ (this is not the case for a 1D plane strip due to zero point energy).

Consider now the case $B < E_F < 4B$ (the second step in the conductance), when three channels are involved, $m = 0$ and $m = \pm 1$. It is easy to see that all perturbation terms in Eq. (7) contain only $\cos\varphi$ and, hence, preserve the parity of the solutions. That is why it is reasonable to choose three eigenfunctions of the zeroth approximation as[2] $\psi_0 = 1/\sqrt{2\pi}$, $\psi_+ = \cos\varphi/\sqrt{\pi}$, $\psi_- = \sin\varphi/\sqrt{\pi}$. Then, the ψ_- state is split off and we come to the following pair of coupled equations for the slow amplitudes c_0, c_+ (only leading terms of the expansion in $\alpha(s)$ are kept):

$$\begin{aligned} c_0'' - \sqrt{2}\alpha c_+'' + \left(k^2 - \frac{\alpha}{2a^2}\right)c_0 &= 0, \\ c_+'' - \sqrt{2}\alpha c_0'' + \left(q^2 - \frac{\alpha}{2a^2}\right)c_+ &= 0, \end{aligned} \qquad (14)$$

where $k^2 = 2\mu E/\hbar^2$, $q^2 = 2\mu(E - B)/\hbar^2 = k^2 - 1/a^2$.

Thus, the nanotube bending causes now both reflection of the electron waves and interchannel transitions. This results in distortion of the rectangular shape of the steps in the dependence $G(E_F)$. In the multichannel situation, $G(E_F)$ is given by the sum [6] $T_{00} + T_{++} + T_{--} + T_{0+} + T_{+0}$. System (14) has been analyzed for $\alpha(s)$ in the form of a rectangular barrier. However, it is easy to see that, due to the threshold character of the transitions under consideration, the results have a general meaning.

For E_F close to B, the transmission coefficient T_{00} may be set equal to 1 as the barrier height $\sim\alpha B \ll E_F$. The coefficients T_{++} and T_{--} in the region of onset of the second step ($E_F - B \ll B$) correspond to slow incoming particles and are described by formulas of type (13) with slightly changed W, as follows from Eqs. (9) and (10). Finally, T_{+0} relates to the interchannel scattering in the threshold regime (slow particle in the final state) and depends on energy as $\sqrt{E - B}$ (finite matrix element at $E \longrightarrow B$ times the ratio of the current densities in subbands ε_+ and ε_0).[3] The same is true for T_{0+}: everything is similar to the transmission of a quantum particle over a potential wall at an energy slightly exceeding the wall height. The latter in our case equals B, the separation between the bottoms of subbands ε_+ and ε_0. So, the leading contribution to the conductance comes from interchannel scattering and the second step in $G(E_F)$ starts as $G_0(1 + \text{const}\sqrt{E_F - B})$. This law holds only for $E_F - B \le \alpha B$. With increasing energy ($q^2a^2 \gg 1$), the coupling terms in Eqs. (13) become unimportant, T_{++}, T_{--} tend to 1 while T_{+0}, T_{0+} decrease, and $G(E_F)$ reaches its second quantized value for the rectilinear nanotube $3G_0$. It is clear that similar behavior of $G(E_F)$ should be expected at the onsets of all the other steps.

In conclusion, bending of a nanotube results in splitting of the energy subbands due to breaking of the azimuthal symmetry. Qualitative changes arise at the onset of each step in the staircase-like dependence of ballistic conductance of the nanotube on the Fermi energy.

This work was supported by the Russian Foundation for Basic Research (grant no. 16377), by the RF President grant for scientific schools, and by the Program "Nanostructures" of the Russian Ministry of Science and Education. I greatly appreciate the hospitality extended to me at the University of Aizu during my research visit. Also, I thank V.I. Ryzhii for valuable discussions.

REFERENCES

1. A. V. Chaplik and R. H. Blick, New J. Phys. **6**, 33 (2004).
2. H. Jensen and H. Koppe, Ann. Phys. (N.Y.) **46**, 586 (1971).
3. R. C. T. da Costa, Phys. Rev. A **23**, 1982 (1981).
4. M. V. Entin and L. I. Magarill, Phys. Rev. B **66**, 205308 (2002).
5. L. I. Magarill and M. V. Entin, Zh. Éksp. Teor. Fiz. **123**, 867 (2003) [JETP **96**, 766 (2003)].
6. M. Buttiker, Phys. Rev. Lett. **57**, 1761 (1986); IBM J. Res. Dev. **32**, 317 (1988).

[2] Here, "+" and "–" denote even and odd solutions, respectively.

[3] Strictly speaking, the density of current in a curvilinear system is changed ($\nabla_s = (1/h)\partial/\partial s$), but, asymptotically, at $s \longrightarrow \pm\infty$, we have $h = 1$.

JETP Letters, Vol. 80, No. 2, 2004, pp. 133–139. Translated from Pis'ma v Zhurnal Éksperimental'noĭ i Teoreticheskoĭ Fiziki, Vol. 80, No. 2, 2004, pp. 143–149.

ON THE RESULTS OF PROJECTS OF THE RUSSIAN FOUNDATION FOR BASIC RESEARCH, project no. 01-02-16356

Problem of Impurity States in Narrow-Gap Lead Telluride–Based Semiconductors

L. I. Ryabova and D. R. Khokhlov*

Moscow State University, Moscow, 119992 Russia

**e-mail: khokhlov@mig.phys.msu.ru*

Received June 9, 2004

A review of recent results of experimental investigations devoted to studying unusual properties of impurity states in doped narrow-gap lead telluride–based semiconductors is presented. These results are analyzed in the framework of existing theoretical concepts. © *2004 MAIK "Nauka/Interperiodica".*

PACS numbers: 71.55.-i; 71.23.An

1. Narrow-gap IV–VI semiconductors are materials unique in their physical properties, the diversity of effects observed in them, and the possibilities of practical use. In particular, these compounds are the basis for creating infrared semiconductor lasers that can operate at near-room temperatures, highly efficient thermoelectric converters, and highly efficient radiation detectors in the far-infrared and submillimeter ranges [1]. All the above possibilities are the consequence of a nontrivial combination of properties characteristic of the materials under consideration. These properties include the direct gap whose width can be smoothly varied by creating solid solutions, the high efficiency of radiative recombination, very high values of the static permittivity ε up to 10^4, and small effective masses of carriers $\sim 10^{-2} m_0$. As a result, the Coulomb potential of charged impurities in IV–VI semiconductors is almost completely screened. Therefore, it has no substantial effect on the mobility of carriers.

One of the important disadvantages of IV–VI semiconductors is the high concentration of defects in their structure. For standard synthesis methods, the concentration of vacancies and interstitial atoms reaches 10^{18}–10^{19} cm^{-3}. All the growth defects are electroactive, because of which the low carrier concentration necessary for a number of applications cannot be reached in undoped compounds.

Doping is one of the main methods for controlling the concentration of free carriers in semiconductors. The use of this method as applied to IV–VI semiconductors and, in particular, to lead telluride–based solid solutions not only allows the concentration of electrons and holes to be changed but also lead to the appearance of radically new properties uncharacteristic of the starting material.

When PbTe and a number of PbTe-based alloys are doped with group III impurities (indium, gallium, or thallium) and with some rare earth (Yb or Gd) and transition (Cr or Mo) elements, the effect of Fermi-level stabilization is observed. In this case, the Fermi-level position is determined by the alloy composition alone and is independent of the concentration of doping impurities and lattice defects [2]. In particular, a situation can arise when the Fermi level is stabilized within the band gap and a semi-insulating state is accomplished at low temperatures. Such a state is not observed in alloys that have not been specially doped.

In principle, heavy doping can lead in conventional semiconductors to the formation of a large-scale potential barrier and to the appearance of a drift barrier for carriers [3]. A paradoxical consequence of the effect of Fermi-level stabilization in lead telluride–based alloys is the high uniformity of electrophysical properties of the materials in spite of the heavy doping necessary for the appearance of the effect and the high concentration of defects [4]. This property is a consequence of the valence instability of impurity centers; that is, the fact that the charge state of impurities neutral with respect to the crystal lattice is unstable because of the high polarizability of the crystal lattice [5]. The balance between the amounts of impurity centers in different charge states is accomplished in such a way that the Fermi-level position is fixed at a certain place of the energy spectrum. This place is determined by the alloy composition alone, independent of the defect concentration.

The second most important effect determining the properties of lead telluride–based alloys doped with certain group III elements is the appearance of long-term relaxation processes in the semiconductor electron system when this system is disturbed from equilibrium

0021-3640/04/8002-0133$26.00 © 2004 MAIK "Nauka/Interperiodica"

at low temperatures [2]. The most prominent manifestation of this group of effects is persistent photoconductivity. Thus, the temperature dependences of the resistance measured in the dark and under infrared illumination substantially differ at temperatures $T < T_c$. The difference can reach six to eight orders of magnitude, depending on the alloy composition, doping level, etc. The temperature T_c is about 25 K for bulk crystals doped with indium and about 80 K for the gallium impurity. The appearance of such a strong photoresponse is a consequence of the fact that the lifetime of free nonequilibrium carriers at low temperatures sharply increases to values larger than 10^4 s. Thus, the photoexcited carriers are accumulated in the allowed band almost without recombination, which results in persistent photoconductivity.

2. A number of models have been proposed to explain the reasons for the appearance of long-term relaxation processes in doped lead telluride–based alloys.

Some authors [6–8] relate the appearance of persistent photoconductivity to the ferroelectric phase transition at the temperature T_c. Actually, the high permittivity of IV–VI materials is due to the closeness of the lattice to the phase transition to the rhombohedral phase. This transition in PbTe is a virtual one, and its temperature is ~130 K. However, in some PbTe-based alloys, in particular, in $Pb_{1-x}Ge_xTe$, such a transition is observed and its temperature is determined by the alloy composition. By the suggestion of the authors of [6–8], the introduction of an indium or gallium impurity can give rise to a similar phase transition. A particular mechanism relating the phase transition with the long lifetimes of nonequilibrium carriers was not discussed by the authors of [6–8]. The model under consideration encounter a large number of problems in the explanation of experimental facts. In particular, the independence of the temperature T_c from the amount of the added impurity finds no explanation [9]. However, studies that invoke this model to interpret the results obtained are still published [10].

A model explaining the appearance of long-term relaxation processes at low temperatures was proposed in [11]. In the framework of the concepts described in [11], the long lifetimes of nonequilibrium carriers at low temperatures are associated with the appearance of an autolocalization barrier arising when the impurity changes its charge state. When an impurity center is ionized, the configuration of the nearest crystal environment of the impurity atom is rearranged. In this case, for recombination to occur, an electron must overcome a barrier in the configuration space. This barrier is associated with the necessity for the crystal lattice to be polarized in the vicinity of an impurity center upon localization of a nonequilibrium electron. Various mechanisms of such polarization were proposed in a number of subsequent studies [12–15]; however, in principle, these mechanisms did not strongly differ from each other. It should be noted that a similar mechanism is also proposed for the explanation of long-term relaxation processes in III–V semiconductors with DX centers [16].

It was shown in [15, 17–19] that the results observed could not be explained in the framework of a model that takes into account the existence of only one local state. In particular, this is exhibited in the fact that the photoresponse decay kinetics after switching off illumination consists of two sections: fast (~1–10 ms) and slow (from 10 ms to 10^4 s, depending on temperature) conductivity relaxation. In order to describe this and a number of other experimental results, an essential amendment [15] was introduced into the model [11]. According to [15], in addition to the ground impurity state, which is a two-electron state and provides Fermi-level stabilization, there is also a metastable one-electron impurity state. This state is separated by a barrier in the configuration space from both the ground two-electron local state and the state with delocalized carriers in the allowed band. In this case, the localization of photoexcited carriers proceeds in two steps through an intermediate metastable one-electron state. The section of fast photoconductivity relaxation corresponds to recombination into the metastable local state, whereas the section of slow relaxation corresponds to recombination into the ground impurity state.

The energy position of the metastable impurity state and the height of the barriers separating it from the ground local state and from the band states were the subject of consideration in a number of articles [15, 17–20]; however, an integral picture was not obtained. Thus, according to one group of data [15, 17, 18], the metastable one-electron impurity state in $Pb_{1-x}Sn_xTe(In)$ alloys is positioned rather high in the conduction band, and, according to other studies [19, 20], it virtually coincides in energy with the conduction band bottom and is separated from the delocalized states by only a low barrier of ~1 meV.

In order to resolve this contradiction, a somewhat different concept was proposed in [21]. The model [21] was based on the fact that the actual bands in lead chalcogenides are almost entirely constructed from atomic *p* orbitals. In doping, an atom of group III impurities substitutes for a lead atom in the materials indicated above. The effect of Fermi-level stabilization is caused by the fact that the charge state of an impurity atom Im^{2+} neutral with respect to the crystal lattice is unstable and decays according to the reaction $2Im^{2+} \longrightarrow Im^{+} + Im^{3+}$.

In terms of atomic orbitals, the Im^{2+} state corresponds to the electronic configuration s^1p^2, the Im^{+} state corresponds to the configuration s^2p^1, and the Im^{3+} state corresponds to s^0p^3. The lead atom that substitutes for an impurity corresponds to the configuration s^2p^2. The actual bands in lead chalcogenides are almost entirely constructed of atomic *p* orbitals; therefore, for various

charged states of an impurity atom, electrons that occupy the deeply lying *s* shell are localized and *p* electrons are delocalized.

The main idea of the model [21] is that the one-electron impurity state in which only one electron occupies the *s* shell is positioned in energy in the one-electron approximation significantly higher than the ground two-electron state and higher than the conduction band bottom (Fig. 1). Then, in the photoionization of the first electron from an impurity center, it must be supplied with an energy necessary, first, for the excitation of this electron to the conduction band and, secondly, for transferring the impurity center to the state corresponding one *s* electron localized on the impurity. One *s* electron remained on the impurity center rapidly passes to the conduction band, whose bottom lies lower in energy. Thus, two nonequilibrium electrons appear in the conduction band. Recombination is a one-electron process; however, in order for an impurity center to trap an electron, it must be supplied with an energy equal to the distance between the quasi-Fermi level and the one-electron impurity state. In fact, it is this energy gap that prevents fast electron recombination on the center.

However, the reasons for the appearance of two sections of photoconductivity relaxation remain unclear in the framework of the model outlined above. The possible resolution of this contradiction is as follows. Fermi-level stabilization implies that a significant amount of gallium atoms has an empty *s* shell. Two *p* electrons with oppositely directed spins can be localized in the short-range attractive potential of this shell [22]. However, because of the high permittivity and the small effective electron mass in PbTe, a single impurity center with an empty *s* shell might not create a bound state. At the same time, the amount of such centers is rather large, and one bound state of *p* electrons can be formed for a great (to 10^3–10^4) number of impurity centers with an empty *s* shell [23]. Then, fast photoconductivity relaxation can be due to the localization of part of the photoexcited electrons in these bound states, which are positioned in energy near the conduction band bottom and are shallow in this sense.

3. Lately, the body of experimental information on nonequilibrium processes in lead telluride–based solid solutions doped with indium and gallium has been significantly increased. In particular, new data have appeared on the spectral sensitivity of $Pb_{1-x}Sn_xTe(In)$ single crystals [24], on the character of the photoconductivity (PC) of PbTe(Ga) epitaxial layers differing in thickness and in doping level [25–27], on the ferroelectric phase transition in $Pb_{1-x}Ge_xTe(Ga)$ [28, 29]. These results allow a theoretical model to be selected out of the existing variety that most adequately and unambiguously describes the set of available experimental results.

The detection of a photoresponse in a $Pb_{0.75}Sn_{0.25}Te(In)$ film at wavelengths of 176 and 241 μm was reported in [24]. The $Pb_{0.75}Sn_{0.25}Te(In)$ film was grown by molecular-beam epitaxy on a BaF_2 substrate. The thermal activation energy of the ground impurity state calculated using the relationship $\rho \sim \exp(E_a/2kT)$ was 20 meV. The experiment was performed using an installation in which the background radiation was completely screened. The source of infrared radiation was a blackbody with a temperature of 77 or 300 K. The narrow spectral band of the radiation incident on the sample was provided with the use of a series of cooled filters. The build-up kinetics of the current through the sample was measured in time at various values of the voltage across the sample and various temperatures of the blackbody. The experimental results for a voltage across the sample of 10 mV at a blackbody temperature of 300 K are given in Fig. 2.

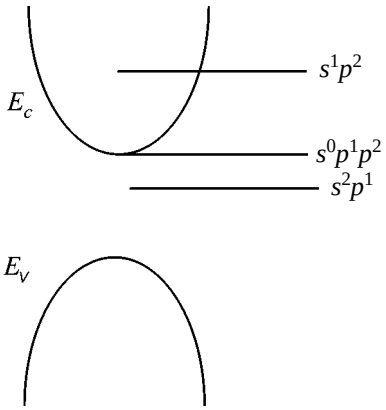

Fig. 1. Model of the energy spectrum of an impurity center in PbTe(Ga) [21].

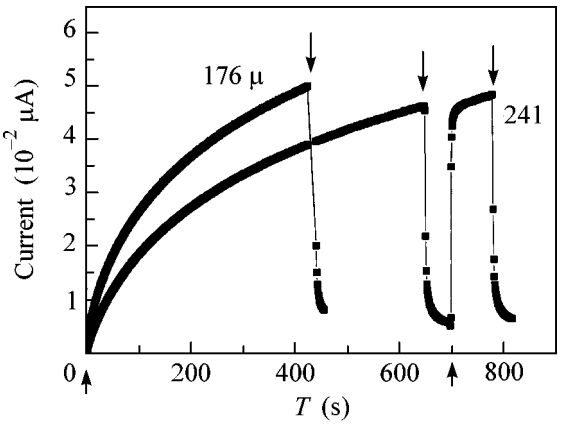

Fig. 2. Photocurrent build-up and decay kinetics at a voltage of 10 mV across a $Pb_{0.75}Sn_{0.25}Te(In)$ sample and various exciting radiation wavelengths. Arrows show the instants of switching on and switching off infrared illumination [24].

A significant photoresponse was detected for both wavelengths of the radiation incident on the sample. A number of PC features attract attention. First, the kinet-

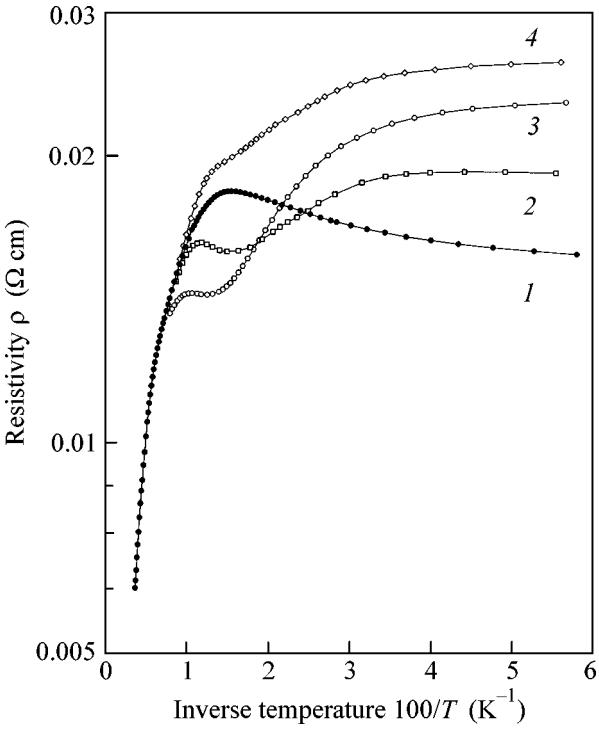

Fig. 3. Temperature dependences of the resistivity ρ(100/*T*) of an *n*-PbTe(Ga) sample; curve *1* was obtained in the dark, curves *2* and *3* were obtained under continuous illumination conditions (by a miniature incandescent lamp) with a varying (increasing) intensity, and curve *4* was obtained upon heating in the dark after switching off the source of IR illumination at $T = 4.2$ K [27].

ics of current build-up in time after switching on illumination is strongly nonlinear. Switching off illumination leads to fast photocurrent decay followed by slow relaxation to the dark value. However, if, shortly after being switched off, illumination is switched on again, the photocurrent very rapidly (in a time comparable with the fast relaxation time) increases to the value measured before switching off illumination. After that, the previous, relatively slow photocurrent build-up dynamics is restored. Evidently, the fast and slow relaxation processes are essentially different in nature.

The second important issue is in the following. The quantum energy corresponding to radiation wavelengths of 176 and 241 μm is considerably lower than the thermal activation energy of the ground impurity state. Thus, the results reported in [24] are direct evidence that the persistent PC in $Pb_{1-x}Sn_xTe$(In) can be caused by the photoexcitation of metastable impurity states. The boundary optical excitation energy of these states is very low. The wavelength of the corresponding radiation quantum is at least larger than 241 μm, which is the highest value for the photoelectric threshold in nonthermal radiation detectors. It is most likely that the threshold of photosensitivity in these materials is located at considerably larger wavelengths. It is not inconceivable that the working range of $Pb_{1-x}Sn_xTe$(In)-based photodetectors covers the entire submillimeter region.

At the same time, the nature of the appearance of two sections of free-electron generation and recombination in this case remains unclear, because the ground impurity state must be excluded from consideration by virtue of the smallness of the exciting quantum energy.

A distinctive feature of PbTe(Ga) is the rather narrow concentration range of the doping impurity in which the effect of Fermi-level stabilization is manifested. As the gallium concentration in the samples increases, a sharp growth is observed in the electron concentration. This growth can be caused by the fact that the excess gallium starts to behave as an active donor. In single-crystal samples at a small excess of doping, it was not possible to accomplish the state with low electron concentrations corresponding to the removal of the effect of stabilization. In the case of films, it was possible to vary the impurity concentration significantly more smoothly and to obtain a series of samples corresponding to a certain intermediate state between the stabilized Fermi-level position and the *n*-type metallic conductivity [27].

A study of photoelectric processes showed that the kinetics of PC signal decay after switching off illumination in semi-insulating films as well as in single-crystal samples includes a relatively fast section followed by persistent photoconductivity [25]. Under pulse illumination, a rapidly relaxing signal dominates. Various ratios between the amplitudes of the rapidly relaxing signal and the persistent PC itself can be obtained by changing the experimental conditions (pulse duration, the type of the radiation source, temperature, etc.). However, both in single crystals and in films several microns thick, the PC relaxation is of nonexponential character. The situation changes qualitatively in sufficiently thin layers with $d \sim 0.2$ μm. Almost immediately after the passage of an illumination pulse, the signal decay is described by exponential kinetics $\Delta\sigma(t) \propto \exp(-t/\tau)$. At $T = 4.2$ K, the fast relaxation time is 13 ms [26].

The data obtained correspond to the concept of variable valence of the gallium impurity. The impurity centers in different charge states are responsible for the occurrence of several recombination channels. The nonuniform distribution of carriers in the bulk in combination with the nonuniform distribution of impurity centers in different charge states can lead to nonequivalent conditions for the recombination of different groups of carriers and to a substantial modification of kinetic processes. Evidently, the spatial uniformity of the distribution of nonequilibrium carriers and charged impurity centers is accomplished only in sufficiently thin layers with $d \le 0.2$ μm.

In relatively low-resistance PbTe(Ga) samples characterized by an increased gallium concentration, the PC is qualitatively different from that in semi-insulating

layers [27]. Figure 3 demonstrates temperature dependences of the resistivity for one of the low-resistance films (d = 2 μm). Along with the dark curve (*1*), the figure displays dependences measured at different illumination intensities (*2*, *3*). In the region of low temperatures, an increase in the film resistance (negative PC) is observed upon switching on illumination. As the temperature increases, the amplitude of negative PC decreases, PC disappears (the intersection point of curves *1–2* or *1–3*), and positive PC is observed as T further increases. In fact, the positive and negative PC components coexist even at low temperatures, but the contribution of negative PC dominates. This is evidenced by the fact that the resistivity ρ at T = 4.2 K attains its maximum value after switching off illumination (see Fig. 3, curve *4*). It is seen in the figure that persistent negative PC was observed up to $T \sim 100$ K.

The coexistence of the contributions of positive and negative PC at low temperatures is revealed even more clearly in studies of PC kinetics (Fig. 4). It is evident that only positive PC is observed at a temperature of 77 K. However, as the temperature decreases to 4.2 K, the initial signal of positive PC changes its sign already approximately in 0.5 s. Negative PC is observed subsequently, and this PC is persistent: the fast relaxation of part of positive PC occurs after switching off illumination, and the resistance of the sample increases even more as compared with the dark state.

It should be noted that persistent negative PC detected in relatively low-resistance PbTe(Ga) layers is not an unusual effect in semiconducting samples. It was rather frequently observed in recombination barrier systems. In particular, in heterogeneous semiconductors in which nonequilibrium carriers existed for one or another reason, the recombination of spatially separated electron–hole pairs could be hindered because of the modulation of the band relief, and additional illumination allowed carriers to overcome this barrier. A similar situation can arise in quantum well systems and in polycrystalline samples. However, persistent negative PC in all the above cases is observed only under quasi-equilibrium conditions in the presence of nonequilibrium carriers excited earlier by another external action. The fast component of negative PC detected in low-resistance PbTe(Ga) layers under pulse illumination conditions [27] may be considered a more interesting phenomenon. Under pulse illumination conditions, rapidly relaxing negative PC dominates and the instant relaxation times are of the order of tens of microseconds, which is three orders of magnitude shorter than the corresponding times of the fast component of positive PC in semi-insulating PbTe(Ga) samples [25, 26]. Such a fast recombination process cannot be explained within the models that suggest the spatial separation of nonequilibrium carriers. The recombination character must be determined by the energy spectrum structure of impurity states.

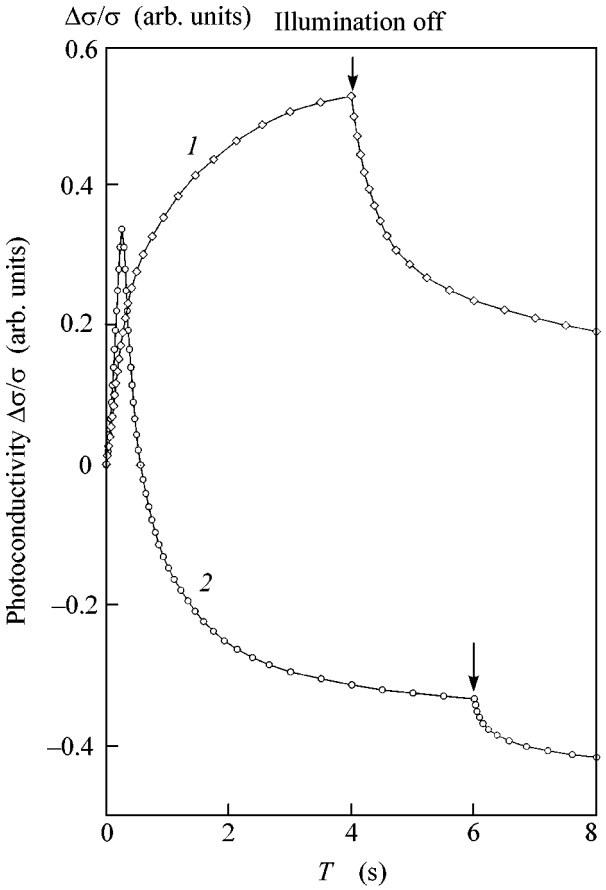

Fig. 4. Photoconductivity kinetics $\Delta\sigma(t)$ under illumination by a miniature incandescent lamp for an *n*-PbTe(Ga) sample (see Fig. 3) at various temperatures: (*1*) 77 and (*2*) 4.2 K; the instant of switching off illumination is shown by vertical arrows [27].

The observed phenomena can be best understood under the assumption that the generation and recombination of nonequilibrium carriers in both PbTe(Ga) single crystals and epitaxial films are determined by electron transitions in the system of two allowed bands and three impurity levels (see Fig. 1). In this case, the density of states on impurity levels can vary in the course of relaxation and can be spatially nonuniform. Under these conditions, one can observe rather exotic phenomena, such as, for example, the rapid decay of the negative PC signal. Thus, the model [21] allows all the main experimental facts to be described at a qualitative level. Unfortunately, it is hardly possible to develop a strict quantitative description, because it would require the determination of many microscopic parameters and their time and coordinate dependences.

In conclusion, we will consider the problem of the possible effect of the ferroelectric phase transition on the nonequilibrium processes. The total impedance of bulk PbTe(Ga) and $Pb_{1-x}Ge_xTe$(Ga) single crystals (x = 0.04–0.10) was studied in [28, 29] in the frequency range from 10^2 to 10^6 Hz at temperatures from 4.2 to

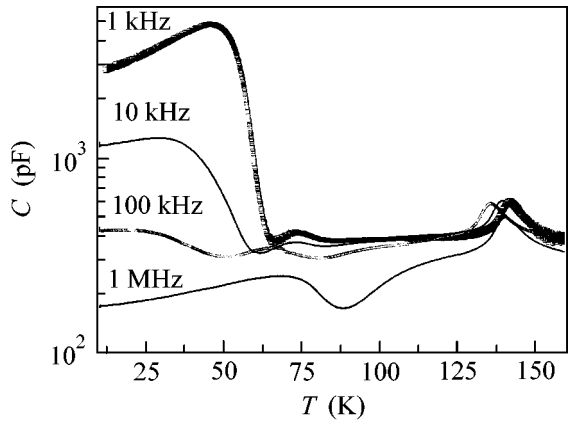

Fig. 5. Temperature dependences of the capacity for a $Pb_{0.94}Ge_{0.06}Te(Ga)$ sample. Numbers by the curves indicate the measurement frequencies. The geometrical capacity of the sample $C_0 = 0.18$ pF [28].

300 K. Two types of features were detected in the temperature dependences of the capacity in all the studied $Pb_{1-x}Ge_xTe(Ga)$ samples. These were a pronounced peak at the temperature $T = T_P$, which was due to the permittivity anomaly at the ferroelectric phase transition, and an increase in the capacity in the region of low temperatures $T < 100$ K, which was characterized by a strong frequency dependence. As an example, Fig. 5 demonstrates rather typical temperature dependences of the capacity for a $Pb_{1-x}Ge_xTe(Ga)$ sample with $x = 0.46$. For all the studied compositions of $Pb_{1-x}Ge_xTe(Ga)$ samples, the temperature of the ferroelectric phase transition proved to be close to the data reported in the literature for undoped samples. In this case, T_P exhibits a strong dependence on the composition X. The amplitude of the low-temperature effect decreases monotonically with increasing frequency f, and the effect virtually disappears at $f > 10^5$ Hz. The contribution to the capacity at such low frequencies can be associated with charge exchange processes in the impurity subsystem. It is important that the value of T_P determined experimentally proved to be substantially higher than the characteristic temperatures of the appearance of long-term relaxation processes, in particular, persistent PC. That is, the change of charge states in the impurity subsystem is not accompanied with permittivity anomalies of the crystal lattice as a whole, and the possible rearrangement of the lattice is of local character.

Thus, the model proposed in [21] can be currently considered to be most consistent with experimental data for lead telluride–based solid solutions doped with indium and gallium. It is important to note that this model is also best defined from the point of view of microscopic impurity states.

This work was partially supported by the Russian Foundation for Basic Research, project nos. 04-02-16497 and 02-02-17057, and by INTAS, project no. 2001-0184.

REFERENCES

1. *Lead Chalcogenides: Physics and Applications*, Vol. 18 of *Optoelectronic Properties of Semiconductors and Superlattices*, Ed. by D. Khokhlov (Taylor and Francis, New York, 2003).
2. B. A. Volkov, L. I. Ryabova, and D. R. Khokhlov, Usp. Fiz. Nauk **172**, 857 (2002) [Phys. Usp. **45**, 819 (2002)].
3. M. K. Sheĭkman and A. Ya. Shik, Fiz. Tekh. Poluprovodn. (Leningrad) **10**, 208 (1976) [Sov. Phys. Semicond. **10**, 128 (1976)].
4. B. A. Akimov, N. B. Brandt, K. R. Kurbanov, *et al.*, Fiz. Tekh. Poluprovodn. (Leningrad) **17**, 1604 (1983) [Sov. Phys. Semicond. **17**, 1021 (1983)].
5. I. A. Drabkin and B. Ya. Moĭzhes, Fiz. Tekh. Poluprovodn. (Leningrad) **17**, 969 (1983) [Sov. Phys. Semicond. **17**, 611 (1983)].
6. K. H. Herrmann and K.-P. Moellmann, Phys. Status Solidi A **91**, K147 (1985).
7. A. N. Vasil'ev, Yu. P. Gaĭdukov, and V. N. Nikiforov, Pis'ma Zh. Éksp. Teor. Fiz. **41**, 466 (1985) [JETP Lett. **41**, 568 (1985)].
8. K. H. Herrmann and K.-P. Moellmann, Phys. Status Solidi A **80**, K101 (1983).
9. B. A. Akimov, A. V. Albul, A. V. Nikorich, *et al.*, Fiz. Tekh. Poluprovodn. (Leningrad) **18**, 1778 (1984) [Sov. Phys. Semicond. **18**, 1112 (1984)].
10. A. E. Klimov and V. N. Shumsky, Proc. SPIE **5126**, 341 (2003).
11. Yu. M. Kagan and K. A. Kikoin, Pis'ma Zh. Éksp. Teor. Fiz. **31**, 367 (1980) [JETP Lett. **31**, 335 (1980)].
12. V. I. Litvinov and K. D. Tovstyuk, Fiz. Tverd. Tela (Leningrad) **24**, 896 (1982) [Sov. Phys. Solid State **24**, 508 (1982)].
13. O. A. Pankratov and M. G. Foĭgel', Fiz. Tekh. Poluprovodn. (Leningrad) **18**, 1203 (1984) [Sov. Phys. Semicond. **18**, 752 (1984)].
14. O. A. Pankratov and B. A. Volkov, Sov. Sci. Rev., Sect. A **9**, 355 (1987).
15. I. I. Zasavitskiĭ, B. N. Matsonashvili, O. A. Pankratov, *et al.*, Pis'ma Zh. Éksp. Teor. Fiz. **42**, 3 (1985) [JETP Lett. **42**, 1 (1985)].
16. P. M. Mooney, J. Appl. Phys. **67**, R1 (1990).
17. I. I. Zasavitskiĭ, A. V. Matveenko, B. N. Matsonashvili, *et al.*, Fiz. Tekh. Poluprovodn. (Leningrad) **20**, 214 (1986) [Sov. Phys. Semicond. **20**, 135 (1986)].
18. V. N. Vinchakov, V. I. Kaĭdanov, S. N. Lykov, *et al.*, Pis'ma Zh. Éksp. Teor. Fiz. **43**, 384 (1986) [JETP Lett. **43**, 495 (1986)].
19. B. A. Akimov, A. V. Nikorich, D. R. Khokhlov, *et al.*, Fiz. Tekh. Poluprovodn. (Leningrad) **23**, 668 (1989) [Sov. Phys. Semicond. **23**, 418 (1989)].
20. A. I. Belogorokhov, E. I. Slyn'ko, and D. R. Khokhlov, Pis'ma Zh. Tekh. Fiz. **18** (8), 30 (1992) [Sov. Tech. Phys. Lett. **18**, 252 (1992)].

21. A. I. Belogorokhov, B. A. Volkov, I. I. Ivanchik, and D. R. Khokhlov, Pis'ma Zh. Éksp. Teor. Fiz. **72**, 178 (2000) [JETP Lett. **72**, 123 (2000)].

22. B. A. Volkov and O. M. Ruchaĭskiĭ, Pis'ma Zh. Éksp. Teor. Fiz. **62**, 205 (1995) [JETP Lett. **62**, 217 (1995)].

23. A. I. Byaz', Ya. B. Zel'dovich, and A. M. Perelomov, *Scattering, Reactions and Decays in Nonrelativistic Quantum Mechanics*, 2nd ed. (Nauka, Moscow, 1971; Israel Program for Scientific Translations, Jerusalem, 1966).

24. K. G. Kristovskiĭ, A. E. Kozhanov, D. E. Dolzhenko, *et al.*, Fiz. Tverd. Tela (St. Petersburg) **46**, 123 (2004) [Phys. Solid State **46**, 122 (2004)].

25. B. A. Akimov, V. A. Bogoyavlenskiy, L. I. Ryabova, *et al.*, Semicond. Sci. Technol. **19**, 679 (1999).

26. B. A. Akimov, V. A. Bogoyavlenskiĭ, L. I. Ryabova, *et al.*, Fiz. Tekh. Poluprovodn. (St. Petersburg) **35**, 524 (2001) [Semiconductors **35**, 502 (2001)].

27. B. A. Akimov, V. A. Bogoyavlenskiy, L. I. Ryabova, *et al.*, Phys. Rev. B **61**, 16045 (2000).

28. B. A. Akimov, V. V. Pryadun, L. I. Ryabova, and D. R. Khokhlov, Fiz. Tekh. Poluprovodn. (St. Petersburg) **38**, 293 (2004) [Semiconductors **38**, 281 (2004)].

29. B. A. Akimov, V. V. Pryadun, L. I. Ryabova, *et al.*, Fiz. Nizk. Temp. (in press).

Translated by A. Bagatur'yants

JETP Letters, Vol. 80, No. 2, 2004, pp. 67–72. From Pis'ma v Zhurnal Éksperimental'noĭ i Teoreticheskoĭ Fiziki, Vol. 80, No. 2, 2004, pp. 75–80.

The Role of Finite Kinematic Bounds in the Induced Gluon Emission from Fast Quarks in a Finite Size Quark–Gluon Plasma¶

B. G. Zakharov

Landau Institute for Theoretical Physics, Russian Academy of Sciences, Moscow, 117334 Russia

Received June 7, 2004

We study the influence of finite kinematic boundaries on the induced gluon radiation from a fast quark in a finite size quark–gluon plasma. The calculations are carried out for fixed and running coupling constant. We find that, for running coupling constant, the kinematic correction to the radiative energy loss is small for quark energy $\gtrsim$5 GeV. Our results differ both analytically and numerically from that obtained by the GLV group [6]. The effect of the kinematic cutoffs is considerably smaller than reported in [6]. *© 2004 MAIK "Nauka/Interperiodica".*

PACS numbers: 12.38.Mh

1. It is very likely that parton energy loss due to the induced gluon radiation caused by multiple scattering [1–7] plays a major role in suppression of high-p_T hadron spectra in heavy-ion collisions observed at RHIC [8, 9]. There is an attractive idea [10] to use this phenomenon (usually called "jet-quenching") to obtain information about the density of hot quark–gluon plasma (QGP) produced in *AA*-collisions. Such a jet tomographic analysis requires accurate methods for evaluating the induced gluon emission. In recent years, this problem has been attacked from several directions. In [3] (see also [11–13]), we have developed a light-cone path integral (LCPI) approach to the induced radiation. The induced gluon spectrum was expressed through a solution of a two-dimensional Schrödinger equation in the impact parameter space with an imaginary potential. This approach accounts for the Landau–Pomeranchuk–Migdal (LPM) effect [14, 15], finite-size and mass effects which are important for the QGP produced in *AA*-collisions. In [2, 5], the radiative energy loss was addressed using diagrammatic formalism. Similarly to the LCPI approach, the BDMPS approach [2, 5] expresses the gluon spectrum through a solution of a two-dimensional Schrödinger equation in the impact parameter space. However, the BDMPS formalism applies only in the limit of strong LPM suppression. In this regime, it is equivalent [5, 13] to the approach [3]. The GLV group [6] has developed, within the soft gluon approximation, an approach in momentum space which applies to thin plasmas when the mean number, $\bar{N}$, of jet scatterings is small, and performed calculations accounting for the $N = 1, 2, 3$ rescatterings.

For applications of the formalisms [3, 5, 6] to the tomographic analysis of experimental data on *AA*-collisions, it is important to understand the limits of applicability of these approaches. In the analyses [3, 5, 6], the QGP is modeled by a system of Debye screened color centers [1], and parton scattering is treated in the small-angle approximation. The LCPI [3] and BDMPS [2, 5] approaches, formulated in the impact parameter space, in addition, imply that the integration over the transverse momenta can be extended up to infinity ignoring finite kinematic boundaries. The small-angle approximation for fast partons moving through the medium should work well for parton energy $E \gg \mu_D$, where μ_D is the Debye screening mass which plays the role of a natural infrared cutoff and energy scale for parton scatterings in the QGP. For RHIC and LHC conditions, where $\mu_D \sim 0.5$ GeV [16], it means $E \gtrsim 3$–5 GeV. It is, however, not clear whether the approximation of static color centers neglecting recoil effects is adequate for $E \sim 5$ GeV. For such energies, the kinematic constraints on the momentum transfer $q \lesssim q_{\max} \sim \sqrt{EE_{\rm th}}$, where $E_{\rm th} \approx 3T$ is the typical thermal energy of quarks and gluons in the QGP, may be important. The GLV group [6] has reported that the kinematic cutoffs suppress greatly the parton energy loss, ΔE. Even at $E \sim 1000\ \mu_D$ for the leading $N = 1$ contribution to ΔE for a homogeneous QGP with thickness $L \approx 5$ fm, the authors have found the suppression ~0.5, and, for $E \sim 10\ \mu_D$, they give the suppression ~0.16.

The approaches [3, 5] become inapplicable when the kinematic bounds become important. The GLV formalism [6], which does not treat accurately parton scattering near the kinematic limit, also cannot be used for quantitative calculations in this regime. Thus, if the

¶ This article was submitted by the author in English.

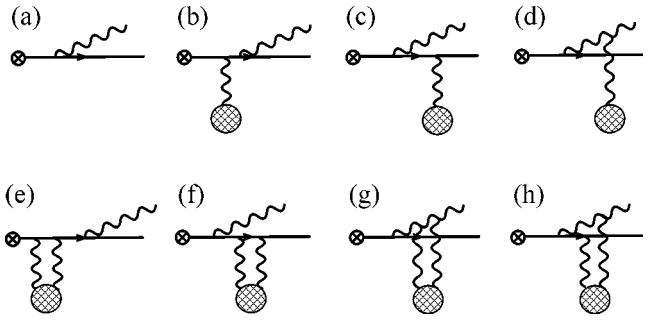

Fig. 1. The set of the Feynman diagrams for the $N = 1$ contribution to the induced gluon spectrum.

kinematic effect were as strong as found in [6], the available approaches to the induced radiation would be inapplicable even at LHC energies. For this reason, the kinematic effect merits further investigations. In particular, it is clearly desirable to study the effect of the running coupling constant. The decrease of the coupling constant near the kinematic bounds should act as a natural cutoff of large parton transverse momenta and diminish the role of the recoil effects. Another remaining open question is related to the different cutoffs for the initial and final partons. The authors of [6] have used for scattering of the radiated gluon the same cutoff in the momentum transfer as that for the initial parton. However, for soft gluons with $x \ll 1$ (hereafter, x is the gluon fractional momentum), the $q_{\max}$ is considerably smaller than for the initial parton. In the present paper, we address the role of the kinematic cutoffs accounting for the running coupling constant and different cutoffs for the initial and final partons. The analysis is performed for the $N = 1$ scattering which dominates the induced spectrum for RHIC and LHC conditions. We find that, although the difference in the initial and final state cutoffs changes the analytical form of the induced spectrum, numerically the effect is insignificant. For fixed coupling constant, the kinematic corrections become important for $E \lesssim 10$–20 GeV, and, for running one, the kinematic effect is small even at $E \sim 5$ GeV. We find that the kinematic effect is considerably smaller than found in [6].

2. We consider a fast quark with energy E produced at $z = 0$ (we choose the z-axis along the momentum of the quark) traversing a medium of thickness L, which eventually splits into a gluon and final quark with the energies xE and $(1 - x)E$, respectively. We assume that parton energies are much larger than the thermal quasiparticle masses in the QGP. The $N = 1$ induced spectrum can be represented in the form

$$\frac{dP}{dx} = \int_0^L dz n(z) \frac{d\sigma^{BH}(x, z)}{dx}, \tag{1}$$

where $n(z)$ is the number density of the medium (the summation over the triplet (quark–antiquark) and octet (gluon) color states is implied on the right-hand side of (1)), and $d\sigma^{BH}(x, z)/dx$ is the in-medium (z-dependent) Bethe–Heitler cross section. It can be written as

$$\frac{d\sigma^{BH}(x, z)}{dx} = J_{bb} + J_{cc} + J_{dd} + 2J_{bc} + 2J_{cd} + 2J_{db} + 2J_{ae} + 2J_{af} + 2J_{ag} + 2J_{ah}, \tag{2}$$

with $J_{\alpha\beta}$ given by

$$J_{\alpha\beta} = \frac{E}{(2\pi)^5} \mathrm{Re} \int d\mathbf{q} d\mathbf{p} T_\alpha(\mathbf{q}, \mathbf{p}) T_\beta^*(\mathbf{q}, \mathbf{p}), \tag{3}$$

where the amplitudes T_α diagrammatically are shown in Fig. 1, $\mathbf{q}$ and $\mathbf{p}$ are the transverse momenta of the t-channel and emitted gluons, respectively. Note that the interference between the double-gluon exchange diagrams (e), (f), (g), (h) and the diagram without gluon exchange (a) is important to ensure unitarity.

The diagrams of Fig. 1 can be evaluated with the help of the ordinary perturbative formula

$$T = \int_0^\infty dz' \int d\boldsymbol{\rho} g \bar{\psi}_f(\boldsymbol{\rho}, z') \gamma^\mu A_\mu(\boldsymbol{\rho}, z') \psi_i(\boldsymbol{\rho}, z'), \tag{4}$$

where $\boldsymbol{\rho}$ is the transverse coordinate, $\psi_{i,f}(\boldsymbol{\rho}, z')$ are the wave functions of the initial and final quarks, and $A_\mu(\boldsymbol{\rho}, z')$ is the wave function of the emitted gluon (hereafter, we omit the color factors and spin indices). In (4), we do not explicitly indicate the dependence of the wave functions on the position of the scattering center. The quark wave functions using the light-cone spinor basis can be written as

$$\psi_j(\boldsymbol{\rho}, z') = \exp(iE_j z') \hat{U}_j \phi_j(\boldsymbol{\rho}, z'), \tag{5}$$

where the operator $\hat{U}_j$ reads

$$\hat{U}_j = \left(1 + \frac{\boldsymbol{\alpha}\mathbf{p} + \beta m_q}{2E_j}\right) \chi_j. \tag{6}$$

Here, χ_j is the quark spinor (normalized to unity), $\boldsymbol{\alpha} = \gamma^0 \boldsymbol{\gamma}$, $\beta = \gamma^0$, and $\mathbf{p} = -i\nabla_\perp$. The transverse wave function $\phi_j(\boldsymbol{\rho}, z')$ entering (5) is governed by the two-dimensional Schrödinger equation in which z' plays the role of time

$$i \frac{\partial \phi_j(\boldsymbol{\rho}, z')}{\partial z'} = \left[\frac{(\mathbf{p}^2 + m_q^2)}{2E_j} + v(\boldsymbol{\rho}, z')\right] \phi_j(\boldsymbol{\rho}, z'), \tag{7}$$

where

$$v(\boldsymbol{\rho}, z') = \delta(z' - z) \int \frac{d\mathbf{q}}{(2\pi)^2} \exp(i\mathbf{q}\boldsymbol{\rho}) v(\mathbf{q}),$$
$$v(\mathbf{q}) = \frac{4\pi\alpha_s(q)}{\mathbf{q}^2 + \mu_D^2}, \tag{8}$$

is the potential generated by the one-gluon exchange between quark and the Debye screened color center. In the longitudinal direction, we treat the potential as a pointlike. In the same form, one can represent the gluon wave function (up to an obvious change of the spin operator and color factors).

The amplitudes entering (3) can be easily obtained from (4) treating in (7) the potential v as a perturbation. For the diagrams with gluon exchanges in the z' regions $0 < z' < z$ and $z' > z$, the transverse wave functions are given by the plane waves (with different transverse momenta in these two regions of z')

$$\phi_j(\boldsymbol{\rho}, z') \propto \exp\left\{i\left[\mathbf{p}_j\boldsymbol{\rho} - z'\frac{(\mathbf{p}_j^2 + m_j^2)}{2E_j}\right]\right\}. \quad (9)$$

The color center acts as a kick which changes the quark (or gluon) transverse momentum at $z' = z$. The corresponding amplitude $\propto v(\mathbf{q})$ for one-gluon exchange diagrams and $\propto \int d\mathbf{p}\, v(\mathbf{p}) v(\mathbf{q} - \mathbf{p})$ for the double-gluon exchange ones. Note that, eventually, the $\boldsymbol{\rho}$-integration in (4) ensures conservation of the transverse momentum.

To account for the kinematic boundaries, we introduce in the amplitudes the cutoff factors. For each t-channel gluon, we modify the propagator introducing the cutoff factor $\theta(q_{\max} - q)$. Here, $q_{\max}$ is the upper kinematic bound on the momentum transfer for the parton to which the t-channel gluon is attached. Also, we modify the qqg-vertex for splitting the initial fast quark into quark–gluon system introducing the cutoff factor $\theta(k_{\max} - k)$, k is the transverse momentum of the gluon in the frame where the total transverse momentum of the quark–gluon state equals zero, and $k_{\max} = E\min(x, 1 - x)$ (here, E is the initial quark energy). The above prescription ensures that parton scattering angles are small, and the momentum transfer does not exceed the kinematic bounds.

Using (2)–(8) after straightforward but a bit cumbersome calculations, the effective Bethe–Heitler cross section can be represented in the form

$$\frac{d\sigma^{BH}(x, z)}{dx} = \frac{d\sigma_1^{BH}(x, z)}{dx} + \frac{d\sigma_2^{BH}(x, z)}{dx}, \quad (10)$$

where

$$\frac{d\sigma_1^{BH}(x, z)}{dx} = \frac{2C_T}{\pi^2 x}\left(1 - x + \frac{x^2}{2}\right)$$

$$\times \int d\mathbf{q}\, d\mathbf{k} \frac{\alpha_s^2(q)}{(\mathbf{q}^2 + \mu_D^2)^2}\Big[\theta(q_3 - q)F(\mathbf{k}, \mathbf{q}, z) + \theta(q_1 - q)F(\mathbf{k}, \mathbf{q}(1 - x), z) \quad (11)$$

$$- \frac{1}{N_c^2}\theta(q_2 - q)F(\mathbf{k}, \mathbf{q}x, z)\Big],$$

$$F(\mathbf{k}, \mathbf{q}, z) = \left[\frac{\mathbf{k}^2\Theta^2(\mathbf{k})}{(\mathbf{k}^2 + \epsilon^2)^2} - \frac{(\mathbf{k} - \mathbf{q})\mathbf{k}\Theta(\mathbf{k})\Theta(\mathbf{k} - \mathbf{q})}{(\mathbf{k}^2 + \epsilon^2)((\mathbf{k} - \mathbf{q})^2 + \epsilon^2)}\right] \times \left[1 - \cos\left(\frac{iz}{l(\mathbf{k}, x)}\right)\right], \quad (12)$$

$$\frac{d\sigma_2^{BH}(x, z)}{dx} = \frac{2C_T}{C_A\pi^2 x}\left(1 - x + \frac{x^2}{2}\right)$$

$$\times \int d\mathbf{q} \frac{\alpha_s^2(q)}{(\mathbf{q}^2 + \mu_D^2)^2}[C_F(\theta(q_0 - q) - \theta(q_2 - q)) + C_A(\theta(q_2 - q) - \theta(q_3 - q))] \quad (13)$$

$$\times \int d\mathbf{k} \frac{\mathbf{k}^2\Theta^2(\mathbf{k})}{(\mathbf{k}^2 + \epsilon^2)^2}\left[1 - \cos\left(\frac{iz}{l(\mathbf{k}, x)}\right)\right],$$

with the following shorthands:

$$l(\mathbf{k}, x) = \frac{2Ex(1 - x)}{\mathbf{k}^2 + \epsilon^2}, \quad (14)$$

$$q_0 = q_{\max}(E), \quad q_1 = q_{\max}(Ex), \quad q_2 = q_{\max}(E(1 - x)), \quad q_3 = \min(q_1, q_2), \quad (15)$$

$\Theta(\mathbf{k}) = \sqrt{\alpha_s(k)}\,\theta(k_{\max} - k)$, $\epsilon^2 = m_q^2 x^2 + m_g^2(1 - x)$, $m_{q,g}$ are the thermal quark and gluon quasiparticle masses, $C_{T,F,A}$ are the color Casimir factors of the color center, quark, and gluon, respectively. Equations (15) correspond to the above described scheme when each scattered parton has its own q-cutoff factor. Note that, in the soft gluon limit $x \ll 1$, our formulas do not reduce to that of [6]. If one uses for the final partons the same $q_{\max}$ as for the initial quark as was done in [6], the second term on the right-hand side of (10) vanishes. This term emerges inevitably because the initial and final partons have different phase space for their scattering. Below, for comparison with [6], we also present the results for $q_i = q_{\max}$ as in [6].

The quantity $L_f = l(\mathbf{k} = 0, x)$ characterizes the longitudinal scale of gluon emission, i.e., the gluon formation length. The induced spectrum depends crucially on the ratio L_f/L [3, 4, 17]. For gluons with small formation length $L_f \ll L$, the finite-size effects caused by the oscillating cosine on the right-hand side of (12), (13) becomes small. In this regime, the rapidly oscillating cosine can be neglected, and the effective cross section (10) becomes equal to the ordinary Bethe–Heitler one, i.e., to the cross section for a quark which approaches the color center from outside. In contrast, when $L_f \gtrsim L$, the finite size effects due to the cosine in (12), (13) suppress greatly the radiation rate as compared to the

Bethe–Heitler one [4, 17]. This suppression, physically, is connected with small transverse size of the qg system (it is $\propto L$). In this regime, the t-channel gluons cannot distinguish the $|q\rangle$ and $|qg\rangle$ Fock components of the physical quark and, for this reason, the gluon emission turns out to be suppressed. One remark regarding the Bethe–Heitler regime for $L_f \ll L$ is in order here. Diagrammatically, the ordinary Bethe–Heitler cross section is given by the diagrams (b), (c), (d) of Fig. 1 involving only one-gluon exchange. However, our formulas include the interference between the diagram (a) and (e), (f), (g), (h). The explanation of this fact is as follows. For a quark incident on the color center from outside, the amplitudes (b), (c), (d) should be evaluated integrating over z' in (4) from $-\infty$ (with usual adiabatic switching off of the coupling constant for $|z'| \longrightarrow \infty$). For a quark produced in a hard reaction at $z' = 0$, the z'-integration region is $(0, \infty)$. This gives rise to additional endpoint terms (corresponding to $z' = 0$) in the cross section which are absent when the lower limit equals $-\infty$. However, similar endpoint terms emerge for the interference term involving the double-gluon exchange diagrams as well. They cancel exactly the endpoint terms stemming from the graph (b), (c), (d). As a result, for $z \longrightarrow \infty$, our effective cross section (10) equals the ordinary Bethe–Heitler one.

It should be noted that our method (and any other one based on the GW model [1] for the QGP) can only give an estimate for the kinematic correction. It is inapplicable in the regime of strong kinematic suppression when the spectrum becomes very sensitive to the detailed form of the kinematic cutoffs. This fact is closely connected with the antileading log character of the **q**, **k**-integrations in (11). Contrary to the ordinary leading log situation, say, in $\gamma^* \longrightarrow q\bar{q}$ transition in deep inelastic scattering, where the typical values of the momentum transfer q is smaller than the internal momentum k, in the case of the induced gluon emission in the high-energy limit when $L_f \gg L$, the dominating contribution to the induced spectrum comes from $q \gtrsim k$. A detailed discussion of this phenomenon is given in [17].

The effective Bethe–Heitler cross section evaluated without kinematic cutoffs, i.e., with $q_i = k_{\max} = \infty$, is given by the first term on the right-hand side of (10). After the Fourier transform, it can be represented in the impact parameter space in the form obtained previously [17, 18] within the LCPI formalism

$$\frac{d\sigma^{BH}(x,z)}{dx} = \mathrm{Re}\int d\boldsymbol{\rho}\boldsymbol{\Psi}^*(\boldsymbol{\rho},x)\sigma_3(\rho,x)\boldsymbol{\Psi}_m(\boldsymbol{\rho},x,z), \tag{16}$$

where $\boldsymbol{\Psi}(\boldsymbol{\rho}, x)$ is the ordinary light-cone wave function for the $q \longrightarrow gq$ transition in vacuum, $\boldsymbol{\Psi}_m(\boldsymbol{\rho}, x, z)$ is the z-dependent light-cone wave function describing the quark–gluon Fock component at the longitudinal coordinate z, and $\sigma_3(\rho, x)$ is the three-body cross section of a $q\bar{q}g$ system with a particle in the medium (the explicit form of the wave functions and three-body cross section can be found in [17]). In the $q\bar{q}g$ system, antiquark is located (in the transverse space) in the center of mass of the qg pair, and the relative separations satisfies the relation $(\boldsymbol{\rho}_g - \boldsymbol{\rho}_{\bar{q}})x = (1-x)(\boldsymbol{\rho}_{\bar{q}} - \boldsymbol{\rho}_q)$.

3. We have performed numerical calculations for fixed and running coupling constant. In the first case, we take $\alpha_s = 0.5$ [19]. For running coupling constant, we use the one-loop formula with $\Lambda_{QCD} = 0.3$ GeV frozen at the value $\alpha_s = 0.65$. In this case, α_s approximately satisfies the relation

$$\int_0^{2\ \mathrm{GeV}} dk\frac{\alpha_s(k)}{\pi} \approx 0.36\ \mathrm{GeV} \tag{17}$$

obtained from the analysis of the heavy-quark energy loss [20]. We have carried out the calculations for expanding plasma. We use the Bjorken [21] model with $T\tau^3 = T_0\tau_0^3$ and take the initial conditions suggested in [22] for heavy-ion central collisions at RHIC: $T_0 = 446$ MeV and $\tau_0 = 0.147$ fm. For the upper limit of the z-integration in (1), we take $L = R_A \approx 6$ fm. For quark and gluon quasiparticle masses, we use the values obtained in [16] from the lattice data $m_q \approx 0.3$ and $m_g \approx 0.4$ GeV. With the above value of m_g from the perturbative relation $\mu_D = \sqrt{2}\,m_g$, one obtains for the Debye screening mass $\mu_D \approx 0.57$ GeV. For the energy dependence of the maximum momentum transfer, we take $q^2_{\max}(E) \approx E\bar{E}_{\mathrm{th}}$ with $\bar{E}_{\mathrm{th}} = 750$ MeV. It is smaller than $q^2_{\max}(E) \approx 3E\mu_D$ used in [6].

In Figs. 2 and 3, we plot the induced gluon spectrum for $E = 5$, 10, and 20 GeV evaluated using (1), (10)–(15) with (solid line) and without (dashed line) the kinematic cutoffs for fixed and running α_s. The results with kinematic cutoffs have been obtained for q_i given in (15). For this version, we also plot the spectrum without the second term in (10) (dotted line). In Figs. 2 and 3, we also show the results for the same kinematic cutoffs for initial and final partons obtained with $q_i = q_{\max}(E)$ (long-dashed line). From Figs. 2 and 3, one sees that the kinematic cutoffs become especially important when the energy of the radiated gluon (or the final quark) $\lesssim$1–2 GeV. The kinematic correction is smaller for running coupling constant. It is also seen that, for fixed coupling constant, the relative contribution from the second term in (10) is larger. It is natural since, for the running α_s, the contribution from large transverse momenta is suppressed. The total spectrum in the above two scheme of the q-cutoff turns out to be approximately the same.

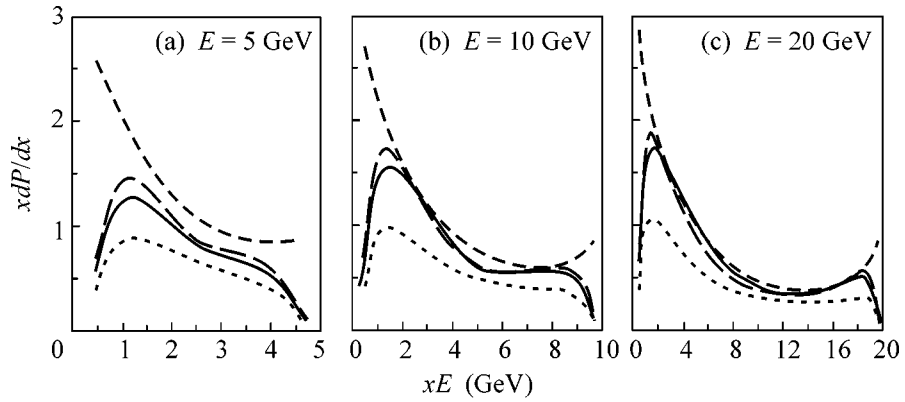

Fig. 2. The spectrum of the induced $q \longrightarrow gq$ transition versus the gluon energy xE for RHIC conditions for fixed coupling constant. The solid lines are for q_i given in (15), and the long-dashed lines are for the same q-cutoffs for the initial and final partons with $q_i = q_{\max}(E)$. The dashed lines show the spectrum obtained without kinematics cutoffs. The spectrum without the second term in (10) for q_i given in (15) is shown by the dotted curves.

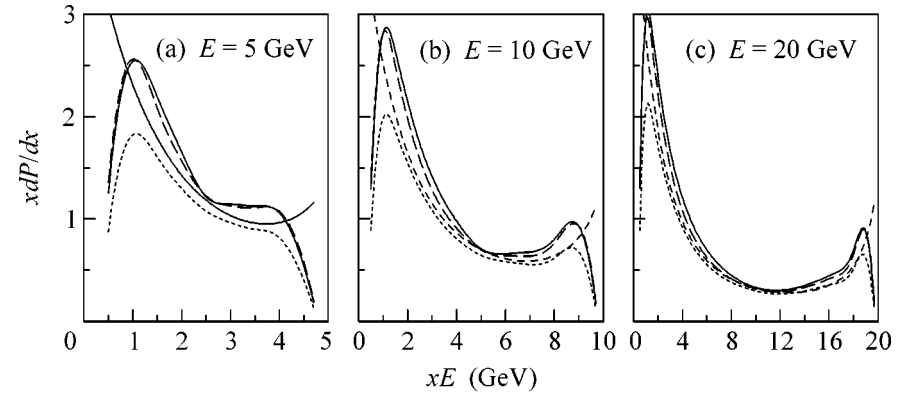

Fig. 3. The same as in Fig. 2 but for running coupling constant.

To illustrate the effect of the kinematic cutoffs on the quark energy loss in Fig. 4, we plot the energy dependence of the kinematic K-factor

$$K(E) = \frac{\Delta E_{f.b.}}{\Delta E_{i.b.}}, \tag{18}$$

where $\Delta E_{f.b.}$ and $\Delta E_{i.b.}$ are the quark energy losses evaluated with (for q_i as given in (15)) and without kinematic constraints, respectively. We define ΔE as

$$\Delta E = E\int_{x_{\min}}^{x_{\max}} dx x\frac{dP}{dx} \tag{19}$$

with $x_{\min} = m_g/E$, $x_{\max} = 1 - m_q/E$. Figure 4 demonstrates that, for fixed coupling constant, the kinematic cutoffs are important for $E \lesssim 20$ GeV. For running coupling, the kinematic correction is small even for $E \sim 5$ GeV. One can see that the difference between the cutoffs

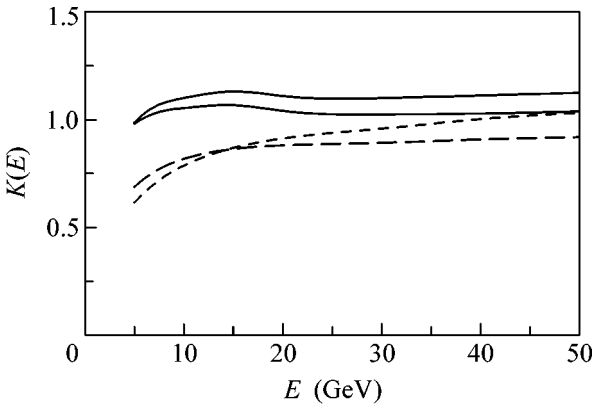

Fig. 4. The energy dependence of the kinematic K-factor (18) for RHIC conditions for running (solid line) and fixed (dashed line) coupling constant. The thick lines are for the q-cutoff given in (15), and the thin lines are for $q_i = q_{\max}(E)$.

given in (15) (thick curves) and $q_i = q_{\max}(E)$ (thin curves) is less than ~10%.

The kinematic K-factor shown in Fig. 4 is obtained for an expanding plasma with $n(z) \propto 1/z$. For comparison with the analysis [6], we have also carried out calculations for a homogeneous plasma. In this case, the kinematic effect is weaker since the relative contribution of the region of small z, where the typical parton transverse momenta are large (they are $\propto 1/\sqrt{z}$) is smaller. For correspondence with [6], we have taken $q^2_{\max} = 3E\mu_D$ (the same for the initial and final partons) and $k^2_{\max} = 4E^2\min(x^2, x(1-x))$ used in [6] which give somewhat smaller kinematic effect than our cutoffs. We have obtained a small kinematic effect, say, $K \approx 0.9$ at $E = 5$ GeV and $K \approx 0.94$ at $E = 10$ GeV (we have used fixed coupling constant as in [6]). It is considerably larger than the suppression reported in [6] (~1/6 for $E =$ 5 GeV). In connection with strong kinematic suppression reported in [6], we would like to emphasize one more time that, within the approximation of static color centers [1] when the kinematic cutoffs are introduced by hand, the regime of strong kinematic effect cannot be described accurately. It is clear that the analysis of the induced radiation in this regime requires an accurate treatment of the recoil effects. In this case, the fast partons moving through QGP and partons from QGP should be treated on an even footing. Note also that, in this regime, suppression of the radiative energy loss may largely be compensated by the collisional energy loss due to strong recoil effects.

In summary, the form of the induced gluon spectrum obtained in the present analysis shows that the kinematic effect is relatively small and is mainly important near to the endpoints $x \sim 0$ and $x \sim 1$ when the energy of the radiated gluon (or of the final quark) is about ~2–3 units of the Debye screening mass, i.e., about 1–2 GeV for RHIC and LHC conditions. For fixed coupling constant, the kinematic correction to the quark energy loss becomes small for $E \gtrsim 20$ GeV; for running coupling constant, it is small even at $E \sim 5$ GeV. The kinematic effect found in our analyses is considerably smaller than reported in [6]. Our results say that, in the region of the gluon fractional momentum $\delta \lesssim x \lesssim 1 - \delta(\delta \sim (2–3)\mu_D/E)$, the induced spectrum can be evaluated to reasonable accuracy within the LCPI approach [3] which ignores the kinematic bounds. This approach can be used for evaluation of the energy loss and nuclear suppression factor [19] for RHIC and LHC energies.

I thank N.N. Nikolaev for discussion of the results. I am grateful to the High Energy Group of the ICTP for the kind hospitality during my visit to Trieste where the present calculations were carried out.

REFERENCES

1. M. Gyulassy and X.-N. Wang, Nucl. Phys. B **420**, 583 (1994); X.-N. Wang, M. Gyulassy, and M. Plumer, Phys. Rev. D **51**, 3436 (1995).
2. R. Baier, Y. L. Dokshitzer, A. H. Mueller, *et al.*, Nucl. Phys. B **483**, 291 (1997); **484**, 265 (1997).
3. B. G. Zakharov, JETP Lett. **63**, 952 (1996).
4. B. G. Zakharov, JETP Lett. **65**, 615 (1997).
5. R. Baier, Y. L. Dokshitzer, A. H. Mueller, and D. Schiff, Nucl. Phys. B **531**, 403 (1998).
6. M. Gyulassy, P. Lévai, and I. Vitev, Nucl. Phys. B **594**, 371 (2001).
7. U. A. Wiedemann, Nucl. Phys. A **690**, 731 (2001).
8. G. David *et al.* (PHENIX Collab.), Nucl. Phys. A **698**, 227 (2002); D. d'Enterria *et al.* (PHENIX Collab.), Nucl. Phys. A **715**, 749 (2003).
9. J. C. Danlop *et al.* (STAR Collab.), Nucl. Phys. A **698**, 515 (2002); J. C. Klay *et al.* (STAR Collab.), Nucl. Phys. A **715**, 733 (2003).
10. M. Gyulassy, P. Lévai, and I. Vitev, Phys. Lett. B **538**, 282 (2002).
11. B. G. Zakharov, Phys. At. Nucl. **61**, 838 (1998).
12. B. G. Zakharov, JETP Lett. **70**, 176 (1999).
13. R. Baier, D. Schiff, and B. G. Zakharov, Annu. Rev. Nucl. Part. Sci. **50**, 37 (2000).
14. L. D. Landau and I. Ya. Pomeranchuk, Dokl. Akad. Nauk SSSR **92**, 535 (1953); Dokl. Akad. Nauk SSSR **92**, 735 (1953).
15. A. B. Migdal, Phys. Rev. **103**, 1811 (1956).
16. P. Lévai and U. Heinz, Phys. Rev. C **57**, 1879 (1998).
17. B. G. Zakharov, JETP Lett. **73**, 49 (2001).
18. B. G. Zakharov, in *Proceedings of the 33rd Rencontres de Moriond: QCD and High Energy Hadronic Interactions*, Ed. by J. Tran Thanh Van (Les Arcs, France, 1998), p. 533; hep-ph/9807396.
19. R. Baier, Yu. L. Dokshitzer, A. H. Mueller, and D. Schiff, J. High Energy Phys. **0109**, 033 (2001); hep-ph/0106347 (2001).
20. Yu. L. Dokshitzer, V. A. Khoze, and S. I. Troyan, Phys. Rev. D **53**, 89 (1996).
21. J. D. Bjorken, Phys. Rev. D **27**, 140 (1983).
22. R. J. Fries, B. Müller, and D. K. Srivastava, nucl-th/0208001 (2003).

JETP Letters, Vol. 80, No. 2, 2004, pp. 73–77. From Pis'ma v Zhurnal Éksperimental'noĭ i Teoreticheskoĭ Fiziki, Vol. 80, No. 2, 2004, pp. 81–85.

Vector Meson Couplings to Vector and Tensor Currents in Extended NJL Quark Model¶

M. Chizhov

Institut de Physique Nucléaire de Lyon and Université Claude Bernard Lyon-1, 69622 Villeurbanne, France
Center for Space Research and Technologies, Faculty of Physics, University of Sofia, 1164 Sofia, Bulgaria

Received May 14, 2004

A simple explanation of the dynamic properties of vector mesons is given in the framework of extended Nambu–Jona-Lasinio quark model. New mass relations among the hadron vector resonances are derived. The results of this approach are in good accordance with the QCD sum rules, the lattice calculations, and the experimental data. © *2004 MAIK "Nauka/Interperiodica".*

PACS numbers: 12.39.Ki; 12.39.Fe; 14.40.Cs

1. INTRODUCTION

All known elementary vector particles, the photon, *Z*, *W*, and gluons, are gauge particles. An opinion exists that there are no other vector particles besides gauge ones. They have only chirality-conserved vector interactions with matter fields. The so-called *anomalous* term, which appears from radiative corrections [1], is small and is not present in the initial Lagrangian. It describes chirality-flipped interactions with the tensor current.

Although gluons are gauge particles, they induce chirality violation, and, therefore, in hadron physics, the *anomalous* interactions of the vector mesons are not so small. They should be taken into account, for example, to extract the $|V_{ub}|$ element of the CKM matrix from the semileptonic decay $B \longrightarrow \rho l\nu$. Even more peculiar is the existence of the vector $b_1(1235)$ meson with only anomalous interactions with quarks. It is not possible at all to describe this meson as a gauge particle.

This type of particle originates from a tensor formalism. It is known that free relativistic particles with spin 1 can be described by the four-vector A_μ or by the second-rank antisymmetric tensor field $T_{\mu\nu}$. These two different descriptions are applied to the vector mesons without noting the main difference between them [2]. However, the different formalisms are related to the different couplings of the vector mesons to the quarks and, therefore, to the different chiral properties. The vector fields are transformed under *real* (chirally neutral) representation (1/2, 1/2) of the Lorentz group. On the other hand, $T_{\mu\nu} \pm i\tilde{T}_{\mu\nu}$ combinations are transformed under irreducible *chiral* representations (1, 0) and (0, 1). They describe *chiral* vector fields.

The aim of this letter is to put on the same footing (at least at a phenomenological level) the consideration of the gauge particles and the particles with only *anomalous* interactions. The successful description of the dynamical properties of the hadron systems hints that the same phenomenon also takes place in high-energy physics. Then, we may expect the discovery of *anomalously* interacting particles at future colliders.

The Nambu–Jona-Lasinio (NJL) [3] quark model is a successful tool for investigating hadron physics and the spontaneous chiral-symmetry-breaking mechanism. However, an extension of the model is needed [4] in order to introduce the new type *anomalous* interactions and the particles associated with them.

To simplify the idea, we will deal only with the one-flavor NJL model. The generalization for the real case with *N* flavors is straightforward and will be considered elsewhere. As long as the isospin triplet $I = 1$ consists of *up* and *down* quarks with approximately the same constituent masses, we can apply this one-flavor model to the vector mesons ρ, b_1, a_1, and ρ'. Using this approach, we will get, for example, very a simple prediction for the ratio $f_\rho^T/f_\rho \simeq 1/\sqrt{2}$, which matches the latest lattice calculations [5] very well.

2. THE MODEL

Following the classical paper [3], we start with the chiral invariant Lagrangian

$$\mathcal{L} = \bar{\psi}\partial\!\!\!/\psi + \frac{G_0}{2}\bar{\psi}(1+\gamma^5)\psi\bar{\psi}(1-\gamma^5)\psi$$
$$-\frac{G_V}{2}(\bar{\psi}\gamma_\mu\psi)^2 - \frac{G_A}{2}(\bar{\psi}\gamma_\mu\gamma^5\psi)^2 \qquad (1)$$
$$-\frac{G_T}{2}\bar{\psi}\sigma_{\mu\lambda}(1+\gamma^5)\psi\frac{q_\mu q_\nu}{q^2}\bar{\psi}\sigma_{\nu\lambda}(1-\gamma^5)\psi,$$

¶ This article was submitted by the author in English.

0021-3640/04/8002-0073$26.00 © 2004 MAIK "Nauka/Interperiodica"

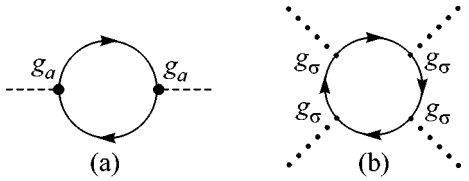

Fig. 1. Radiative corrections to (a) meson self-energy and (b) scalar self-interaction.

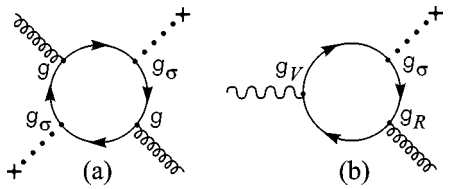

Fig. 2. (a) Contributions to the mass term and (b) mixing between vector mesons.

where the new tensor interaction term was introduced. It should contain a unique momentum dependence, because the local product of two tensor currents with different chiralities vanishes identically. Generally speaking, there are four different positive coupling parameters, G_0, G_V, G_A, and G_T, with dimensions $[mass]^{-2}$ for each chiral invariant term.

Let us rewrite Lagrangian (1) by introducing auxiliary bosonic fields (without kinetic terms), which will later play the role of collective meson states after quantization

$$\begin{aligned}\mathcal{L} &= \bar{\psi}\partial\!\!\!/\psi + g_\sigma\bar{\psi}\psi\sigma - \frac{g_\sigma^2}{2G_0}\sigma^2 + ig_\pi\bar{\psi}\gamma^5\psi\pi - \frac{g_\pi^2}{2G_0}\pi^2 \\ &+ g_V\bar{\psi}\gamma_\mu\psi V_\mu + \frac{g_V^2}{2G_V}V_\mu^2 + g_A\bar{\psi}\gamma_\mu\gamma^5\psi A_\mu + \frac{g_A^2}{2G_A}A_\mu^2 \\ &- ig_R\bar{\psi}\sigma_{\mu\nu}\psi\frac{q_\mu}{|q|}R_\nu + \frac{g_R^2}{2G_T}R_\mu^2 \\ &+ g_B\bar{\psi}\sigma_{\mu\nu}\gamma^5\psi\frac{q_\mu}{|q|}B_\nu + \frac{g_B^2}{2G_T}B_\mu^2,\end{aligned} \tag{2}$$

where g_a ($a = \sigma, \pi, V, A, R, B$) are dimensionless coupling constants. At the classical level, Lagrangians (1) and (2) are equivalent. However, the perturbation quantum field theory cannot be applied in the former case due to the dimensional constants G. Therefore, the second form of the Lagrangian with dimensionless coupling constants g_a is more appropriate for quantization by perturbative methods [6].

3. QUANTUM CORRECTIONS AND SYMMETRY BREAKING

It is interesting to note that, in spite of the absence of kinetic terms for the meson fields in initial Lagrangian (2), they are generated at the quantization stage due to radiative corrections (Fig. 1a). Such kinetic term generation reflects into relations of the coupling constants g_a. In a one-loop approximation, they are

$$3g_\sigma^2 = 3g_\pi^2 = 2g_V^2 = 2g_A^2 = g_R^2 = g_B^2 = \frac{24\pi^2}{N_c}\varepsilon, \tag{3}$$

where N_c is the number of colors and ε is the dimensional regularization parameter. The quark loops lead also to various self-interactions and interactions among the mesons. For example, due to generation of quartic self-interaction σ^4 of the scalar meson (Fig. 1b), a spontaneous breaking of the chiral symmetry occurs, which leads to generation of nonzero quark mass $m = -\langle\sigma\rangle/g_\sigma$, to additional mass contributions for the mesons (Fig. 2a), and to mixings between them (Fig. 2b).

The chiral symmetry breaking for the scalar sector has been studied in detail. The introduction of the new vector mesons R_μ and B_μ brings nothing new there. On the other hand, the symmetry breaking leads to an interesting phenomenon in the vector-mesons sector. In the following, we focus just on the vector mesons.

We have introduced four vector mesons, V_μ, A_μ, R_μ, and B_μ. Their quantum numbers (the total angular momentum J, P parity, and the charge conjugation C) can be defined from their interactions with quarks (2):

Meson vector fields	V_μ	A_μ	R_μ	B_μ
Quantum numbers J^{PC}	1^{--}	1^{++}	1^{--}	1^{+-}

The vector mesons V_μ and A_μ have gaugelike minimal interactions with quarks, while R_μ and B_μ have only *anomalous* tensor interactions. Nevertheless, in the chiral limit, all these mesons couple to *conserved* quark currents. Therefore, their kinetic terms are gauge-invariant:

$$\begin{aligned}\mathcal{L}_0 &= -\frac{1}{2}V_\mu(q^2g_{\mu\nu} - q_\mu q_\nu)V_\nu + \frac{M_V^2}{2}V_\mu^2 \\ &- \frac{\sqrt{18}m}{|q|}V_\mu(q^2g_{\mu\nu} - q_\mu q_\nu)R_\nu \\ &- \frac{1}{2}R_\mu(q^2g_{\mu\nu} - q_\mu q_\nu)R_\nu + \frac{M_T^2 - 6m^2}{2}R_\mu^2 \\ &- \frac{1}{2}B_\mu(q^2g_{\mu\nu} - q_\mu q_\nu)B_\nu + \frac{M_T^2 + 6m^2}{2}B_\mu^2 \\ &- \frac{1}{2}A_\mu(q^2g_{\mu\nu} - q_\mu q_\nu)A_\nu + \frac{M_A^2 + 6m^2}{2}A_\mu^2.\end{aligned} \tag{4}$$

Here, $M_V^2 = g_V^2/G_V$, $M_A^2 = g_A^2/G_A$, and $M_T^2 = g_R^2/G_T = g_B^2/G_T$ are the initial vector boson masses before symmetry breaking. Since R_μ and B_μ are chiral mesons, their masses, $M_R^2 = M_T^2 - 6m^2$ and $M_B^2 = M_T^2 + 6m^2$, split due to symmetry breaking. The axial-vector mesons A_μ also get an additional contribution to their mass terms.

The essential feature of Eq. (4) is the mixing between the two vector mesons V_μ and R_μ, which have the same quantum numbers as ρ and ρ' mesons. In the Lorentz gauge, this reads

$$\mathcal{L}_{VR} = -\frac{1}{2}(V_\mu R_\mu)\begin{pmatrix} q^2 - M_V^2 & \sqrt{18}m|q| \\ \sqrt{18}m|q| & q^2 - M_R^2 \end{pmatrix}\begin{pmatrix} V_\mu \\ R_\mu \end{pmatrix}. \quad (5)$$

If we identify the physical states with quantum numbers 1^{--} with these mesons, they can be expressed as linear combinations of the chiral eigenstates V_μ and R_μ:

$$\begin{aligned} \rho_\mu(q^2) &= \cos\theta(q^2)V_\mu + \sin\theta(q^2)R_\mu, \\ \rho'_\mu(q^2) &= -\sin\theta(q^2)V_\mu + \cos\theta(q^2)R_\mu, \end{aligned} \quad (6)$$

where

$$\tan 2\theta(q^2) = \frac{\sqrt{72m^2q^2}}{M_R^2 - M_V^2}. \quad (7)$$

It means that ρ and ρ' mesons have both vector and anomalous tensor couplings with quarks, while the axial-vector mesons a_1 with quantum numbers 1^{++}, which are assigned to A_μ, have only gaugelike minimal interactions and the axial-vector mesons b_1 with quantum numbers 1^{+-}, which are assigned to B_μ, have only anomalous tensor interactions.

Diagonalization of (5) leads to relations for the physical masses of ρ, ρ', and b_1 mesons [7], $m_\rho = 771.1 \pm 0.9$ MeV, $m_{\rho'} = 1465 \pm 25$ MeV, and $m_{b_1} = 1229.5 \pm 3.2$ MeV:

$$\begin{aligned} m_\rho^2 + m_{\rho'}^2 &= M_V^2 + m_{b_1}^2 + 6m^2, \\ m_\rho^2 m_{\rho'}^2 &= M_V^2(m_{b_1}^2 - 12m^2), \end{aligned} \quad (8)$$

which define $M_V = 1034 \pm 33$ MeV and the quark mass $m = 163 \pm 7$ MeV.

In general, the mixing angle θ depends on q^2 (7) and should be different at ρ and ρ' scale. However, the denominator in (7) is smaller in comparison with the nominator and $2\theta(q^2) = |q|/(89^{+82}_{-75}$ MeV) is big, which corresponds to almost maximal mixing $\theta \sim \pi/4$ with weak q^2 dependence.

If we suppose that the effective four-fermion interactions of quarks (1) could originate in QCD by gluon exchange in $1/N_c$ limit, it follows that $M_V = M_A$ [8]. Then, from the first equation in (8), a remarkable relation among masses of the vector mesons is obtained:

$$m_\rho^2 + m_{\rho'}^2 = m_{a_1}^2 + m_{b_1}^2. \quad (9)$$

This leads to a little bit smaller value for the mass of a_1 meson, $m_{a_1} = 1109 \pm 37$ MeV (2.2σ below PDG estimation).

4. LONGITUDINAL AND TRANSVERSE POLARIZATIONS OF THE VECTOR MESONS

The longitudinal and transverse polarizations of the (axial-)vector mesons are defined by the corresponding couplings f from the matrix elements

$$\begin{aligned} \langle 0|\bar\psi\gamma_\mu\gamma^5\psi|A(q,\lambda)\rangle &= m_A f_A e_\mu^\lambda, \\ \langle 0|\bar\psi\sigma_{\mu\nu}\psi|A(q,\lambda)\rangle &= i f_A^T \varepsilon_{\mu\nu\alpha\beta} e_\alpha^\lambda q_\beta; \end{aligned} \quad (10)$$

$$\begin{aligned} \langle 0|\bar\psi\gamma_\mu\psi|V(q,\lambda)\rangle &= m_V f_V e_\mu^\lambda, \\ \langle 0|\bar\psi\sigma_{\mu\nu}\psi|V(q,\lambda)\rangle &= i f_V^T(e_\mu^\lambda q_\nu - e_\nu^\lambda q_\mu), \end{aligned} \quad (11)$$

where e_μ^λ is the polarization vector of a spin-1 meson. Then, using meson–fermion couplings (2) and taking into account the mixing after symmetry breaking (6), we can express the couplings f in terms of the parameters of our model:

$$f_{a_1} = m_{a_1}/g_A, \quad f_{a_1}^T = 0; \quad (12)$$

$$f_{b_1} = 0, \quad f_{b_1}^T = m_{b_1}/g_B; \quad (13)$$

$$\begin{aligned} f_\rho &= \frac{m_\rho\cos\theta(m_\rho) + \sqrt{18}m\sin\theta(m_\rho)}{g_V}, \\ f_\rho^T &= \frac{m_\rho\sin\theta(m_\rho) + \sqrt{18}m\cos\theta(m_\rho)}{g_R}; \end{aligned} \quad (14)$$

$$\begin{aligned} f_{\rho'} &= \frac{-m_{\rho'}\sin\theta(m_{\rho'}) + \sqrt{18}m\cos\theta(m_{\rho'})}{g_V}, \\ f_{\rho'}^T &= \frac{m_{\rho'}\cos\theta(m_{\rho'}) - \sqrt{18}m\sin\theta(m_{\rho'})}{g_R}; \end{aligned} \quad (15)$$

where g_a obey relations (3).

We can immediately make simple qualitative predictions, using the interesting fact that the solution of system (8) is very close to the unique solution when the mixing angle θ equals π/4 and does not depend on q^2. This happens when $M_R^2 = M_V^2$. In this case, some valuable mass relations, besides (9), have place

$$m_{\rho'} = m_\rho + \sqrt{18}m,$$

$$3m_{b_1}^2 = 2m_{\rho'}^2 - m_\rho m_{\rho'} + 2m_\rho^2, \quad (16)$$

$$3m_{a_1}^2 = m_{\rho'}^2 + m_\rho m_{\rho'} + m_\rho^2.$$

The first two relations are based only on the suggestion of maximal mixing, while the last one requires the additional constraint $M_V = M_A$. Using more precise mass values for ρ and b_1 mesons [7], we can predict other masses based solely on this ansatz: $m_{a_1} = 1155.1 \pm 2.7$ MeV, $m_{\rho'} = 1500.5 \pm 4.8$ MeV, and $m = 171.9 \pm 1.3$ MeV.

It is interesting to note that the second relation can be applied to the spin-1 isosinglets $I = 0$ ω(782), ω'(1420), $h_1(1170)$ and φ(1020), φ'(1680), $h_1(1380)$, which are almost pure $(u\bar{u} + d\bar{d})/\sqrt{2}$ and $s\bar{s}$ states, respectively. In the first case, the mass relation among ω's and h_1 is fairly satisfied. In the second case, we can confirm the existence of the $h_1(1380)$ state, which is omitted from the summary table. Our prediction for the mass $m_{h_1(1380)} = 1415 \pm 13$ MeV agrees with PDG average $m_{h_1(1380)} = 1386 \pm 19$ MeV.

In the case of the maximal mixing, Eqs. (14) and (15) can be rewritten in a compact form:

$$f_\rho = \frac{m_{\rho'}}{\sqrt{2}g_V}, \quad f_\rho^T = \frac{m_{\rho'}}{\sqrt{2}g_R}; \quad (17)$$

$$f_{\rho'} = -\frac{m_\rho}{\sqrt{2}g_V}, \quad f_{\rho'}^T = \frac{m_\rho}{\sqrt{2}g_R}. \quad (18)$$

As far as $g_R = \sqrt{2}\,g_V$, Eq. (17) leads directly to a prediction for the ratio $f_\rho^T/f_\rho = 1/\sqrt{2} \approx 0.707$, which is in perfect agreement with the latest lattice calculations [5]. The corresponding ratio for the ρ' meson should have the same value and the opposite sign $f_{\rho'}^T/f_{\rho'} = -1/\sqrt{2}$. Unfortunately, there are no lattice calculations for the ρ' meson yet.

Another reliable method giving information about the matrix elements is the QCD sum rules [9]. If one accepts the experimental value for the vector coupling $f_\rho = 208 \pm 10$ MeV [5], the QCD sum rules give compatible with lattice calculation result $f_\rho^T = 160 \pm 10$ MeV [10]. It is interesting to note that the consideration of the correlation function of the tensor with the vector current proves that the relative sign of f_ρ^T and f_ρ is positive [11]. Moreover, it was shown [12] that the contribution of the ρ' meson to this correlation function is negative and $m_\rho f_\rho f_\rho^T \simeq -2m_{\rho'} f_{\rho'} f_{\rho'}^T$. This is in good accordance with our predictions (17) and (18), since $m_{\rho'} \simeq 2m_\rho$.

The derivation of the transverse couplings within the QCD sum rules framework has been reestimated in [13]: $f_\rho^T = 157 \pm 5$ MeV and $f_{b_1}^T = 184 \pm 5$ MeV, confirming the results of [10]. In addition, the ρ'-transverse coupling $f_{\rho'}^T = 140 \pm 5$ MeV has been evaluated, which is, however, in contradiction with the superconvergence relation

$$(f_\rho^T)^2 + (f_{\rho'}^T)^2 = (f_{b_1}^T)^2 \quad (19)$$

from [14].

It should be compared with our predictions for the same couplings: $f_\rho^T = (0.703^{+0.004}_{-0.007})f_\rho = 146 \pm 7$ MeV, $f_{b_1}^T = (0.839^{+0.017}_{-0.015})f_\rho = 175 \pm 9$ MeV, and $f_{\rho'}^T = (0.405^{+0.040}_{-0.034})f_\rho = 84 \pm 9$ MeV. The first two are in good agreement with all QCD sum rules results, while the last one for the ρ' meson is in a good accordance with relation (19), but it is in noticeable disagreement with [13].

It is worth noting that the anomalous dimension of the tensor current is not zero and the couplings $f^T(\mu)$ are scale-dependent. Our values are systematically lower than QCD estimations made at the renormalization scale $\mu = 1$ GeV and closer to lattice calculations at $\mu = 2$ GeV.

5. CONCLUSIONS

In this letter, we followed an approach based on the extended NJL quark model, describing all low-lying meson resonances. In total, there are 16 degrees of freedom for the one-flavor quark–antiquark meson excitations: scalar, pseudoscalar, vector, axial-vector, and antisymmetric tensor. They have corresponding Yukawa interactions with quarks. All these excitations are assigned to physical meson states σ, π, ρ, a_1, ρ', and b_1. The (pseudo)scalar sector was already well studied, and the introduction of the tensor bosons does not bring anything new there. Hence, we have concentrated mainly on the spin-1 meson sector.

Simultaneous description of all these states in the framework of the NJL model leads to interesting predictions like new mass formulas and relations among meson coupling constants. All these relations are in agreement with present experimental data and the numerical calculations on the lattice and the QCD sum rules.

Another interesting property which follows immediately from our approach is the dual nature of ρ and ρ' mesons. They have both vector and tensor couplings with quarks. The new insight into this phenomenon is the suggestion that there exist two different vector particles with the same quantum numbers, which interact differently with quarks. One of them has only gaugelike vector interactions, and the other one has only *anoma-*

lous tensor interactions. After the spontaneous chiral symmetry breaking, they are mixed, producing the physical ρ and ρ' meson states. From the point of view of hadron phenomenology, this suggestion does not seem unnatural, because the axial-vector mesons a_1 and b_1, due to their different quantum numbers, exist as pure states, which have correspondingly only gaugelike couplings and tensor couplings with quarks.

The above consideration means that, in nature, there exist two different vector particles with respect to their interactions with matter. However, they are just composite quark–antiquark states. The question of whether there are new fundamental vector particles will be probably answered at the future colliders and, especially, at LHC.

I would like to thank Prof. V. Braun for useful comments. During preparation of this letter, I learned of the premature death of Prof. I. Kogan. We all miss him very much. I acknowledge the warm hospitality of IPNL and, especially, Profs. S. Katsanevas and Y. Déclais.

REFERENCES

1. J. Schwinger, Phys. Rev. **73**, 416 (1948).
2. G. Ecker *et al.*, Nucl. Phys. B **321**, 311 (1989).
3. Y. Nambu and G. Jona-Lasinio, Phys. Rev. **122**, 345 (1961).
4. M. V. Chizhov, hep-ph/9610220.
5. D. Becirevic *et al.*, J. High Energy Phys. **05**, 007 (2003); V. M. Braun *et al.*, Phys. Rev. D **68**, 054501 (2003).
6. T. Eguchi, Phys. Rev. D **14**, 2755 (1976).
7. K. Hagiwara *et al.*, Phys. Rev. D **66**, 010001 (2002).
8. J. Bijnens, Phys. Rep. **265**, 369 (1996).
9. M. A. Shifman, A. I. Vainshtein, and V. I. Zakharov, Nucl. Phys. B **147**, 385 (1979); **147**, 448 (1979).
10. P. Ball and V. M. Braun, Phys. Rev. D **54**, 2182 (1996).
11. V. L. Chernyak and A. R. Zhitnitsky, Phys. Rep. **112**, 173 (1984).
12. V. M. Belyaev and Ya. I. Kogan, Sov. J. Nucl. Phys. **40**, 659 (1984).
13. A. P. Bakulev and S. V. Mikhailov, Eur. Phys. J. C **17**, 129 (2000).
14. N. S. Craigie and J. Stern, Phys. Rev. D **26**, 2430 (1982).

JETP Letters, Vol. 80, No. 2, 2004, pp. 78–82. Translated from Pis'ma v Zhurnal Éksperimental'noĭ i Teoreticheskoĭ Fiziki, Vol. 80, No. 2, 2004, pp. 86–91.

Calorons and the Bilocal Correlator of the Gluon-Field Strength

N. O. Agasian* and S. M. Fedorov**

Institute of Theoretical and Experimental Physics, ul. Bol'shaya Cheremushkinskaya 25, Moscow, 117218 Russia

** e-mail: agasian@heron.itep.ru*

*** e-mail: fedorov@heron.itep.ru*

Received May 27, 2004; in final form, June 10, 2004

The bilocal correlator for finite-temperature gluodynamics is calculated in the instanton gas model. It is shown that the correlation length of vacuum in this model decreases when temperature increases. The results are compared with finite-temperature lattice calculations for the bilocal correlator. The instanton density and possible structures of nonperturbative vacuum are discussed. © *2004 MAIK "Nauka/Interperiodica".*

PACS numbers: 12.38.Lg; 11.15.Tk

Nonperturbative fluctuations of gluon fields are of fundamental importance for the vacuum of non-Abelian gauge theories and determine many properties of QCD. In particular, they are responsible for confinement, spontaneous breaking of chiral symmetry, and, finally, for the formation of the observed hadron spectrum. The instanton-liquid model, which was proposed by Shuryak [1] and Dyakonov and Petrov [2], is well developed and quite successfully explains many QCD phenomena. In this model, instantons and anti-instantons that are well separated and interact with each other not too strongly (this is a reason for the name "liquid") are basic nonperturbative fields. The instanton density is equal to about 1 fm^{-4}. This model makes it possible to solve a number of QCD problems. In particular, spontaneous breaking of chiral symmetry arises naturally in this model, the mass of the η' meson is explained, etc. Nevertheless, it has a number of substantial disadvantages. Namely, it is unknown how to stabilize the instanton–anti-instanton ensemble (problem of the infrared inflation of instantons), and confinement cannot be explained in the instanton-liquid model.

However, vacuum contains not only semiclassical instantons but also other nonperturbative fields that, in particular, enable one to solve the infrared problem of instantons. Nonperturbative QCD vacuum can be parameterized by a set of the nonlocal gauge-invariant vacuum averages of the gluon-field strength [3]. In this case, a large number of phenomena in hadron physics can be described (see review [4]). In many cases, the inclusion of only the bilocal correlator (stochastic-vacuum model) provides the qualitative explanation of effects. Moreover, there are indications that corrections due to higher correlators are small and do not exceed several percent in some cases [4]. In this approach, string tension arises naturally and is expressed in terms of the vacuum average of chromoelectric field strengths [3]:

$$\sigma = \frac{g^2}{2}\int d^2x \langle \mathrm{Tr}(E_i(x)\Phi(x,0)E_i(0)\Phi^\dagger(x,0))\rangle, \quad (1)$$

where $E_i = F_{4i}$ is the chromoelectric field operator, $F_{\mu\nu} = F^a_{\mu\nu}t^a$ is the gluon-field strength tensor, and $\Phi(x, 0)$ is the operator of translation along the straight line connecting points x and 0. Integration in Eq. (1) is performed in spacetime plane $(i, 4)$.

The problem of the infrared inflation of instantons is also naturally solved in the stochastic-vacuum model. Analysis of the effect of nonperturbative quantum fluctuations on instantons was begun in [5, 6]. More recently, it was shown that standard perturbation theory changes in nonperturbative stochastic vacuum, and the contribution of large instantons to physical quantities becomes finite [7]. Further, the direct interaction of an instanton with nonperturbative vacuum fields was proved to stabilize the instanton at a scale of the correlation length in vacuum condensate [8]. The size distribution of instantons, which has a maximum at $\rho_c \simeq 0.25$ fm and coincides well with lattice calculations, was obtained.

An important property of vacuum is scaling revealed in lattice calculations for string tension between sources in the different representations of the color group [9]. As was shown in [10], the contribution of instantons to the potential between heavy quarks in different representations breaks Casimir scaling. Therefore, their density must be limited.

In this work, we analyze the contribution of instantons to the bilocal correlator for finite temperature.[1] We show that the correlation length of the bilocal correlator

[1] The bilocal correlator in the instanton gas for zero temperature was calculated in [11, 12].

on calorons (instantons at finite temperature) in the lowest order in the density of calorons depends rather strongly on temperature. This behavior disagrees with lattice calculations, according to which the correlation length for the bilocal correlator of chromomagnetic fields is independent of temperature over the entire range from zero to T_c within errors [13].

The temperature dependence of the chromomagnetic bilocal correlator was analytically found in [14]. It was shown that chromomagnetic condensate increases slowly with temperature up to $2T_c$, and the correlation length $\lambda_m(T)$ in this temperature range is independent of T. For high temperatures $T > 2T_c$, condensate increases with T as $\langle H^2\rangle_T \propto g^8(T)T^4$ and the magnetic correlation length decreases as $\lambda_m(T) \propto 1/g^2(T)T$. These behaviors completely agree with lattice calculations, where the scaling behaviors of these quantities in the high-temperature region were obtained [15]. There is a simple physical explanation of the independence of the correlation length on temperature at $T \leq T_c$. The inverse magnetic correlation length $M = 1/\lambda_m$ is the mass of the 1^{+-} lowest magnetic gluelump. Gluelumps [16] are nonphysical objects, but they play an important role in nonperturbative QCD, because their masses determine field correlators and, in particular, string tension for $T = 0$ is associated with them. The masses of gluelumps were calculated both analytically in the framework of QCD sum rules [17], as well as in QCD string model [18], and numerically in various lattice calculations [19]. Summarizing all these results, we obtain the correlation length $\lambda_m \approx 0.15$ fm, which corresponds to $M \approx 1.5$ GeV. Since the phase-transition temperature is much lower than the gluelump mass, $T_c \ll M$, it is physically obvious that the temperature dependence of the gluelump mass and, therefore, correlation length must be very weak in the low-temperature region $T < T_c \simeq 300$ MeV under investigation. This behavior is corroborated by both analytic [14] and lattice [13] calculations. We emphasize that the magnetic correlation length does not change its behavior at the phase-transition point. It is well known that the vacuum average of the Polyakov loop is the order parameter for the deconfinement phase transition. Therefore, it is the Polyakov loop correlator $\langle L(\mathbf{x})L^\dagger(0)\rangle$ that significantly changes its behavior at temperature $T = T_c$.

For finite temperature, O(4) Euclidean spacetime symmetry is broken to O(3) space symmetry, and the bilocal correlator is described by independent electric and magnetic correlation functions. These functions are expressed in terms of four independent functions, $D^E(x^2)$, $D_1^E(x^2)$, $D^B(x^2)$, and $D_1^B(x^2)$, as

$$g^2\langle \mathrm{Tr}(E_i(x)\Phi(x,y)E_j(y)\Phi^\dagger(x,y))\rangle = \delta_{ij}\left(D^E + D_1^E + z_4^2\frac{\partial D_1^E}{\partial z^2}\right) + z_i z_j\frac{\partial D_1^E}{\partial z^2},$$

$$g^2\langle \mathrm{Tr}(B_i(x)\Phi(x,y)B_j(y)\Phi^\dagger(x,y))\rangle = \delta_{ij}\left(D^B + D_1^B + \mathbf{z}^2\frac{\partial D_1^B}{\partial z^2}\right) - z_i z_j\frac{\partial D_1^B}{\partial z^2}. \quad (2)$$

Here, $B_i = \frac{1}{2}\varepsilon_{ijk}F_{jk}$ is the chromomagnetic field operator, $E_i = F_{4i}$ is the chromoelectric field operator, $F_{\mu\nu} = F^a_{\mu\nu}t^a$ is the gluon field strength tensor, and

$$\Phi(x,y) = \mathrm{P}\exp\left(igz^\mu\int_0^1 ds A_\mu(y+sz)\right) \quad (3)$$

is the operator of translation along the straight line connecting points x and y, where $z = x - y$. These phase factors Φ are introduced for the gauge invariance of correlators. When these correlators are calculated on a self-dual field, it is obvious that $D_1^E = D_1^B = 0$ and $D^E = D^B$ [12]. Therefore, it is sufficient to consider only the chromomagnetic correlator.

The equality $D^E = D^B$ on instantons means that nonperturbative vacuum cannot be a simple superposition of instanton–anti-instanton field configurations, because lattice calculations show that chromomagnetic and chromoelectric condensates have different temperature dependences. In particular, at the temperature of deconfinement phase transition, chromoelectric condensate decreases abruptly, whereas chromomagnetic condensate virtually does not change [13].

A single-instanton solution for finite temperature, so-called caloron, has the well-known form [20]

$$F^a_{\mu\nu} = \partial_\mu A^a_\nu - \partial_\nu A^a_\mu + g\varepsilon^{abc}A^b_\mu A^c_\nu,$$

$$gB^a_i = -\delta_{ai}g_1(x) + \varepsilon_{aij}\frac{x_j}{r}g_2(x) + \frac{x_a x_i}{r^2}g_3(x),$$

$$E^a_i = B^a_i,$$

$$g_1(x) = \frac{1}{r}\frac{1}{\Pi}\frac{\partial\Pi}{\partial r} + \frac{1}{\Pi}\frac{\partial^2\Pi}{\partial\tau^2} - \frac{1}{\Pi^2}\left(\frac{\partial\Pi}{\partial\tau}\right)^2 + \frac{1}{\Pi^2}\left(\frac{\partial\Pi}{\partial r}\right)^2, \quad (4)$$

$$g_2(x) = -\frac{2}{\Pi^2}\frac{\partial\Pi}{\partial r}\frac{\partial\Pi}{\partial\tau} + \frac{1}{\Pi}\frac{\partial^2\Pi}{\partial r\partial\tau},$$

$$g_3(x) = \frac{2}{\Pi^2}\left(\frac{\partial\Pi}{\partial r}\right)^2 - \frac{1}{\Pi}\frac{\partial^2\Pi}{\partial r^2} + \frac{1}{r}\frac{1}{\Pi}\frac{\partial\Pi}{\partial r}.$$

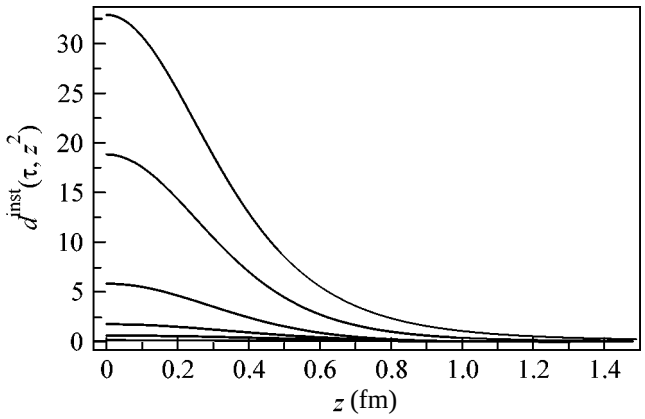

Fig. 1. $d^{\text{inst}}(\tau, z^2)$ for $\tau = 0$, 0.15, 0.3, 0.45, and 0.6 fm and $\rho = 0.3$ fm.

The chromoelectric field is equal to the chromomagnetic field due to the self-duality of the caloron field $F_{\mu\nu} = \tilde{F}_{\mu\nu}$.

Then, it is necessary to calculate the translation operator on the caloron:

$$\Phi(x, y) = \mathrm{P}\exp\left(igz^\mu \int_0^1 ds A_\mu(y + sz)\right)$$

$$= \mathrm{P}\exp\left(-iz^\mu \bar{\eta}^a_{\mu\nu} t^a \int_0^1 ds \partial_\nu \ln\Pi(y + sz)\right)$$

$$= \mathrm{P}\exp\left(-it^a \int_0^1 ds [\bar{\eta}^a_{ij} z_i \partial_j \ln\Pi \right. \quad (5)$$

$$\left. + \bar{\eta}^a_{i4} z_i \partial_4 \ln\Pi + \bar{\eta}^a_{4j} z_4 \partial_j \ln\Pi]\right),$$

$$z = x - y.$$

Implying comparison with lattice calculations, we consider the case $z_4 = 0$. In this case,

$$\Phi(x, y)$$

$$= \mathrm{P}\exp\left(-it^a \int_0^1 ds [\bar{\eta}^a_{ij} z_i \partial_j \ln\Pi + \bar{\eta}^a_{i4} z_i \partial_4 \ln\Pi]\right). \quad (6)$$

It is generally necessary to calculate the integral ordered along the path. However, in particular cases, the exponent for different s values commutes, and the integral is reduced to the calculation of an ordinary exponential. This is obviously the case for $\tau = 0$, $\beta/2$, and β, because $\partial_4 \ln\Pi(r, \tau = 0; \beta/2; \beta) = 0$. Another such case is the field of one instanton, because $\partial_4 \ln\Pi^{\text{inst}} = \tau(1/r)(\partial \ln\Pi^{\text{inst}}/\partial r)$.

To calculate the contribution from the dilute caloron gas to the two-point correlator in the lowest approximation in density, it is necessary to calculate the contribution from one caloron and average it with respect to its position or, what is the same, with respect to y for fixed $z = x - y$.

Averaging with respect to y is reduced to the integral $\int d^4y = \int d^3\mathbf{y} \int_0^\beta dy_4$. Averaging with respect to the three-dimensional vector $\mathbf{y}$ is easy, whereas the integral with respect to y_4 cannot be calculated, because the correlator can be numerically determined only for $\tau = 0$, $\beta/2$, and β, as was mentioned above. Nevertheless, as will be seen from comparison with the case of one instanton, calculation for $\tau = 0$ is sufficient for low temperatures, and the correlation lengths for $\tau = 0$ and $\beta/2$ coincide at high temperatures, and, thereby, averaging with respect to τ is trivial.

We introduce functions d and d_1 as

$$g^2 \langle \mathrm{Tr}(B_i(x)\Phi(x, y)B_j(y)\Phi^\dagger(x, y))\rangle_{\mathbf{y}}$$

$$= \delta_{ij}\left(d + d_1 + \mathbf{z}^2 \frac{\partial d_1}{\partial z^2}\right) - z_i z_j \frac{\partial d_1}{\partial z^2}, \quad (7)$$

where $z_4 = 0$ and d and d_1 are functions of z^2 and $y_4 \equiv \tau$: $d(t, z^2)$ and $d_1(t, z^2)$. By averaging with respect to y_4, we obtain

$$\int_0^\beta d\tau d(\tau, z^2) = D^{\mathrm{B}}(z^2),$$

$$\int_0^\beta d\tau d_1(\tau, z^2) = D_1^{\mathrm{B}}(z^2) = 0, \quad (8)$$

$$D^{\mathrm{B}}(z^2 = 0) = \frac{4\pi^2}{3}.$$

The last equality follows from $g^2 \int d^3\mathbf{y} \int_0^\beta dy_4 (F^a_{\mu\nu})^2 = 32\pi^2$ (this integral is proportional to the topological charge $\sim \int d^4y F\tilde{F}$ due to self-duality).

Let us define the correlation length λ_τ as the parameter in the exponential that provides the best approximation of the function $d(\tau, z^2)$:

$$d(\tau, z^2) \simeq e^{-|z|/\lambda_\tau}. \quad (9)$$

As was discussed above, we calculate only $d(\tau = 0, z^2)$ and $d(\tau = \beta/2, z^2)$. However, this information is sufficient to calculate the correlation length of the function $D^{\mathrm{B}}(z^2)$. Indeed, averaging with respect to τ shows that the functions $d(\tau = 0, z^2)/d(\tau = 0, z^2 = 0)$ and $D^{\mathrm{B}}(z^2)/D^{\mathrm{B}}(z^2 = 0)$, which are normalized to unity, virtually coincide with each other. The matter is that the instanton is a well-localized field configuration, and its

field decreases rapidly with distance from its center. This behavior is illustrated in Fig. 1, which shows the function $d^{\text{inst}}(\tau, z^2)$ calculated on one instanton for several τ values. Since the amplitude of the function $d(\tau, z^2)$ decreases rapidly when τ increases, the profile of the function $D^{\text{B}}(z^2)$ is determined by the function $d(\tau = 0, z^2)$. This is also the case for the caloron for $\beta \gg \rho$, because instantons are well separated in a chain along the time axis. For lower β values, i.e., for $\beta \le 2\rho$, the functions $d(\tau = 0, z^2)$ and $d(\tau = \beta/2, z^2)$ have virtually the same correlation length (see Fig. 2). Thus, averaging with respect to τ is trivial and only changes the amplitude, which is determined by the condition $D^{\text{B}}(z^2 = 0) = 4\pi^2/3$.

In view of the above discussion, we are interested only in the function $d(\tau = 0, z^2)$, whose correlation length is close to the correlation length of the function $D^{\text{B}}(z^2)$ for all β values.

The chromomagnetic correlator for $\tau = 0$, $\beta/2$, and β has the form

$$g^2\langle \mathrm{Tr}(B_i(x)\Phi(x,y)B_j(y)\Phi^\dagger(x,y))\rangle_{\mathbf{y}}$$
$$= g^2\int d^3\mathbf{y}(B_i^a(x)U^{ab}(x,y)B_j^b(y)),$$
$$U^{ab}(x,y) = \mathrm{Tr}(t_a\Phi(x,y)t_b\Phi^\dagger(x,y)) \qquad (10)$$
$$= \frac{1}{2}\delta^{ab}\cos(2\phi) - \frac{1}{2}\varepsilon^{abc}n_c\sin(2\phi) + n_a n_b\sin^2(\phi),$$
$$n_a\phi = \frac{1}{2}\bar{\eta}_{ij}^a z_i y_j\int_0^1 ds\left(\frac{1}{r}\frac{\partial \ln\Pi(y+sz)}{\partial r}\right).$$

The correlator calculated by Eq. (10) was shown in Fig. 3 for various β values. Figure 4 shows the corresponding correlation lengths.

The bilocal correlator on a lattice at finite temperature was calculated in [13], where it was shown that the bilocal correlator of chromomagnetic fields is virtually independent of temperature over the entire range from zero to T_c (the dependence is also weak above the critical temperature). At the same time, Fig. 4 shows that the correlation length of the correlator in the dilute caloron gas changes by about 20% when temperature varies from 0 to 300 MeV. Therefore, the instanton gas cannot provide the correct description of real gluodynamics vacuum. There are several possible explanations of lattice calculations.

(i) The instanton density is much lower than 1 fm^{-4}, and other nonperturbative fields primarily contribute to the correlator and provide confinement. This pattern is consistent with the model of stochastic vacuum.

(ii) The instanton density is high enough for subsequent corrections in density to qualitatively change the result and to lead to the temperature-independent correlation length.

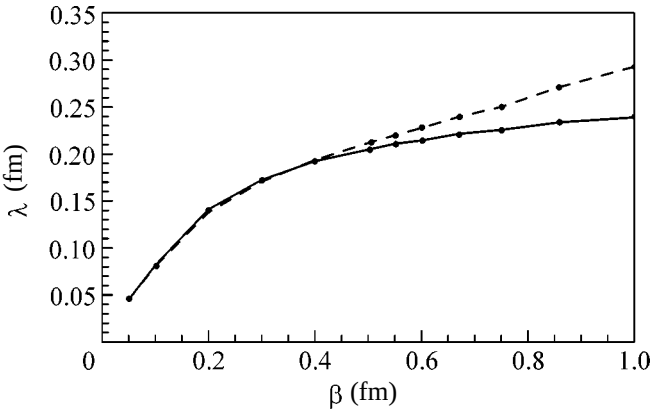

Fig. 2. Correlation lengths (solid line) $\lambda_{\tau=0}(\beta)$ and (dashed line) $\lambda_{\tau=\beta/2}(\beta)$ of the functions $d(\tau = 0, z^2)$ and $d(\tau = \beta/2, z^2)$, respectively, for $\rho = 0.3$ fm.

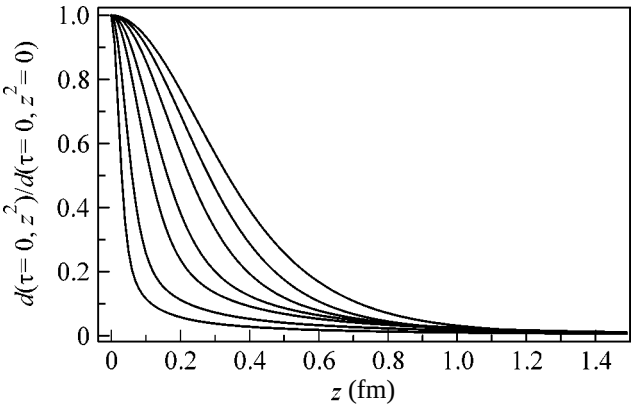

Fig. 3. $d(\tau = 0, z^2)/d(\tau = 0, z^2 = 0)$ for $\beta = 0.05$, 0.1, 0.2, 0.3, 0.5, 0.86, and ∞ fm^{-1} and $\rho = 0.3$ fm. The maximum correlation line shown by the upper line corresponds to zero temperature ($\beta = \infty$), i.e., to the contribution of instantons.

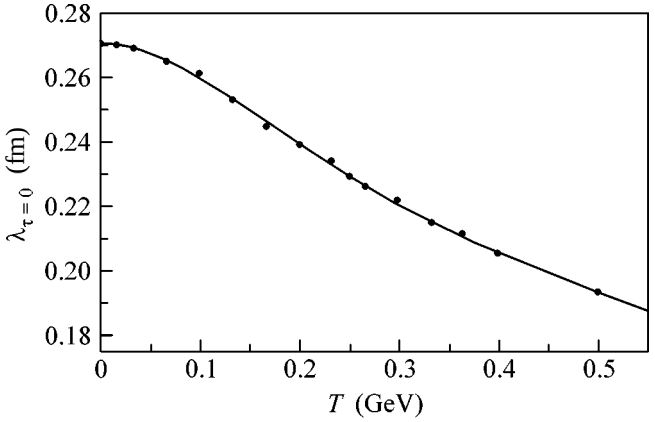

Fig. 4. Temperature dependence of the correlation length $\lambda_{\tau=0}(T)$ for $\rho = 0.3$ fm.

(iii) The configuration of the instanton ensemble changes so that instantons and anti-instantons form molecules, and the contribution from these instanton–anti-instanton molecules considerably differs from the instanton-gas contribution. This pairing can be associated with the deconfinement phase transition. For example, it was shown that instantons and anti-instantons are coupled in molecules in the deconfinement phase in the three-dimensional model with the Higgs field in the adjoint representation [21]. The formation of instanton–anti-instanton molecules in QCD vacuum, as well as connection with the phase transition of the restoration of chiral symmetry, was discussed in review [22].

(iv) It is worth noting that a fundamentally different possible scenario has been discussed recently for caloron vacuum in the confinement phase ($T < T_c$). There are field configurations with nontrivial holonomy, the so-called KvBLL solution [23]. The possibility of caloron decaying into a dyon–antidyon pair is considered in this scenario [24]. The existence of these field configurations for SU(2) and SU(3) groups were corroborated by lattice calculations [25, 26]. In this scenario, the behavior of the correlation length in nonperturbative vacuum is obviously more complex than in the case of the purely caloron gas.

In principle, one can consider another case, where the size distribution of instantons depends on temperature and this dependence is such that the resulting correlation length is independent of T. However, lattice calculations [27] show that the size distribution of instantons does not change over the entire temperature range from 0 to T_c within errors.

In this work, the instanton-gas contribution to the bilocal correlator has been calculated for finite temperature. The comparison of the temperature dependence of the correlation length with lattice calculations provides the conclusion that, if the instanton density is not too high and corrections to the dilute-gas approximation are negligible, the instanton density must be much lower than $n = 1$ fm^{-4}, which is accepted in the instanton-liquid model. The vacuum of non-Abelian gauge theory for finite temperature is a very complex system, and it is natural to assume that it can be a combination of the above possibilities.

We are grateful to Yu.A. Simonov for useful remarks. This work was supported by the Council of the President of the Russian Federation for Support of Young Russian Scientists and Leading Scientific Schools (project no. NSh-1774.2003.2) and by the Ministry of Industry, Science, and Technologies of the Russian Federation (project no. 40.052.1.1.1112).

REFERENCES

1. E. V. Shuryak, Nucl. Phys. B **203**, 93 (1982).
2. D. Dyakonov and V. Y. Petrov, Nucl. Phys. B **245**, 259 (1984).
3. H. G. Dosch, Phys. Lett. B **190**, 177 (1987); H. G. Dosch and Y. A. Simonov, Phys. Lett. B **205**, 339 (1988); Y. A. Simonov, Nucl. Phys. B **307**, 512 (1988).
4. A. Di Giacomo, H. G. Dosch, V. I. Shevchenko, and Y. A. Simonov, Phys. Rep. **372**, 319 (2002).
5. M. A. Shifman, A. I. Vainshtein, and V. I. Zakharov, Nucl. Phys. B **163**, 46 (1980).
6. A. B. Migdal, N. O. Agasyan, and S. B. Khokhlachev, Pis'ma Zh. Éksp. Teor. Fiz. **41**, 405 (1985) [JETP Lett. **41**, 497 (1985)]; N. O. Agasyan and S. B. Khokhlachev, Yad. Fiz. **55**, 1116 (1992) [Sov. J. Nucl. Phys. **55**, 628 (1992)]; Yad. Fiz. **55**, 1126 (1992) [Sov. J. Nucl. Phys. **55**, 633 (1992)].
7. N. O. Agasian and Y. A. Simonov, Mod. Phys. Lett. A **10**, 1755 (1995); N. O. Agasyan, Yad. Fiz. **59**, 317 (1996) [Phys. At. Nucl. **59**, 297 (1996)].
8. N. O. Agasian and S. M. Fedorov, J. High Energy Phys. **0112**, 019 (2001); hep-ph/0111305; hep-ph/0211139; N. O. Agasyan and S. M. Fedorov, Yad. Fiz. **67**, 394 (2004) [Phys. At. Nucl. **67**, 376 (2004)].
9. G. S. Bali, Phys. Rev. D **62**, 114503 (2000).
10. V. I. Shevchenko and Y. A. Simonov, Phys. Rev. Lett. **85**, 1811 (2000); hep-ph/0104135.
11. A. E. Dorokhov, S. V. Esaibegian, and S. V. Mikhailov, Phys. Rev. D **56**, 4062 (1997).
12. E. M. Ilgenfritz, B. V. Martemyanov, S. V. Molodtsov, *et al.*, Phys. Rev. D **58**, 114508 (1998).
13. M. D'Elia, A. Di Giacomo, and E. Meggiolaro, Phys. Rev. D **67**, 114504 (2003).
14. N. O. Agasian, Phys. Lett. B **562**, 257 (2003).
15. G. Boyd, J. Engels, F. Karsch, *et al.*, Nucl. Phys. B **469**, 419 (1996).
16. N. A. Campbell, I. H. Jorysz, and C. Michael, Phys. Lett. B **167**, 91 (1986); I. H. Jorysz and C. Michael, Nucl. Phys. B **302**, 448 (1988).
17. H. G. Dosch, M. Eidemuller, and M. Jamin, Phys. Lett. B **452**, 379 (1999); M. Eidemuller, H. G. Dosch, and M. Jamin, Nucl. Phys. Proc. Suppl. **86**, 421 (2000).
18. Y. A. Simonov, Nucl. Phys. B **592**, 350 (2001).
19. O. Philipsen, Nucl. Phys. B **628**, 167 (2002); M. Laine and O. Philipsen, Nucl. Phys. B **523**, 267 (1998).
20. B. J. Harrington and H. K. Shepard, Phys. Rev. D **17**, 2122 (1978).
21. N. O. Agasian and K. Zarembo, Phys. Rev. D **57**, 2475 (1998); N. O. Agasian and D. Antonov, Phys. Lett. B **539**, 153 (2002).
22. T. Schafer and E. V. Shuryak, Rev. Mod. Phys. **70**, 323 (1998).
23. T. C. Kraan and P. van Baal, Phys. Lett. B **435**, 389 (1998); K. M. Lee and C. H. Lu, Phys. Rev. D **58**, 025011 (1998).
24. E. M. Ilgenfritz, B. V. Martemyanov, M. Muller-Preussker, *et al.*, Phys. Rev. D **66**, 074503 (2002).
25. E. M. Ilgenfritz, B. V. Martemyanov, M. Muller-Preussker, *et al.*, Nucl. Phys. Proc. Suppl. **119**, 754 (2003).
26. C. Gattringer, E. M. Ilgenfritz, B. V. Martemyanov, *et al.*, Nucl. Phys. Proc. Suppl. **129–130**, 653 (2004).
27. B. Lucini, M. Teper, and U. Wenger, hep-lat/0401028.

Translated by R. Tyapaev

JETP Letters, Vol. 80, No. 2, 2004, pp. 83–89. Translated from Pis'ma v Zhurnal Éksperimental'noĭ i Teoreticheskoĭ Fiziki, Vol. 80, No. 2, 2004, pp. 92–98.

Turbulence Spectra Generated by Singularities

E. A. Kuznetsov

Landau Institute for Theoretical Physics, Russian Academy of Sciences, ul. Kosygina 2, Moscow, 119334 Russia
e-mail: kuznetso@itp.ac.ru

Received May 24, 2004

The problem of turbulence spectra generated by the singularities located on lines and planes is considered. It is shown that the frequency spectrum of fluid-surface displacements due to whitecaps (linear singularities) is scaled like a weakly turbulent Zakharov–Filonenko spectrum. The corresponding wave-vector spectrum may be highly anisotropic with a decrease in maximum, as in the Phillips spectrum. However, in the isotropic situation, the spectrum differs markedly from the Phillips form. For a highly anisotropic two-dimensional turbulence, the vorticity jumps can generate the Kraichnan power-law distribution in the region of maximal angular peak. For the isotropic distribution, the turbulence spectrum coincides with the Saffman spectrum. For the shock-generated acoustic turbulence, the spectrum has the form of the Kadomtsev–Petviashvili spectrum $E_\omega \sim \omega^{-2}$ for all spatial dimensionalities. © *2004 MAIK "Nauka/Interperiodica".*

PACS numbers: 47.35.+i; 47.32.Cc; 47.27.-i

1. It is well known that singularities arising due to the nonlinear evolution in continuous media produce power-law tails in the short-wavelength turbulence spectrum. Phillips [1] has resorted to this idea to determine the water-wave turbulence spectrum in the presence of whitecaps, i.e., of singularities at the surface $z = \eta(x, y, t)$. In this case, the second derivative of the vertical surface displacement η has δ singularities, as a result of which the Fourier transform of η decreases as k^{-2} at large wave numbers. Thus, according to Phillips, the $E(k)$ spectrum should be proportional to k^{-3}, which, after recalculation to frequencies $\omega = \sqrt{gk}$, gives [1]

$$E_\omega \sim \omega^{-5}, \tag{1}$$

where E_ω is normalized so that $\int E_\omega d\omega$ is the total energy (per unit area).

When applied to the two-dimensional hydrodynamical turbulence, where the anticipated singularities can be caused by large (according to the Reynolds number) vorticity gradients, the same considerations would give the distribution

$$E(k) \sim k^{-3}, \tag{2}$$

i.e., the distribution coinciding, except for a logarithmic factor, with the Kraichnan spectrum [2] corresponding to a constant enstrophy flux.

However, these simple considerations need closer inspection, because, when deriving Eqs. (1) and (2), it was *implicitly* assumed that the singularities are point-like, although they are distributed and located on lines. Clearly, the difference in the character of singularities should show up in the turbulence spectra. In particular, if the vorticity jumps are distributed isotropically, the turbulence spectrum would be strongly different from distribution (2). Saffman [3] showed that the spectrum in this case has the form

$$E(k) \sim k^{-4}. \tag{3}$$

A similar situation takes place for acoustic turbulence. As was pointed out by Kadomtsev and Petviashvili [4], the role of singularities in this case is played by the shock waves where gas density undergoes jumps. In the three-dimensional case, these singularities are located at surfaces.

In this work, I will examine how the distributed singularities (linear in the two-dimensional systems and surface for the three-dimensional geometry) affect the turbulence spectra, and three particular examples will be given to demonstrate how the turbulence spectra caused by singularities are determined for the surface waves of an infinite-depth fluid, for two-dimensional hydrodynamics with large Reynolds numbers, and for the acoustic turbulence.

This article is organized as follows. Section 2 is devoted to the surface-wave spectra. First, it will be shown that the frequency (Fourier) spectrum of the time autocorrelation function $\langle \eta(t)\eta(t + \tau)\rangle$ of the surface vertical displacement in the presence of cusps (zero-dimensional situation) shows the power-law asymptotic behavior $\sim\omega^{-4}$ at high frequencies. The same behavior is demonstrated by the Zakharov–Filonenko spectrum [5], which is obtained as the exact solution to the kinetic equation for waves in the weak-turbulence approximation. Thus, the Zakharov–Filonenko spectrum is extended to high frequencies, where strongly turbulent processes, such as breaking, become significant. This, in particular, explains the experimentally observed sea frequency spectra [6] (see also [7, 8])

measured over a broad range of angles of inclination, starting with small angles, for which the theory of weak turbulence is operative, and up to the angles where the surface-wave breaking effects become significant. Throughout the entire range, the ω^{-4} law is observed. For a two-dimensional spectrum (Fourier transform of a one-time spatial correlation function) caused by singularities, the situation is basically different. First, the spectrum generated by one singularity is highly anisotropic; it contains two sharp peaks for the directions perpendicular and parallel to the discontinuity, each peak decreasing with increasing k, as in the Phillips spectrum (1). Second, the spectrum in the isotropic situation has the form $E(k) \sim k^{-4}$, i.e., strongly differs from the Phillips spectrum (1). When it is assumed that the relation between the frequency and wave number is the same as for the linear waves, i.e., $\omega = \sqrt{gk}$, then this spectrum would decrease as $\sim\omega^{-7}$ with increasing frequency.

In section 3, the behavior of the two-dimensional turbulence spectra in the presence of the jumps in vorticity Ω (possible candidates for the singularities in the two-dimensional Euler equation) is studied. Although many numerical simulations (cf. [9–17]) for both the Euler equation and Navier–Stokes equation with high Reynolds numbers count in favor of the formation of vorticity jumps, the question of collapse in two-dimensional hydrodynamics still remains open. In this section, the arguments are adduced in favor of collapse and the approach proposed for three-dimensional ideal hydrodynamics [18] and based on the combined Lagrangian–Eulerian description of vortex lines, where each line is numbered by a two-dimensional Lagrange marker, while the other parameter defines the vortex line as such, is developed. In two-dimensional hydrodynamics, the $\mathbf{B} = \mathrm{curl}\Omega$ isolines should be considered instead of vortex lines. This vector proves to be frozen in fluid [19], allowing the construction of an analogue for the vortex-line representation. This description is based on a simple observation: the vector $\mathbf{B}$ changes due to the presence of the velocity component $\mathbf{v}_n$ normal to $\mathbf{B}$, while the tangential component plays a passive role, providing the fulfillment of the incompressibility condition $\mathrm{div}\mathbf{v}_n = 0$. However, the divergence of $\mathbf{v}_n$ is now nonzero, so that the $\mathbf{B}$ isolines can be contracted. The Jacobian of transition to the curvilinear coordinate system moving together with $\mathbf{B}$ is not fixed and different from unity. It is the transformation contractibility that can produce large velocity gradients. It is well known that the singularities in gas dynamics, i.e., in compressible fluid dynamics, appear due to the breaking effect, which is the main cause for the shock-wave formation. From the viewpoint of the classical theory of catastrophes [20], this process is nothing but wrinkling. It is fully characterized by the map describing the transition from the Euler to Lagrange's description. If the Jacobian J of this mapping turns to zero, singularities appear for the derivatives of gas velocity and density.

At the moment, it is unclear whether the singularities in two-dimensional hydrodynamics arise in a finite time or not. Both theoretical investigations and numerical simulations are required to clarify this problem. In this connection, the results obtained by Yudovich in [21] are of great interest. He presented examples of two-dimensional flows for which the vorticity can arise in an infinite time.

If one assumes that the vorticity jumps appear randomly in space, the corresponding short-wavelength spectrum can be found similarly to the surface-wave spectrum. As for the surface gravity waves, the single-singularity spectrum is highly anisotropic with a decrease in the maximal angle, like in the Kraichnan spectrum (2). It is shown in this section that, in the isotropic case, the turbulence spectrum reproduces the Saffman result [3].

The last section is devoted to acoustic turbulence, treated [4] as a random set of shock waves. It is shown that the short-wavelength spectrum of isotropic acoustic turbulence has the wave-vector dependence

$$E(k) \sim k^{-2} \tag{4}$$

for every space dimensionality, i.e., coincides with the original result of Kadomtsev and Petviashvili [4]. Interestingly, the Fourier transform of the density time autocorrelation (single-point) function shows the same power-law decrease in frequency as in the spatial spectrum (4). The reason for this coincidence is likely due to the linear wave-number dependence of sound frequency: $\omega = kc_s$, where c_s is the sound velocity.

2. I start with considering the surface-wave turbulence in an infinite-depth fluid. The dispersion law for linear waves in the gravitational field g is known to be $\omega_k = \sqrt{gk}$. Zakharov and Filonenko found in 1969 the following turbulence spectrum for small-amplitude waves in the weak-turbulence approximation [5]:

$$E_\omega \sim P^{1/3}\omega^{-4}. \tag{5}$$

Here, P is a constant energy flux toward the short-wavelength region, where energy dissipates. Spectrum (5) is obtained as the exact solution to the kinetic equations for waves. In the weak-turbulence approximation, the energy spectral density in the $k - \omega$ representation has the form of δ function

$$E_{k\omega} = \varepsilon(k)\delta(\omega - \omega_k),$$

indicating that the wave ensemble is weakly nonlinear. This allows one to find the $E(\omega)$ distribution from the $\varepsilon(k)$ spectrum using the simple relationship

$$E_\omega = 2\pi k\frac{dk}{d\omega}\varepsilon(k), \tag{6}$$

where $k = \omega^2/g$.

Let us now consider the strongly nonlinear regime, in which whitecaps appear at the fluid surface, i.e., pointlike singularities appear. Let us first calculate the contribution of the one-point autocorrelation function $K(\tau)$ to the spectrum from singularities of this type. To calculate this function, one first measures experimentally the elevation η as a function of time at some point $\mathbf{r}_0$, whereupon $K(\tau)$ is found by the standard scheme:

$$K(\tau) = \langle \eta(t+\tau)\eta(t)\rangle,$$

where the angular brackets stand for averaging. The E_ω spectrum is then obtained by calculating the Fourier transform

$$E_\omega = g\int_{-\infty}^{\infty} K(\tau)e^{i\omega\tau}d\tau.$$

To determine the contribution to the E_ω spectrum from the pointlike surface singularities, one should first take into account that, at the instant t_i of cusp passage through the measurement point $\mathbf{r}_0$, the second derivative $\partial^2\eta/\partial t^2$ is proportional to $\delta(t-t_i)$, i.e.,

$$\frac{\partial^2\eta}{\partial t^2} = \sum_i \Gamma_i\delta(t-t_8) + \text{regular terms}. \qquad (7)$$

Let us now assume that Γ_i and times t_i are random quantities and calculate the contribution from the singular terms in Eq. (7) to the spectrum. The Fourier transform of these terms is

$$\eta_\omega = -\frac{1}{\omega^2}\sum_i \Gamma_i e^{-i\omega t_i}. \qquad (8)$$

Here,

$$\eta_\omega = \int_{-\infty}^{\infty}\eta(t)e^{i\omega t}dt, \quad \eta(t) = \frac{1}{2\pi}\int_{-\infty}^{\infty} e^{-i\omega t}\eta_\omega d\omega.$$

To find the E_ω spectrum, one should square the absolute value of (8) and average the resulting expression. The averaging over times t_i yields

$$E_\omega = \frac{g}{2\pi T}\langle|\eta_\omega|^2\rangle = \frac{g\nu}{2\pi\omega^4}\overline{\Gamma^2}, \qquad (9)$$

where $\nu = N/T$ is the cusp appearance frequency, N is the number of discontinuities in the averaging time T, and $\overline{\Gamma^2}$ is the average value of Γ^2.

It is essential that the frequency dependence of this expression is the same as for the weakly turbulent Zakharov–Filonenko spectrum (5). However, strictly speaking, one cannot use Eq. (9) to reconstruct the wavelength-scale energy distribution using Eq. (6), as was done for the weakly turbulent regime. This requires independent calculation.

Consider first a single wave ridge with a cusp of length $l = x_1 - x_2$ parallel to the y axis and centered at the point (x_0, y_0). In this case,

$$\frac{\partial^2\eta}{\partial y^2} = \Gamma(x)\delta(y-y_0) + \text{regular terms}. \qquad (10)$$

Here, $\Gamma(x)$ is a continuous function of x on the interval $[x_1, x_2]$ with zeros at the endpoints of the interval ($\Gamma(x_{1,2}) = 0$) and outside the interval.

Then, the Fourier transform of the singular part in Eq. (10) is given by the integral

$$\eta_k = -\frac{1}{k_y^2}e^{-ik_y y_0}\int_{x_1}^{x_2}\Gamma(x)e^{-ik_x x}dx,$$

where $\mathbf{k} = (k_x, k_y)$. This is the contribution from one singularity. The total contribution from all discontinuities is given by

$$\eta_k = -\sum_\alpha \frac{e^{-i(\mathbf{k}\mathbf{n}_\alpha)y_\alpha}}{(\mathbf{k}\mathbf{n}_\alpha)^2}\int_{x_{1\alpha}}^{x_{2\alpha}}\Gamma_\alpha(x)e^{-i(\mathbf{k}\tau_\alpha)x}dx.$$

Here, $\mathbf{n}_\alpha$ and τ_α are, respectively, the normal and unit vector to the discontinuity, and y_α, $x_{1\alpha}$, and $x_{2\alpha}$ are the discontinuity coordinates defining, along with $\mathbf{n}_\alpha$ and τ_α, the position and orientation of the discontinuity α.

To find the turbulence spectrum, one should average $|\eta_k|^2$ over all random variables. Assuming that the discontinuity coordinates (x_α, y_α) are distributed uniformly, the averaging over these variables gives

$$|\eta_k|^2 = N\left\langle\left|\frac{1}{(\mathbf{k}\mathbf{n})^4}\int_{x_1}^{x_2}\Gamma(x)e^{-i(\mathbf{k}\tau)x}dx\right|^2\right\rangle. \qquad (11)$$

Here, N is the mean number of discontinuities per S and the angular brackets stand for the averaging over Γ, x_1, x_2, and angles.

Our interest is with the short-wavelength asymptotic behavior of (11), $kL \gg 1$, where L is the characteristic discontinuity length, so that, at $|\mathbf{k}\tau|L \gg 1$, the integral in Eq. (11) is for a rapidly oscillating function. In this limit, it can be evaluated using the stationary phase method. This method applies to all angles θ_k (θ_k is the angle between the vectors $\mathbf{k}$ and $\mathbf{n}$), except for a narrow cone $kL\theta_k \le 1$. In this region, the integral can be taken to be independent of k. The resulting $\tilde{\epsilon}(\mathbf{k})$ spectrum (prior to angular averaging!) in this angular region has the form

$$\tilde{\epsilon}_1(\mathbf{k}) \approx \frac{gn}{4\pi^2 k^4}\langle(\bar{\Gamma}l)^2\rangle, \quad \theta_k \le (kL)^{-1}, \qquad (12)$$

where n is the mean density of discontinuities (per unit area),

$$\bar{\Gamma} l = \int_{x_1}^{x_2} \Gamma(x)dx, \quad l = x_l - x_2, \quad L = \langle l \rangle.$$

For angles θ_k larger than $(kL)^{-1}$, the integral is estimated using the stationary phase method. However, the leading order proportional to $|\mathbf{k}\tau|^{-1}$ gives zero value, because $\Gamma(x_{1,2}) = 0$. The nonzero contribution to the spectrum $\tilde{\epsilon}(k)$ appears in the next order in $|(\mathbf{k}\tau)L|^{-1}$:

$$\tilde{\epsilon}_2(\mathbf{k}) = \frac{gn}{2\pi^2} \frac{\langle (\Gamma')^2 \rangle}{(\mathbf{kn})^4 (\mathbf{k}\tau)^4}, \tag{13}$$

where Γ' denotes the derivative of $\Gamma(x)$ on the ends of the interval x_i. One can see from this relation that the spectrum $\epsilon_2(k)$ contains singularities at angles θ_k close to 0 and $\pi/2$. For small angles $\theta_k \approx (kL)^{-1}$, expression (12) matches Eq. (13). For angles close to $\pi/2$, one should take into account the bending of the discontinuity line. If a is the characteristic value of bending, Eq. (13) is valid in the region $|\theta_k - \pi/2| > (ka)^{-1}$.

Distributions (12) and (13) allow one to calculate the energy spectrum, i.e., the distribution of energy $E(\mathbf{k}) = k\overline{\tilde{\epsilon}(\mathbf{k})}$ in scales, where $\overline{\tilde{\epsilon}(\mathbf{k})}$ is the value of $\tilde{\epsilon}(\mathbf{k})$ averaged using the angular distribution function.

For the isotropic turbulence, this averaging amounts to the integration of Eqs. (12) and (13) over angles θ_k. The integration of expression (12) gives

$$E_1(k) = 2k \int_{-\theta_0}^{\theta_0} \tilde{\epsilon}_1(k)d\theta = \frac{gn}{\pi^2 k^4 L} \langle (\bar{\Gamma} l)^2 \rangle. \tag{14}$$

In the integration of Eq. (13) over angles, the main contribution to the spectrum comes from angles close to 0, π, and $\pm\pi/2$, where spectrum (13) has singularities. For $\theta \longrightarrow 0(\pi)$, the integration is cut off at angles $\theta_k = \pm\theta_0(\pi \pm \theta_0)$, and for $\theta \longrightarrow \pm\pi/2$, it is cut off angles $|\pi/2 \pm \theta_k| \approx (ka)^{-1}$. The averaging gives

$$E_2(k) = \frac{2gn}{3\pi^2 k^4} \langle (\Gamma')^2 \rangle (L^3 + a^3). \tag{15}$$

The final result for the spectrum in the isotropic case is given by the sum of Eqs. (14) and (15):

$$E(k) = \frac{gn}{\pi^2 k^4 L} \left[\langle (\bar{\Gamma} l)^2 \rangle + \frac{2}{3} \langle (\Gamma')^2 \rangle (L^3 + a^3) \right], \tag{16}$$

which differs by one power of k from the Phillips spectrum. After recalculating this spectrum as in Eq. (1), i.e., setting $k = \omega^2/g$ in Eq. (16), one obtains the ω^{-7} power instead of ω^{-5}. At the same time, we see that frequency spectrum (9) behaves as $\sim\omega^{-4}$ and not as ω^{-5} or, the more so, as ω^{-7}, which is quite evident, because, in the strongly nonlinear regime corresponding to the appearance of discontinuities, the frequency ω and k are not related to each other by $\omega = \sqrt{gk}$, as they were in the weak-turbulence regime, and, moreover, there is no relation between frequency spectrum (9) and wavenumber distribution (16). If such a relation exists, then

$$\frac{dk}{k^4} \sim \frac{d\omega}{\omega^4},$$

i.e., the relation between frequency ω and k would be linear instead of quadratic for weakly nonlinear waves.

If the angular distribution is sufficiently narrow, e.g., if all falling wave crests are oriented unidirectionally (this can be caused, e.g., by the coast and/or wind), then the spectrum will have a sharp peak in this direction. If the width $\Delta\theta$ of angular distribution is narrower than θ_0, i.e., if $\Delta\theta < \theta_0$, then the spectrum $E(k, \theta)$ in the cone $\theta < \Delta\theta$ will decrease as $\sim k^{-3}$, i.e., as in the Phillips spectrum. Note, however, that this asymptotic behavior is intermediate, because $\theta_0 = (kL)^{-1}$ decreases with increasing k. For this reason, when averaging over angles, singularities in (13) become essential for $\theta \longrightarrow 0$, and, starting at certain $k = k^*$, the spectrum will decrease as k^{-4} at $k > k^*$.

3. The situation with two-dimensional turbulence in the limit of large Reynolds numbers Re is analogous to the surface waves if, following Saffman, one assumes that singularities appear in vorticity gradient, i.e., the vorticity $\Omega(\mathbf{r})$ has jumps whose width δ is smaller than the characteristic scales of turbulence. As was pointed out in section 1, the appearance of sharp vorticity gradients was observed in many numerical experiments (see, e.g., [9–15]) that simulate turbulence with large Reynolds numbers, i.e., in the regime where, as a zero approximation, one can consider the Euler equation instead of the Navier–Stokes equation. For this reason, the question whether this process can be described within the framework of Euler equation is of basic importance; and, if so, whether it proceeds in a finite time or not. In this section, some considerations are presented in favor of this statement.

Consider the Euler equation for vorticity $\Omega = \partial v_y/\partial x - \partial v_x/\partial y$:

$$\frac{\partial \Omega}{\partial t} + (\mathbf{v}\nabla)\Omega = 0 \text{ with } \mathrm{div}\mathbf{v} = 0. \tag{17}$$

It follows from this equation that Ω is the Lagrangian invariant. Following Weiss' work [19], we introduce the divergence-free vector $\mathbf{B}$ with the components

$$B_x = \frac{\partial \Omega}{\partial y}, \quad B_y = -\frac{\partial \Omega}{\partial x}.$$

This vector is directed along the tangent to the isolines $\Omega(\mathbf{r}) = \text{const}$. The equation of motion for $\mathbf{B}$ can easily

be obtained after the differentiation of Eq. (17) with respect to the coordinates:

$$\frac{\partial \mathbf{B}}{\partial t} = \mathrm{curl}[\mathbf{v} \times \mathbf{B}], \quad (18)$$

i.e., **B** is a frozen-in quantity and obeys the same equation as does magnetic field in ideal magnetic hydrodynamics. One can see from Eq. (18) that **B** changes due to the velocity component $\mathbf{v}_n$ normal to **B**. The tangential velocity component $\mathbf{v}_\tau$ plays a passive role, providing the condition $\mathrm{div}\mathbf{v} = 0$. It is this fact that plays the key role in the derivation of vortex-line representations for a three-dimensional ideal fluid (see [24]). In the same way as in [24], we introduce new trajectories that are determined by the normal velocity component:

$$\frac{d\mathbf{r}}{dt} = \mathbf{v}_n(\mathbf{r}, t); \quad \mathbf{r}|_{t=0} = \mathbf{a}. \quad (19)$$

The solution to this system of equations defines the mapping

$$\mathbf{r} = \mathbf{r}(\mathbf{a}, t). \quad (20)$$

Since trajectories (20) are specified not by the velocity but by its normal component, the Jacobian J of transformation (20) is not fixed and can take arbitrary values. This fact directly follows from the equation

$$\frac{dJ}{dt} = \mathrm{div}\mathbf{v}_n J; \quad J = \det\|\partial x_i/\partial a_j\|, \quad (21)$$

which is obtained from Eq. (19) by differentiation with respect to the variables **a**, followed by the use of the Liouville formula. Since $\mathrm{div}\mathbf{v}_n \neq 0$, the Jacobian J can change, in contrast to the transition from the Eulerian to the Lagrangian description.

Equation (18) can be integrated using relations (19)–(21):

$$\mathbf{B}(\mathbf{r}, t) = \frac{(\mathbf{B}_0(\mathbf{a}) \cdot \nabla_a)\mathbf{r}(\mathbf{a}, t)}{J}, \quad (22)$$

where $\mathbf{B}_0(\mathbf{a})$ is the initial value of **B**.

Note once more that, due to the compressibility of mapping (20), the Jacobian J can take arbitrary values, including zeros. As is well known, the appearance of discontinuities (singularities in the density and velocity field) in gas dynamics is due to the mapping compressibility in the transformation from the Eulerian to the Lagrangian description. From the viewpoint of classical theory of catastrophes, the appearance of discontinuities in gas dynamics in the simplest situation corresponds to the formation of the mapping folds (see, e.g., [20]), which corresponds to zero values of the mapping Jacobian. For this reason, it would appear natural that this process also occurs in two-dimensional hydrodynamics. At the very least, numerous experiments and some theoretical speculations (see, e.g., [22]) count in favor of this point of view.

Hereafter, following Saffman [3], we assume that vorticity jumps appear in two-dimensional turbulence at large Reynolds numbers. The width δ of the jumps is determined from the balance between the inertial and viscous forces. As in section 2, we are interested in the short-wavelength region with k values lying in the interval

$$L^{-1} \ll k \ll \delta^{-1},$$

where L is the characteristic (energy-containing) scale of turbulence.

To find the spectrum of discontinuities, we first write, as in the case of surface waves, the expression for the gradient Ω of a single discontinuity, assuming that it is oriented along y:

$$\frac{\partial \Omega}{\partial y} = G(x)\delta(y - y_0) + \text{regular terms},$$

where $G(x)$ is a nonzero continuous function on the interval $[x_1, x_2]$ and $G(x_{1,2}) = 0$, after which we will sum up over all discontinuities.

Then, we find the Fourier amplitude Ω_k for the ensemble of discontinuities:

$$\Omega_k = -i\sum_\alpha \frac{e^{-i(\mathbf{kn})y_\alpha}}{(\mathbf{kn}_\alpha)} \int_{x_{1\alpha}}^{x_{2\alpha}} G_\alpha(x) e^{-i(\mathbf{k}\tau_\alpha)x} dx. \quad (23)$$

The energy spectrum $\epsilon(k)$ is found from this expression using the relation

$$\epsilon(k) = \frac{\overline{|\Omega(k)|^2}}{8\pi^2 S k^2}, \quad (24)$$

where it is taken into account that the Fourier transform of velocity $\mathbf{v}_k$ is related to Ω_k by the equality $\Omega_k = i[\mathbf{k} \times \mathbf{v}_k]$. Hence, it follows by analogy with Eqs. (12) and (13) that the spectrum $\epsilon(k)$ is written in the form

$$\epsilon_1(k) = \frac{n}{8\pi^2 k^4}\langle(\bar{G}l)^2\rangle, \quad \theta_k \leq \theta_0; \quad (25)$$

$$\epsilon_2(k) = \frac{n}{4\pi^2 k^2}\frac{\langle(G')^2\rangle}{(\mathbf{kn})^2(\mathbf{k}\tau)^4}, \quad \theta_k > \theta_0. \quad (26)$$

Here, n is the density of discontinuities (per unit area) and G' denotes the derivative of G taken at the ends of the interval x_α.

In the isotropic case, the energy spectrum $E(k)$ is given by

$$E(k) = \frac{n}{2\pi^2 k^4 L}\left[\langle(\bar{G}l)^2\rangle + \frac{2L^4}{3}\langle(G')^2\rangle\right],$$

in accordance with the Saffman result [3].

In the strongly anisotropic case with unidirectionally oriented discontinuities, spectrum (25) and (26) has a sharp peak in the anisotropy direction. If the width

$\Delta\theta$ of angular distribution function is narrower than $\theta_0 = (kL)^{-1}$, the energy spectrum decreases at this peak as $\sim k^{-3}$, i.e., coincides with the power-law Kraichnan spectrum. At $k > k^*$ (k^* is defined just as in the preceding section), this asymptotic behavior changes to the Saffman form k^{-4}.

4. The aforesaid can directly be used to calculate the acoustic turbulence. According to Kadomtsev and Petviashvili [4], acoustic turbulence is understood as an ensemble of shock waves randomly distributed in space. Shock waves as density jumps represent singularities. Thus, the problem associated with the spectrum of acoustic turbulence is similar, in this respect, to the aforementioned problems.

In contrast to the examples of two-dimensional systems considered above, a change in the spectrum of acoustic turbulence can be followed for different spatial dimensionalities D, starting with $D = 1$ and ending with three dimensionalities.

For $D = 1$, the derivation differs from (9) only by small details, giving[1]

$$E_1(k) = \frac{n_1 c_s^2}{2\pi\rho_0 k^2}\overline{(\Delta\rho)^2}. \quad (27)$$

Here, n_1 is the density of discontinuities per unit length, c_s is the sound velocity, ρ_0 is the mean density of a medium (per unit length), and $\overline{(\Delta\rho)^2}$ is the mean-square density jump at the discontinuity.

Based on the preceding calculations, the energy spectrum $E(k)$ of the isotropic $D = 2$ turbulence can be written in the form

$$E_2(k) = \frac{n_2 c_s^2}{\pi^2\rho_0 k^2 L}\left[\langle(\overline{\Delta\rho} l)^2\rangle + \frac{2}{3}\langle(\Delta\rho')^2\rangle L^3\right], \quad (28)$$

where n_2 is the density of discontinuities per unit area and the meaning of $\overline{\Delta\rho}$, l, and $\Delta\rho'$ is just the same as for (12).

Thus, the $E(k)$ spectrum as a function of k behaves in the same manner for both the one- and two-dimensional cases: it decreases proportionally to k^{-2}.

It turns out that the spectrum of isotropic turbulence behaves similarly also for $D = 3$. The corresponding calculation differs only slightly from $D = 2$. The difference is that one must additionally integrate over angles in the discontinuity plane. We do not present these calculations in this work and only demonstrate how the same result can be simply obtained in a different way on the basis of one-dimensional spectrum (27). Consider the density correlation function for isotropic turbulence:

$$\phi(y_1) = \langle\rho(x_1 + y_1, x_2, x_3)\rho(x_1, x_2, x_3)\rangle.$$

Its Fourier spectrum (with respect to only the y_1 variable!) is given by an expression that coincides, except for a factor, with Eq. (27):

$$\phi_k = \frac{N_1}{2\pi k^2}\overline{(\Delta\rho)^2}, \quad (29)$$

where N_1 is understood as the mean linear density of discontinuities. The function ϕ_k is related to the three-dimensional Fourier spectrum

$$\Phi(|\mathbf{k}|) = \int\phi(\mathbf{r})e^{-i(\mathbf{kr})}d\mathbf{r}$$

by the obvious formula

$$\phi_{k_1} = \int\Phi(|\mathbf{k}|)d\mathbf{k}_\perp = \pi\int_{k_1^2}^{\infty}\Phi(s)ds^2.$$

By differentiating this equality with respect to k_1, we obtain

$$\Phi(k) = -\frac{1}{2\pi k}\frac{d\phi_k}{dk}.$$

Then, using Eq. (29), one obtains for the spectrum $E_3(k)$

$$E_3(k) = \frac{2N_1 c_s^2}{\pi\rho_0 k^2}\overline{\Delta\rho^2}.$$

The same manipulations can be used to calculate two-dimensional spectrum (28). However, Saffman showed [3] that one should solve the Abel equation when operating with $\Phi(k)$.

I am grateful to V.E. Zakharov and J.J. Rasmussen for discussion. This work was supported by the Russian Foundation for Basic Research (project no. 00-01-00929), INTAS (grant no. 00-00292), and the program for the support of leading scientific schools of the Russian Federation.

[1] Spectrum (27) was first obtained, likely, by Burgers in [23] and, in the many-dimensional statement, by Kadomtsev and Petviashvili (see below).

REFERENCES

1. O. M. Phillips, J. Fluid Mech. **4**, 426 (1958); in *Wind Waves* (Inostrannaya Literatura, Moscow, 1962), p. 219.
2. R. Kraichnan, Phys. Fluids **11**, 1417 (1967).
3. P. G. Saffman, Stud. Appl. Math. **50**, 49 (1971).
4. B. B. Kadomtsev and V. I. Petviashvili, Dokl. Akad. Nauk SSSR **208**, 794 (1973) [Sov. Phys. Dokl. **18**, 115 (1973)].
5. V. E. Zakharov and N. N. Filonenko, Dokl. Akad. Nauk SSSR **170**, 1292 (1967) [Sov. Phys. Dokl. **11**, 881 (1967)].
6. Y. Toba, J. Oceanogr. Soc. Jpn. **29**, 209 (1973).

7. M. Donelan, M. Hamilton, and W. H. Hui, Philos. Trans. R. Soc. London, Ser. A **315**, 509 (1985).
8. O. M. Phillips, J. Fluid Mech. **156**, 505 (1985).
9. D. K. Lilly, J. Fluid Mech. **45**, 395 (1971).
10. J. C. McWilliams, J. Fluid Mech. **146**, 21 (1984).
11. S. Kida, J. Phys. Soc. Jpn. **54**, 2840 (1985).
12. M. E. Brachet, M. Meneguzzi, and P. L. Sulem, Phys. Rev. Lett. **57**, 683 (1986).
13. R. Benzi, S. Patarnello, and P. Santangelo, Europhys. Lett. **3**, 811 (1986).
14. B. Legras, B. Santangelo, and R. Benzi, Europhys. Lett. **5**, 37 (1988); B. Santangelo, R. Benzi, and B. Legras, Phys. Fluids A **1**, 1027 (1989).
15. K. Okhitani, Phys. Fluids A **3**, 1598 (1991).
16. B. Legras and D. Dritschel, Appl. Sci. Res. **51**, 445 (1993).
17. A. H. Nielsen, X. He, J. J. Rasmussen, and T. Bohr, Phys. Fluids **8**, 2263 (1996).
18. E. A. Kuznetsov and V. P. Ruban, Pis'ma Zh. Éksp. Teor. Fiz. **67**, 1015 (1998) [JETP Lett. **67**, 1076 (1998)]; Phys. Rev. E **61**, 831 (2000).
19. J. Weiss, Physica D (Amsterdam) **48**, 273 (1991).
20. V. I. Arnol'd, *Catastrophe Theory* (Znanie, Moscow, 1981; Springer, Berlin, 1986); *Mathematical Methods of Classical Mechanics*, 3rd ed. (Nauka, Moscow, 1984; Springer, New York, 1989).
21. V. I. Yudovich, Chaos **10**, 705 (2000).
22. D. G. Dritschel, Phys. Fluids A **5**, 984 (1993); J. Fluid Mech. **293**, 269 (1995).
23. J. M. Burgers, *Lecture in California Institute of Tech.* (1951) (unpublished).
24. E. A. Kuznetsov, Pis'ma Zh. Éksp. Teor. Fiz. **76**, 406 (2002) [JETP Lett. **76**, 346 (2002)].

Translated by V. Sakun

JETP Letters, Vol. 80, No. 2, 2004, pp. 90–94. Translated from Pis'ma v Zhurnal Éksperimental'noĭ i Teoreticheskoĭ Fiziki, Vol. 80, No. 2, 2004, pp. 99–103.

Decay of a Turbulent Cascade of Capillary Waves at the Surface of Liquid Hydrogen

M. Yu. Brazhnikov[1, *], G. V. Kolmakov[1], A. A. Levchenko[1], L. P. Mezhov-Deglin[1], A. N. Sil'chenko[2], and P. V. E. McClintock[2]

[1] *Institute of Solid-State Physics, Russian Academy of Sciences, Chernogolovka, Moscow region, 142431 Russia*
**e-mail: makc@issp.ac.ru*
[2] *Department of Physics, Lancaster University, Lancaster, LA1 4YB, UK*
Received May 31, 2004

Free decay of a turbulent cascade of capillary waves was experimentally studied at the surface of liquid hydrogen after switching off harmonic pumping. It was found that the cascade starts to decay at the high-frequency side of the frequency spectrum and proceeds in the quasi-stationary regime. The characteristic relaxation time of the whole cascade proves to be close to the viscous-damping time of the wave, whose frequency coincides with the surface-excitation frequency. © *2004 MAIK "Nauka/Interperiodica".*

PACS numbers: 47.35.+i; 47.27.-i

INTRODUCTION

This work is a continuation of our studies of the turbulence in a system of capillary waves at the surface of liquid hydrogen [1] and is devoted to studying the relaxation of a turbulent cascade of capillary waves after switching off the driving force (pump).

In the theory of weak wave turbulence [2, 3], the statistical distribution of "occupation numbers" n_ω for capillary waves can be described by the kinetic equation

$$\frac{\partial n_\omega}{\partial t} = \mathrm{st}(n) - 2\gamma_\omega n_\omega + F_{\mathrm{drive}}(t), \qquad (1)$$

where st(n) is the collision integral, γ_ω is the viscous-damping coefficient of capillary waves, and $F_{\mathrm{drive}}(t)$ corresponds to the external pumping. According to [4], $\gamma_\omega = 2\nu(\rho/\sigma)^{1/3}\omega^{4/3}$, where ν is viscosity, σ is the surface tension coefficient, and ρ is the fluid density. The relation between the capillary-wave frequency ω and the wave vector k is determined by the dispersion law $\omega^2 = (\sigma/\rho)k^3$; i.e., the spectrum is of the decay type. For this reason, the main contribution to the collision integral that is responsible for the energy redistribution between waves in the k space comes from the three-wave interaction events, for which the decay of one wave into two waves and confluence of two waves into a single wave proceed with energy and momentum conservation.

In the inertial frequency interval, i.e., interval between the pumping region (low frequencies) and the energy dissipation region (high frequencies), the wave dynamics are mainly governed by the nonlinear wave interactions. For a broadband perturbation by a low-frequency noise, the steady-state solution to kinetic equation (1) in the inertial interval is the isotropic spectrum of capillary turbulence (Kolmogorov spectrum):

$$n_\omega \sim Q^{1/2}\omega^{-15/6}, \qquad (2)$$

where the energy flux Q is directed from low- to high-frequency waves.

The Kolmogorov spectrum of capillary turbulence was observed in the experimental studies of nonlinear-wave dynamics at the surface of water [5–7] and at the surface of liquid hydrogen [1]. In a real experiment, the surface deviations $\eta(\mathbf{r}, t)$ from the equilibrium position are measured. For this reason, to make the comparison of experimental results with the theoretical predictions more convenient, distribution (2) can be rewritten in terms of the Fourier components of the correlation function $I(\tau) = \langle \eta(\mathbf{r}, t+\tau)\eta(\mathbf{r}, t)\rangle$ of surface elevations. In the frequency representation, the correlation function describing the turbulence cascade can be represented as

$$I_\omega \equiv \langle |\eta_\omega|^2 \rangle \sim \omega^{-1/3} n_\omega \sim \omega^{-17/6}. \qquad (3)$$

Numerical calculations [3, 8] and the results of our measurements [1] showed that the exponent in the spectrum of correlation function (3) changes from –17/6 for the broadband pumping by a low-frequency noise to –3.5 for the harmonic pumping at a fixed frequency ω_p.

Experiments with liquid hydrogen [9] allowed us to determine the high-frequency edge of the inertial interval, i.e., the boundary frequency ω_b to which the power-law spectrum of capillary turbulence extends. It was found that, as the amplitude of surface oscillations at the pump frequency η_p decreases, the boundary frequency ω_b shifts to low frequency as $\omega_b \sim \eta_p^{1.3}$.

0021-3640/04/8002-0090$26.00 © 2004 MAIK "Nauka/Interperiodica"

It is clear that, after pumping is switched off ($F_{\text{drive}}(t) = 0$), the surface relaxes to its equilibrium unperturbed state. In monograph [3], the scenario for self-similar relaxation of the turbulent cascade is considered in the inertial interval without taking into account the viscous loss; i.e., the second term in kinetic equation (1) is set to zero from very beginning. One of the most important consequences of this scenario is that the cascade decay should start from the low frequencies, so that, with time, the energy-containing portion of the spectrum (maximum of the distribution I_ω) shifts to high frequencies. However, it remained unclear whether this scenario can be realized under the real conditions.

In this work, the results of experimental study of the decay of turbulent oscillations at the charged surface of liquid hydrogen are reported and the data on a change in the correlation function I_ω with time after steplike switching off of the harmonic pumping are presented.

The merit of liquid hydrogen in these experiments is that it has a very low density and low viscosity; the nonlinear-interaction coefficient $V \sim (\sigma/\rho^3)^{1/4}k^{9/4}$ of capillary waves at the hydrogen surface is three times as large as, e.g., at the water surface. The oscillations of charged surface can be excited by an ac electric field, allowing one to change in a controllable way the characteristics of perturbation source, such as amplitude of the external field directly applied to the surface and the perturbation frequency spectrum, and to observe the relaxation of free surface oscillations of fluid after switching off the external pumping.

EXPERIMENTAL

The design of the apparatus and the method of measuring were discussed in detail in [10]. An optical cell was placed in a vacuum cavity of a helium cryostat. A flat horizontal capacitor was mounted in the cell. Gaseous hydrogen was condensed into a cylindrical container formed by the lower capacitor plate and a guard ring. The collection of hydrogen was stopped when the fluid surface reached the guard ring.

A radioactive target was attached to the lower plate. A positive electric voltage applied to the lower plate extracts positive ions from the ionized fluid layer adjacent to the target surface and draws them in the liquid-hydrogen surface, where they form a quasi-two-dimensional charged layer. To prevent the charge going away to the container walls, a voltage equal to the voltage at the lower plate was applied to the guard ring. The field of the charged layer fully compensates the electric field inside the fluid.

In the preliminary experiments, the container diameter was 25 mm and the depth was 3 mm (small cell). Most of the data presented below were obtained in a large cell with a container 60 mm in diameter and 6 mm in depth. The gap between the fluid surface and the upper capacitor plate in both cells was equal to 4 mm.

The oscillations of the charged liquid-hydrogen surface were excited by an ac electric field by applying, in addition to the dc voltage, an ac voltage to the guard ring. The maximal ac voltage amplitude on the guard ring did not exceed 100 V, and the dc voltage was equal to 1400–1600 V. Experiment [1, 10] showed that, in fields on the order of 4000 V/cm, the dispersion law for the excited surface waves was close to the capillary type $\omega \sim k^{3/2}$ at frequencies higher than 10 Hz.

In the experiments, the temperature of liquid hydrogen was equal to 15.5 K.

The oscillations of the hydrogen surface were detected from a change in the power of a laser beam reflected from the surface. The reflected beam was focused by a lens onto a photodetector. The ac voltage component on the photodetector was amplified and read in a computer using a 16-bit analog-to-digital converter with a polling frequency of 40 kHz. The write time varied from 2 to 10 s. Measurements were carried out for various pump frequencies $\omega_p/2\pi$ in the range from 20 to 400 Hz. The angular amplitude of surface oscillations did not exceed 0.04 rad (which corresponds to a wave height of 0.04 mm at a frequency of 100 Hz).

The correlation function I_ω of surface deviations from the unperturbed state can be reproduced from the known Fourier spectrum of the reflected laser-beam power [10]. These experiments were carried out in the "wide-beam" regime, for which the Fourier harmonic of the reflected power P_ω is proportional to the Fourier harmonic of the surface elevation η_ω. Correspondingly, the correlation function is

$$I_\omega \equiv \langle |\eta_\omega|^2 \rangle \sim P_\omega^2.$$

RESULTS

The waves at the fluid surface were excited by a harmonic pumping at a fixed frequency ω_p for a time on the order of 10 s, which is sufficient for establishing the steady-state turbulent distribution in the system of capillary waves. Then, the pumping was switched off and the relaxation of free surface oscillations with time was observed.

In Fig. 1, fragments of the time-dependent photodetector signals $P(t)$ recorded at a pump frequency of (a) $\omega_p/2\pi = 98$ Hz in the small cell and (b) 97 Hz in the large cell are shown. At time $t = 0$, the harmonic pumping is switched off and the oscillation amplitude starts to decrease. The low-frequency modulation of the signals shown in Fig. 1 is due to the uncontrolled surface oscillations caused by the cryostat vibrations. One can see in Fig. 1 that the decay in the small cell proceeds appreciably faster than in the large cell. Clearly, the specific energy loss by friction on the container bottom and walls is much stronger than in the large cell. For this reason, the detailed measurements of the relaxation processes were carried out with the large cell.

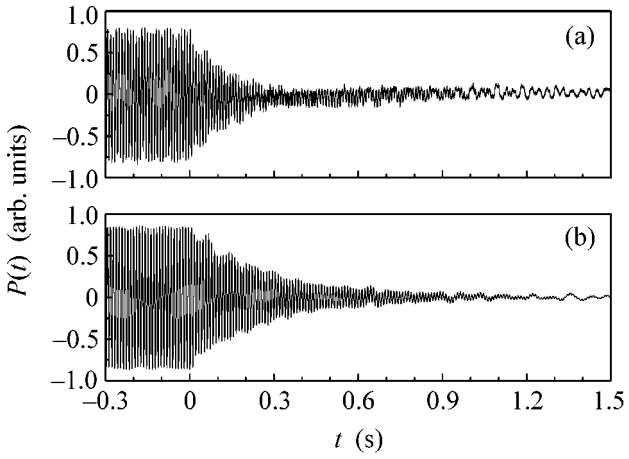

Fig. 1. Relaxation of the liquid-hydrogen surface oscillations after switching off pumping with frequency $\omega_p/2\pi$ at $t = 0$. (a) Small cell, $\omega_p/2\pi$ = 98 Hz, and (b) large cell, $\omega_p/2\pi$ = 97 Hz.

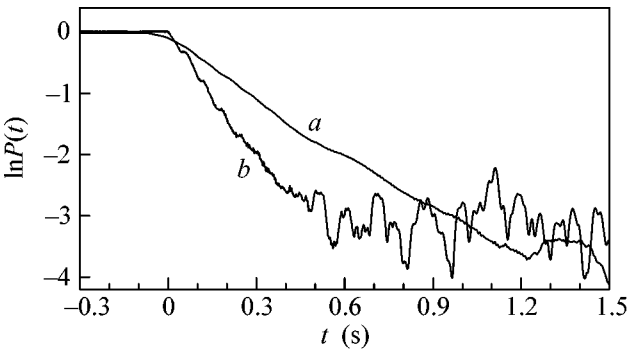

Fig. 2. Time dependence of the signal amplitude $P(t)$ recorded in the large cell. Pump frequency $\omega_p/2\pi$ is (*a*) 97 and (*b*) 173 Hz.

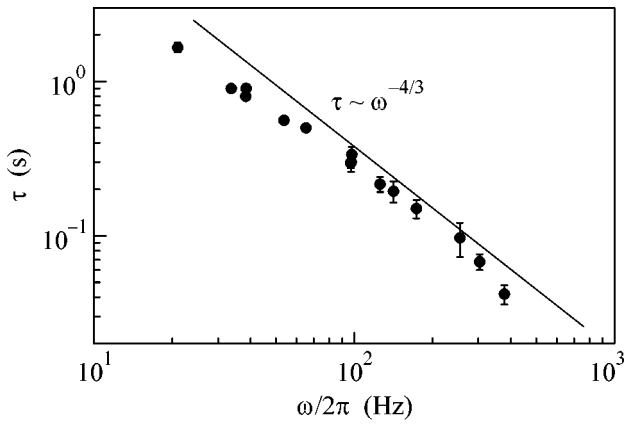

Fig. 3. Frequency-dependent relaxation time of the amplitude η_p for the wave with pump frequency ω_p (log–log plot). Solid line corresponds to the viscous-damping time of the capillary wave with frequency ω_p, as calculated with the known viscosity of liquid hydrogen.

In Fig. 2, the time dependences of the signal amplitudes $P(t)$ obtained for pump frequencies of (*a*) 97 and (*b*) 173 Hz are obtained by averaging the absolute value of $P(t)$ over a time interval that is a multiple of the half-period of the fundamental harmonic. It turned out that the decrease in the signal amplitude with time after switching off pumping can be described by the exponential law $P(t) \sim \exp(-t/\tau)$, where the time constant $\tau = (0.3 \pm 0.03)$ s for the frequency $\omega_p/2\pi$ = 97 Hz and $\tau = (0.15 \pm 0.02)$ s for a pump frequency of 173 Hz. The dependence of the decay time constant τ on $\omega_p/2\pi$ is shown in Fig. 3 on the log–log scale. The solid line corresponds to the viscous-damping time $\tau_\omega = \gamma_\omega^{-1} \sim \omega^{-4/3}$ of a linear wave at the liquid-hydrogen surface, as calculated using the known liquid-hydrogen parameters at a temperature of 15.5 K [11]. One can see that the experimental points fall rather close to the calculated τ_ω dependence.

To study the time evolution of the spectrum I_ω of the correlation function, we used the short-time Fourier transform procedure [12]. The validity of this method of analysis is based on the fact that the experimentally observed signal time decay is much longer than the period of the harmonic force exciting the surface; i.e., $\tau_\omega \gg 2\pi/\omega_p$. This allows the choice of a time window with a size smaller than the signal time decay but much larger than the period of the exciting force. By shifting the window position in time, we succeeded in studying the evolution of the turbulent cascade at the liquid-hydrogen surface after switching off pumping. The surface oscillation spectra P_ω^2 for a pump frequency of 97 Hz are shown in Fig. 4 at various instants of time after switching off pumping: after (a) 0.03, (b) 0.34, and (c) 1.07 s.

Immediately after switching off pumping, the spectrum $I_\omega \sim P_\omega^2$ of the correlation function (Fig. 4a) is close to the steady-state distribution of the nonlinear surface oscillations for the narrow-band pumping [1]. The fundamental peak is positioned at a pump frequency of 97 Hz, while the higher harmonics form a cascade with the power-law frequency dependence $P_\omega^2 \sim \omega^{-3.5}$ of their peak heights. The arrow indicates the position of the high-frequency edge $\omega_b \approx 5$ kHz of the inertial interval. At time $\Delta t = 0.34$ s after switching off pumping (Fig. 4b), the wave amplitude at frequency ω_p decreased approximately by a factor of 3, as compared to Fig. 4a, while the boundary frequency ω_b decreased to ≈2.4 kHz. The final decay stage after Δt = 1.07 s, when only a few harmonics are excited, is shown in Fig. 4c. It is remarkable that, over a rather long time interval $\Delta t \lesssim 0.6$ s after switching off pumping, the high-frequency portion of the spectrum can be described by the distribution $P_\omega^2 \sim \omega^{-3.5}$, which is typical of the steady-state cascade; i.e., the spectrum shape is retained in the course of vibrational relaxation, but

the surface oscillations start to decay on the high-frequency portion of the spectrum.

DISCUSSION

The observation of a quasi-stationary spectrum over a rather long time after switching off pumping allows one to assume that the nonlinear-interaction time of the capillary waves is much shorter than the viscous-damping time of a linear wave at the pump frequency ω_p even in the case where the surface-oscillation amplitude at pump frequency $\omega_p/2\pi = 97$ Hz becomes one order of magnitude smaller than its initial value: it decreases from 0.02 mm 0.03 s after switching off pumping to 0.002 mm after 0.6 s (Figs. 4a, 4b). As a result, the relatively intense energy exchange between waves with frequencies lying in the inertial interval results in the stabilization of the power-law spectrum in the low-frequency region $\omega < \omega_b$. At the same time, it follows from the experiment (see Figs. 3, 4) that the characteristic relaxation time of surface oscillations is determined by the viscous damping of waves at the pump frequency, and the cascade decay is accompanied by moving the high-frequency edge ω_b of inertial interval to low frequencies. Hence, when describing the relaxation of nonlinear fluid-surface oscillations within the framework of kinetic equation (1), one should not ignore viscous loss even at larger, for our experiment, surface-oscillation amplitudes $k\eta_p \lesssim 0.04$ rad, which corresponds to $\eta_p \lesssim 0.02$ mm for a pump frequency of 97 Hz.

Recent numerical calculations [13] including viscous damping of capillary waves over the entire range of frequencies $\gamma_\omega \sim \omega^{4/3}$ have shown that, after switching off pumping, the system rather rapidly (in a time on the order of nonlinear-interaction time) transmits a considerable portion of energy from the low-frequency region (on the order of the pump frequency) to high frequencies through the nonlinear channel, i.e., through the energy transfer in the form of cascade. During the further evolution, the role of nonlinear interaction at low frequencies becomes lower. In even further evolution, the viscous damping becomes the main decay mechanism for a wave with a frequency equal to the pump frequency, while the role of nonlinear interaction with high-frequency waves becomes negligible because of the small amplitudes of the latter. Quite the reverse, the wave amplitudes in the high-frequency portion of the spectrum below ω_b are mainly determined by the interaction with the low-frequency surface oscillations, whose oscillation amplitude exceeds the amplitudes of high-frequency waves by several orders of magnitude. Therefore, the evolution of the high-frequency portion of the spectrum is determined by the nonlinear properties of the system. Upon further decrease in the surface-wave amplitudes (at times $t \gtrsim$ 1 s for a pump frequency of 97 Hz), the boundary frequency ω_b becomes on the order of the pump frequency and the viscous damping dominates over the nonlinear energy transfer for all energies (Fig. 4c).

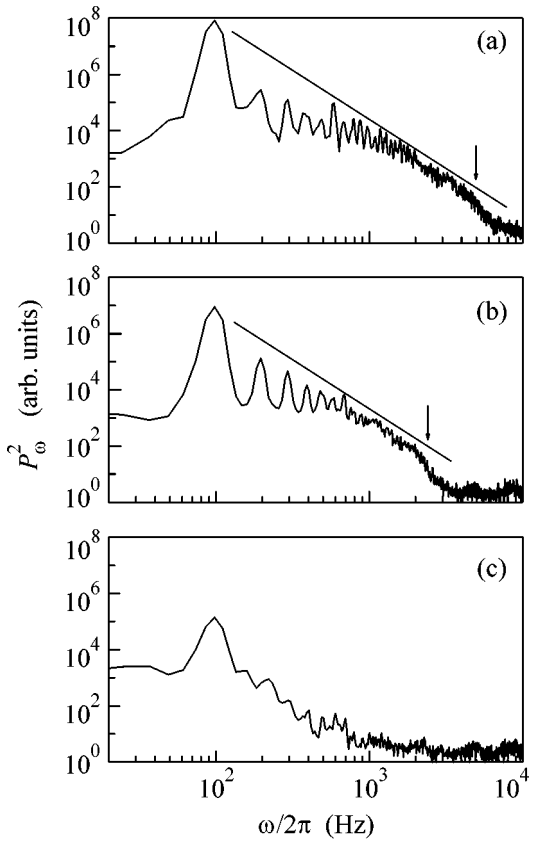

Fig. 4. Oscillation spectra of the liquid-hydrogen surface in the large cell at different times after switching off pumping: after Δt = (a) 0.03, (b) 0.34, and (c) 1.07 s. The solid line corresponds to the power law $P_\omega^2 \sim \omega^{-7/2}$. The arrow indicates the position of the high-frequency edge ω_b of the inertial interval.

It is worth noting that this scenario is realized for the capillary-wave systems in our experiments because the inertial interval is bounded by frequencies on the order of 5–10 kHz. From the general theory [3], it follows that, in the case of a rather broad frequency inertial interval (in the idealized case of infinitely small viscosity, the width of inertial interval tends to infinity), the nonlinear interaction of capillary waves has a local character, so that the interaction of waves with close frequencies dominates. It follows from our studies that, under real experimental conditions (with a finite inertial interval), the nonlocal interaction of high-frequency waves with the low-frequency waves makes a contribution that is comparable with the local part of interaction. This determines the observed features in the decay of the turbulent state of capillary waves at the charged liquid-hydrogen surface.

CONCLUSIONS

The quasi-stationary decay of the turbulent cascade of capillary waves has been experimentally observed at the liquid-hydrogen surface after switching off the low-frequency pumping. The decay starts from high frequencies and ends in a time close to the viscous-damping time of the wave with the pump frequency. The energy-containing portion of the spectrum (maximum of the distribution I_ω) is retained at low frequencies during the entire decay process. This indicates that, when considering the relaxation processes in the system of capillary waves at the fluid surface, one should take into account the contribution from viscous damping.

We are grateful to V.N. Khlopinskiĭ for assistance in preparing experiments and to V.E. Zakharov, E.A. Kuznetsov, and M.T. Levinsen for discussions. This work was supported in part by the Russian Foundation for Basic Research (project nos. 01-02-97037 and 03-02-16865), INTAS (grant no. 2001-0618), and the Ministry of Industry and Science of the Russian Federation (contract no. 40.012.1.1.11.64). G.V. Kolmakov is grateful for the support of the Foundation for Assistance of Domestic Science (Russian Federation) and the Leverhulme Trust Foundation (UK).

REFERENCES

1. M. Yu. Brazhnikov, G. V. Kolmakov, A. A. Levchenko, and L. P. Mezhov-Deglin, Fiz. Nizk. Temp. **27**, 1183 (2001) [Low Temp. Phys. **27**, 876 (2001)].
2. V. E. Zakharov and N. N. Filonenko, J. Appl. Mech. Tech. Phys. **4**, 506 (1967).
3. V. E. Zakharov, G. Falkovich, and V. S. L'vov, *Kolmogorov Spectra of Turbulence I* (Springer, Berlin, 1992).
4. L. D. Landau and E. M. Lifshitz, *Course of Theoretical Physics*, Vol. 6: *Fluid Mechanics*, 4th ed. (Nauka, Moscow, 1988; Pergamon, New York, 1987).
5. W. Wright, R. Hiller, and S. Putterman, J. Acoust. Soc. Am. **92**, 2360 (1992).
6. E. Henry, P. Alstrom, and M. T. Levinsen, Europhys. Lett. **52**, 27 (2000).
7. M. Yu. Bazhnikov, G. V. Kolmakov, A. A. Levchenko, and L. P. Mezhov-Deglin, Europhys. Lett. **58**, 510 (2002).
8. G. E. Fal'kovich and A. B. Shafarenko, Zh. Éksp. Teor. Fiz. **94**, 172 (1988) [Sov. Phys. JETP **67**, 1393 (1988)].
9. M. Yu. Brazhnikov, G. V. Kolmakov, A. A. Levchenko, and L. P. Mezhov-Deglin, Pis'ma Zh. Éksp. Teor. Fiz. **74**, 660 (2001) [JETP Lett. **74**, 583 (2001)].
10. M. Yu. Brazhnikov, A. A. Levchenko, and L. P. Mezhov-Deglin, Prib. Tekh. Éksp. **45**, 31 (2002).
11. *The Properties of Condensed Phases of Hydrogen and Oxygen*, Ed. by B. I. Verkin (Naukova Dumka, Kiev, 1984) [in Russian].
12. Shie Qian and Dapang Chen, *Joint Time–Frequency Analysis—Methods and Applications* (Prentice Hall, Upper Saddle River, N.J., 1996).
13. G. V. Kolmakov, A. A. Levchenko, M. Yu. Brazhnikov, *et al.*, Phys. Rev. Lett. (in press).

Translated by V. Sakun

JETP Letters, Vol. 80, No. 2, 2004, pp. 95–97. Translated from Pis'ma v Zhurnal Éksperimental'noĭ i Teoreticheskoĭ Fiziki, Vol. 80, No. 2, 2004, pp. 104–106.

Dissociation of CF_2HCl Molecules by Intense Radiation from a Femtosecond Laser in the Near-IR Range

V. M. Apatin, V. O. Kompanets, V. B. Laptev, Yu. A. Matveets, E. A. Ryabov*, S. V. Chekalin, and V. S. Letokhov

Institute of Spectroscopy, Russian Academy of Sciences, Troitsk, Moscow region, 142190 Russia

**e-mail: ryabov@isan.troitsk.ru*

Received June 9, 2004

It is found that CF_2HCl molecules dissociate under irradiation by high-intensity pulses of femtosecond radiation ($\lambda = 1.8$ μm) in the vicinity of resonance with the frequency of overtone vibrational transitions in the C–H bond. It is shown that the dissociation products substantially differ from the products of dissociation of CF_2HCl molecules from the ground and excited electronic states under the action of IR and UV nanosecond pulses. © *2004 MAIK "Nauka/Interperiodica".*

PACS numbers: 33.80.Gi; 33.20.Tp

1. The ideas that laser radiation can be used for initiating photoinduced processes in atoms and molecules and their subsequent control appeared almost immediately after the invention of lasers. This primarily concerns the realization of selective processes. In the case of molecules, two types of selectivity exist: *intermolecular and intramolecular.* In the former case, we are speaking of the possibility of selective action (e.g., dissociation or ionization) on molecules of selected species in their mixture, including a mixture of various isotopic isomers. In the latter case, we mean the realization of processes selective with respect to a preferred molecular bond or a group of bonds.

A number of methods for obtaining intermolecular selectivity have been proposed and implemented (see [1, 2]). These methods were mainly based on resonant single- and multiphoton excitation of vibrational states by pulsed IR radiation within the ground electron level. Subsequent reaction may occur upon the transfer of vibrationally excited molecules to the higher electronic states with the help of the next UV radiation pulse. The development of this approach was termed "vibrationally mediated photodissociation" (see [3, 4]). In polyatomic molecules, when one of the molecular vibrations is in resonance of intense IR radiation, these molecules may dissociate under the action of IR radiation alone as a result of IR multiphoton excitation (IR MPE and MPD) (see [5–7] for details). Isotopically selective IR MPD [8] forms the basis of one of the most effective methods for laser isotope separation, which has been implemented on a commercial scale [9].

At the same time, the possibility to obtain *intramolecular* selectivity (in particular, selective rupture of a certain bond or a group of bonds) remained unrealized for a long time. This is due to a fundamental constraint imposed by intramolecular vibrational redistribution (IVR) (see, for example, [4, 6]) leading to stochastization of vibrational motion starting from a certain energy E_{st} and, hence, to the loss of excitation mode selectivity. The value of E_{st} for relatively small polyatomic molecules amounts to $(4–7) \times 10^3$ cm^{-1} [10]. The characteristic IVR time lies in the subpicosecond range [4]. As a result, IR MP dissociation of molecules upon their vibrational excitation under the action of pulses of a duration of 10^{-7}–10^{-9} s is always statistical by nature, since dissociation always occurs along the weakest bond, irrespective of the vibration that was excited initially. The development of IR femtosecond lasers paved the way to a basically new possibility for overcoming limitations imposed by the IVR. A number of approaches to mode-selective excitation were proposed, including the control of the dynamics of reactions themselves [11–13]. The observation of the nonstatistical nature of dissociation of a number of molecules as a result of their IR MPE through one of the fundamental vibrations was reported in recent publications [14, 15].

2. Here, we report on the dissociation of CF_2HCl molecules under the action of femtosecond pulses in the near-IR range. A CF_2HCl molecule exhibits a stretching vibration of the C–H bond, whose frequency ν_1 amounts to 3021.3 cm^{-1} [16]. The lasing frequency of a femtosecond source $\nu_{las} = 5502$ cm^{-1} ($\lambda = 1.8$ μm) was chosen in the vicinity of the lower overtone transitions of the ν_1 mode, which amount to 5927.3 cm^{-1} (($v = 0$) $\longrightarrow$ ($v = 2$)) and 5502 cm^{-1} (($v = 2$) $\longrightarrow$ ($v = 4$)), respectively [16].

In our experiments, we used a femtosecond laser system consisting of Ti : Sapphire muster oscillator (Tsunami HP), a regenerative amplifier (Spitfire HP), and a parametric amplifier OPA-800 (all devices are

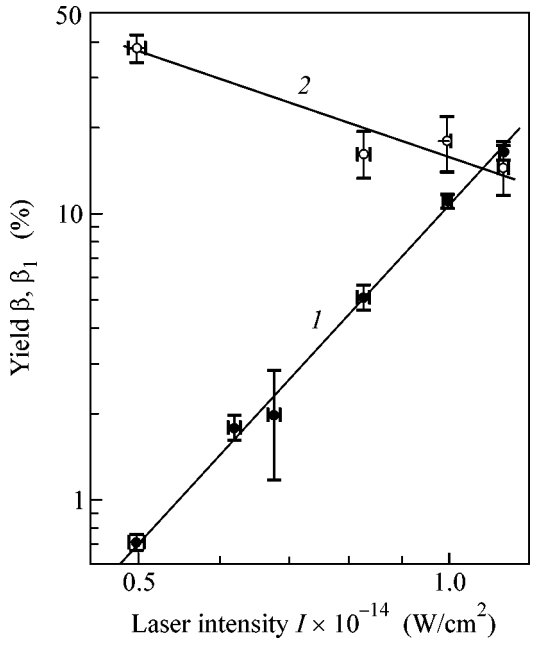

CF_2HCl dissociation yield β (curve *1*) and the relative yield β_1 of product CF_3H (curve *2*) as functions of the laser intensity.

manufactured by Spectra Physics). The radiation pulse duration at a wavelength of 1.8 μm after parametric amplification was ~100 fs, the pulse energy was up to 0.1 mJ, and the pulse repetition rate was 1 kHz. Laser radiation was focused onto a cell (of length 4 cm and volume $V_0 = 2.8$ cm^3) filled with gaseous CF_2HCl by a CaF_2 lens with $f = 3$ cm. The radiant energy density distribution at the focus was close to the Gaussian distribution with a radius of $r_0 = 13$ μm (at the $1/e$ level). The total caustic length was $2l = 520$ μm (l is the Rayleigh length); consequently, the volume of the dissociation region was $V \approx 4.2 \times 10^{-7}$ cm^3. The pressure of CF_2HCl in all experiments was $p = 1.0$ mmHg. The amount of initial CF_2HCl was controlled and the dissociated products were analyzed from the IR absorption spectra recorded by a Specord-82M spectrophotometer.

In the course of experiments, it was found that the exposure of CF_2HCl to femtosecond pulses at a wavelength of $\lambda = 1.8$ μm and a radiant energy density above $\Phi \approx 4.9$ J/cm^2 ($I_0 \approx 4.9 \times 10^{13}$ W/cm^2) induced dissociation of CF_2HCl molecules, and the amount of the substance in the cell decreased with increasing number m of radiation pulses. A quantitative characteristic of the process is the dissociation yield β, viz., the fraction of molecules dissociated in the irradiated volume per pulse. The value of β was determined from the relation

$$N = N_0(1 - \beta\Gamma)^m,$$

where N and N_0 are the final and initial amounts of CF_2HCl in the cell and $\Gamma = V/V_0$. As the radiation intensity increases, the dissociation yield increases in accordance with the power law $\beta \sim I^n$, where $n = 3.9 \pm 0.1$ (curve *1* in the figure). The only new gaseous product of dissociation of CF_2HCl by femtosecond radiation which could be detected in these experiments from the IR spectra was the CF_3H molecule. The dependence of the relative yield β_1 of CF_3H (β_1 is the fraction of dissociated CF_2HCl molecules transformed into CF_3H) on the radiation intensity is shown in the figure (curve *2*). The value of β_1 amounts to ≈38% for $I \approx 5.0 \times 10^{13}$ W/cm^2 and decreases with increasing radiation intensity. It should be noted that irradiation of pure CF_3H by laser pulses up to the maximal possible intensity $I = 1.1 \times 10^{14}$ W/cm^2 did not cause the dissociation of these molecules.

3. The formation of CF_3H upon irradiation of CF_2HCl by femtosecond pulses distinguishes this process from other known methods of excitation. For example, as a result of thermal pyrolysis of CF_2HCl, the decomposition of this molecule occurs via the channel with the lowest energy,

$$CF_2HCl \longrightarrow CF_2 + HCl, \quad (1)$$

and the subsequent reactions yield predominantly C_2F_4, as well as a certain amount of C_3F_6 [17]. In the case of IR multiphoton excitation of CF_2HCl by pulsed (10^{-7}–10^{-6} s) radiation of a CO_2 laser within the ground electronic state, the dissociation of CF_2HCl molecules also occurs according to reaction (1), and C_2F_4 is the final product (with a yield of ≳99%) of IR MPD of CF_2HCl [18]. When dissociation of CF_2HCl is induced by UV radiation in the range of $\lambda \approx 200$ nm through an excited electronic state, two dissociation channels exist [19]:

$$CF_2HCl \longrightarrow CF_2H + Cl, \quad (2)$$

$$CF_2HCl \longrightarrow CF_2Cl + H. \quad (3)$$

The end products of these reactions are halogenated products of ethane.

The difference between the results of femtosecond irradiation, as compared to those in the above processes, especially as compared to the IR MPD induced by radiation from a CO_2 laser, where dissociation is purely statistical, is obviously due to the difference in the primary products of dissociation of CF_2HCl molecules. The change in the relative yield β_1 of CF_3H upon a change in the intensity of femtosecond radiation indicates the existence of several (at least two) dissociation channels of a CF_2HCl molecule exposed to radiation. The change in the relative contribution from these channels leads to a change in the composition/ratio of the primary products and, hence, in the composition/ratio of the end products of subsequent reactions (in our case, the relative yield of CF_3H).

Our experiments form the initial stage in the investigation of possible nonstatistical effects in the vibrational excitation of molecules by femtosecond IR radi-

ation in the ground electron state. Further experiments should throw more light on this problem. As regards the nature of the observed dissociation of CF_2HCl, the possible mechanisms of this process include various types of dissociative ionization. These processes were observed for a number of molecules during their irradiation by femtosecond pulses with an intensity of $\sim 10^{14}$ W/cm^2 at a wavelength of 800 or 400 nm as a rule (see [20–22] and the references cited therein). Further experiments will provide a more definite answer to the question about the mechanism of dissociation of CF_2HCl (in our case), the extent of deviation of excitation process from resonance, and the primary products of dissociation.

This study was supported by the Russian Foundation for Basic Research (project nos. 03-02-16736 and NSh-1772.2003.2).

REFERENCES

1. V. S. Letokhov, Science **180**, 451 (1973).
2. V. S. Letokhov and C. B. Moore, in *Chemical and Biochemical Applications of Lasers*, Ed. by C. B. Moore (Academic, Orlando, 1977), Vol. 3, Chap. 1, pp. 1–165.
3. F. F. Crim, J. Phys. Chem. **100**, 12725 (1996).
4. D. J. Nesbitt and R. W. Field, J. Phys. Chem. **100**, 12735 (1996).
5. V. S. Letokhov, *Nonlinear Selective Photoprocesses in Atoms and Molecules* (Nauka, Moscow, 1983) [in Russian].
6. V. N. Bagratashvili, V. S. Letokhov, A. A. Makarov, and E. A. Ryabov, *Multiple Photon Infrared Laser Photophysics and Photochemistry* (Harwood Academic, Chur, 1985).
7. D. W. Lupo and M. Quack, Chem. Rev. **87**, 181 (1987).
8. R. V. Ambartsumyan, V. S. Letokhov, E. A. Ryabov, and N. V. Chekalin, Pis'ma Zh. Éksp. Teor. Fiz. **20**, 597 (1974) [JETP Lett. **20**, 273 (1974)].
9. V. Yu. Baranov, A. P. Dyadkin, D. D. Malyuta, *et al.*, Proc. SPIE **4116**, 314 (2000).
10. A. L. Malinovsky, E. A. Ryabov, and V. S. Letokhov, Chem. Phys. **139**, 229 (1989).
11. D. Tannor and S. J. Rice, J. Chem. Phys. **83**, 5013 (1985).
12. P. Brummer and M. Shapiro, Chem. Phys. Lett. **126**, 541 (1986).
13. H. Rabitz, R. de Vivie-Riedle, M. Motzkus, and K. Kompa, Science **288**, 824 (2000).
14. L. Windhorn, T. Witte, J. S. Yeston, *et al.*, Chem. Phys. Lett. **357**, 85 (2002).
15. L. Windhorn, J. S. Yeston, T. Witte, *et al.*, J. Chem. Phys. **119**, 641 (2003).
16. A. Brown, D. C. McKean, and J. L. Dunkan, Spectrochim. Acta A **44**, 553 (1988).
17. M.-C. Su, S. S. Kumar, K. P. Lim, *et al.*, J. Phys. Chem. **100**, 15827 (1996).
18. R. I. Martinez and J. T. Herron, Chem. Phys. Lett. **84**, 180 (1981).
19. A. Melchior, P. Knupfer, I. Bar, *et al.*, J. Phys. Chem. **100**, 13375 (1996).
20. A. N. Markevich, N. P. Moore, and R. J. Levis, Chem. Phys. **267**, 131 (2001).
21. M. Lezius, V. Blachet, M. Yu. Ivanov, and A. Stolow, J. Chem. Phys. **117**, 1575 (2002).
22. Z.-H. Liu, Y. Q. Wang, J.-J. Ma, *et al.*, Chem. Phys. Lett. **383**, 198 (2004).

Translated by N. Wadhwa

JETP Letters, Vol. 80, No. 2, 2004, pp. 98–102. Translated from Pis'ma v Zhurnal Éksperimental'noĭ i Teoreticheskoĭ Fiziki, Vol. 80, No. 2, 2004, pp. 107–111.

Monomer Counterrotations and Tunneling Splitting in CO Dimer by Data of Millimeter Wave Spectroscopy

B. S. Dumesh[1, *], V. A. Panfilov[1], L. A. Surin[1, 2], D. N. Furzikov[1], and G. Winnewisser[2]

[1]*Institute of Spectroscopy, Russian Academy of Sciences, Troitsk, Moscow region, 142190 Russia*

[2]*Physical Institute 1, University of Cologne, Cologne, Germany*

**e-mail: Dumesh@isan.troitsk.ru*

Received June 2, 2004; in final form, June 16, 2004

Analysis of the rotational spectrum of the molecular dimer $(CO)_2$ measured in the millimeter wave range has been performed and four new rotational states are revealed. Three of these states are characterized by almost free rotations of both monomers in the dimer. These states have approximately the same first term σ in the expansion of the rotational energy in powers of the rotational angular momentum J for various values of the momentum projections on the dimer axis ($K = 0, 1, 2$) and various rotational constants B. The intrinsic rotational angular momenta of CO dimers, $j_1 = j_2 = 1$, are determined from the σ value. In addition, a state with $K = 2$ is found which corresponds to one of the known shape isomers of $(CO)_2$. The values of the tunneling splitting for each of the new states are determined. The results indicate that previous data on the suppressed tunneling are determined by the asymmetry of internal rotations in the CO monomers rather than by the K value. © *2004 MAIK "Nauka/Interperiodica".*

PACS numbers: 33.20.Sn; 33.20.Bx

This paper is devoted to analysis of the results of investigating the rotational spectra of the $(CO)_2$ molecular dimer. Our aim was to find the states in which both dimers exhibit nearly free rotations and to determine the tunneling splitting in these states. This problem has a certain prehistory. As the coupling of monomers in the molecular complex decreases, their internal motions become freer and freer. However, the problem of existence of stable complexes with almost free monomer rotations is nontrivial because of the presence of anisotropic van der Waals interaction. Previously, such rotations were found for the most part in the complexes of small molecules (such as CH_4 [1] and CO [2]) with inert gas atoms, where these motions do not lead to any qualitative transformation of the spectra: the difference from the rigid top case is purely quantitative (at a relatively low accuracy of calculation of the rotational spectra).

Therefore, it was interesting to study the rotational spectra of weakly bound complexes composed of two molecules, in which the rotations of monomer must lead to the appearance of new states with the same energy and different projections (K) of the total rotational angular momentum (J) onto the intermolecular axis. Recently, such states where both monomers are rotating with the moments $j = 1$ and $K = 1$ or 2 were found in the N_2–CO complex [3], which is close to $(CO)_2$ in both shape and binding energy. However, states with $K = 0$ belonging to the same group were not found.

Under laboratory conditions, CO dimers (characterized by low binding energies) are created by means of a supersonic gas jet technique. Using this method, it is possible to obtain molecular beams with low (several kelvins) effective translational and rotational temperatures. However, the concentration of $(CO)_2$ dimers is still rather small and the measurement of their spectra requires highly sensitive equipment. Rovibronic absorption bands occur in the IR range, in the region of fundamental vibrations of CO molecule, while the transitions between tunneling-split levels are observed predominantly in the upper part of the millimeter wavelength range.

The CO dimers exist in the form of two shape isomers: CO–OC (O-bound) and OC–CO (C-bound) with an energy difference as small as 1.5 cm^{-1}. Both isomers have a distance between monomers of about 0.4 nm, which is large as compared to the CO monomer size (0.1 nm). The existence of these shape isomers was theoretically predicted by Bunker *et al.* [4] and confirmed as a result of interpretation of the IR spectra of $(^{12}C^{16}O)_2$ [5, 6] and $(^{13}C^{16}O)_2$ [7]. The tunneling splitting was measured in the millimeter wave spectra of $(^{12}C^{16}O)_2$ [8, 9] and $(^{13}C^{16}O)_2$ [10]. When this study was initiated, a total of 48 rotational levels with the energies within 0–9.5 cm^{-1} (measured from the lowest level) and rotational angular momenta $J = 0$–8 had been known in the spectrum of $(^{12}C^{16}O)_2$. These levels belong to four rotational states (two for each shape isomer) with projections of the rotational angular momentum on the intermolecular axis $K = 0$ and 1.

0021-3640/04/8002-0098$26.00 © 2004 MAIK "Nauka/Interperiodica"

It was found that the tunneling splitting significantly decreases in the states with $K = 1$ [9], although, in other dimers of similar shape (but higher binding energy), this splitting either increases, as in $(HF)_2$ [11], or remains constant, as in $(HCl)_2$ [12]. In addition, the tunneling splitting in $(CO)_2$ exhibited an anomalous dependence on the isotope mass [10]: in the O-bound isomer, the splitting was inversely proportional to the reduced mass μ, while, in the C-bound isomer, the splitting increased with μ. In the ground state ($K = 0$), this increase is small and can be rather interpreted as a weak dependence of the splitting on the reduced mass. In the state with $K = 1$, the increase in splitting is quite large, amounting to 13%, which is significantly greater than all uncertainties involved in data processing. Note that no such anomalies in the dependence of tunneling splitting on the isotope mass take place for $(HF)_2$ and $(HCl)_2$ dimers [11, 12].

Our previous results have been reviewed in [13]. Recent calculations of the $(CO)_2$ spectrum, while being qualitatively in agreement with experiment, exhibit significant differences in details and do not explain the observed peculiarities in the tunneling splitting [14]. The dynamic symmetry of CO dimers has been analyzed in [15].

It was hoped that investigation of the high-lying states of the $(CO)_2$ molecule with almost freely rotating monomers would not only supplement the pattern but also provide for a better understanding of the interplay of tunneling and rotations in this system. The spectral transitions to these states must have maximum intensities at a rotational temperature of $(CO)_2$ molecules on the order of 10–20 K. We have performed new measurements of the microwave absorption spectra for a supersonic gas jet of pure CO in the 81–175 GHz range and found 250 new spectral lines.[1] Our intracavity-jet OROTRON spectrometer and the experimental procedure were described in detail elsewhere [16]. This paper is devoted to the analysis and interpretation of obtained results.

First, let us briefly describe the structure of the rotational spectrum of the CO dimer. Since the distance between monomers is much greater than the monomer size, the ellipsoid of inertia corresponds to a strongly elongated, slightly asymmetric top. The rotational constants (inverse components of the ellipsoid of inertia) are related as $A \approx b_{CO} \gg B \approx C$, while the short ellipsoid axis a passes through the centers of gravity of the monomers (b_{CO} is the rotational constant of the CO molecule). The projection K of the total angular momentum J onto the intermolecular axis is well determined and offers a convenient classification of the rotational levels (although it is not a conserved quantity).

In the general case, the energies of rotational states are described by the following polynomials:

$$E(J, K) = \sigma_K + (B \pm \beta_K)J(J+1) - DJ^2(J+1)^2 + \ldots, \quad (1)$$

where

$$B \approx \hbar^2/2\mu r^2 \ll b_{CO}, \quad (2)$$

D is the centrifugal distortion constant, $\beta_K \ll B$ is the K-splitting constant ($\beta_0 = 0$), μ is the reduced mass of the dimer, and r is the distance between the centers of monomers. In the rigid rotator approximation, the first term is $\sigma_K \approx b_{CO}K^2$ and the rotational spectrum of the dimer differs from that of the symmetric top by removal of the degeneracy with respect to $\beta_K \neq 0$ for $K \neq 0$ and by the appearance of allowed transitions with $\Delta K \neq 0$.

In the model of freely rotating monomers, the K value is a sum of the projections of the intrinsic rotational moments (j_1, j_2) onto the intermolecular axis, $K = |\mathbf{j}_1 + \mathbf{j}_2|$, and

$$\sigma_K \approx b_{CO}[j_1(j_1+1) + j_2(j_2+1)]. \quad (3)$$

The tunneling splitting rather significantly (by ~4 cm^{-1}) separates the symmetric (A^+ symmetry) and antisymmetric (A^- symmetry) rotational levels of the CO dimer, so that each rotational state becomes split into two sets of levels of the same symmetry.[2] The energies of levels in each state are conveniently described by the formula

$$E_i^{\pm}(J, K) = \sigma_i(K) + B_iJ(J+1) - D_iJ^2(J+1)^2 \mp 1/2[\Delta\sigma_i(K) + \Delta B_iJ(J+1)], \quad (4)$$

where the signs "+" and "–" correspond to the level symmetry and the expression in square brackets refers to the parameters of tunneling splitting. The states with $K = 0$ include only the levels of the A^+ symmetry with even J and the levels of the A^- symmetry with odd J. The rotational levels of both shape isomers are composed of such states with the corresponding sets of constants. The spectral transitions are possible only between the levels of different symmetry (selection rules: $\Delta J = 0, \pm 1$; $A^+ \longleftrightarrow A^-$). As a result, there appears a specific "staircase" comprising alternating levels of different symmetry, by which it is possible to reach high-lying levels even at a low radiation energy. This circumstance was used in our investigation.

The measured absorption spectrum of $(^{12}C^{16}O)_2$ consists of separate, nonuniformly distributed lines with widths of about 300 kHz, which is close to the Doppler broadening. The observed shape of absorption

[1] The characteristic temperatures were ~15–20 K. In the previous experiments with a Ne–CO mixture, the jet temperature was 3–5 K.

[2] Rotational levels with the wave functions transforming according to the B representations of the C_h^2 symmetry group are missing in $(^{12}C^{16}O)_2$ with zero nuclear spins but appear in $(^{13}C^{16}O)_2$.

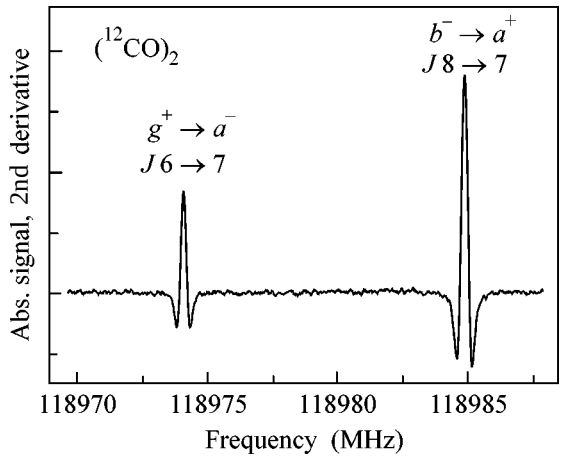

Fig. 1. Observed absorption lines $(^{12}C^{16}O)_2$ (second derivative). Figures at the peaks indicate energy levels involved in the given transition.

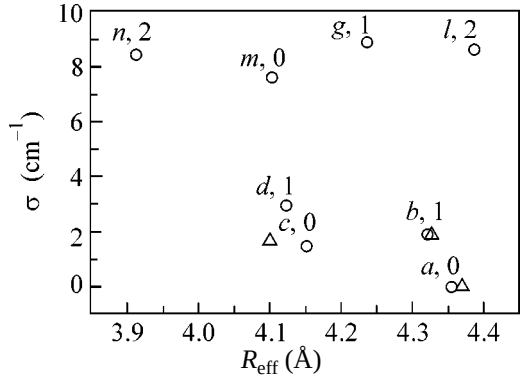

Fig. 2. Plot of the initial energy vs. effective dimer size for (○) $(^{12}C^{16}O)_2$ and (Δ) $(^{13}C^{16}O)_2$ (figures indicate *K* values) in various rotational states.

lines is illustrated in Fig. 1. As was mentioned above, we have found 250 new spectral transitions, the positions of which were determined to within 50 kHz.

An analysis of the experimental spectrum was performed, as in our previous investigations, by the technique of combination differences, according to which a difference (or sum) of the energies of transitions from two known levels to a third level is exactly equal to the energy difference between these levels. A computer program automatically selected the pairs of transitions with the required difference (sum) of frequencies and calculated the energy of the new level. As a rule, this level was considered to be found if there were no less than three transitions to this level (to within the accuracy of our calculations). Using the selection rules known for dipole transitions, we calculated the rotational angular momentum and the parity of each level, after which it was implemented in the analytical procedure. As a result of this analysis, we revealed 43 new levels of positive and negative parity in the energy interval 7.077–18.95 cm^{-1} (relative to the lowest level of the CO dimer) with the total rotational angular momenta *J* ranging from 0 to 10. These levels form four pairs of the new states (*m* with $K = 0$; *g* with $K = 1$; *l* with $K = 2$; *n* with $K = 1$ or 2).[3] A detailed description of the results with data on the transition frequencies and level energies will be published soon [17].

The level energies in each state are satisfactorily described by formula (4) with the constants B_i having reasonable values for the CO dimer and $D_i < 10^{-4}B_i$. This inequality implies that the centrifugal distortion is small and insignificant for the further analysis. Using the B_i values and formula (2), it is possible to calculate the average distances between monomers. The projection *K* (common of the rotational states) is determined by the *J* value of the lowest level ($K = J_{min}$). Unfortunately, we failed to find the lowest energy levels for the *n* state, so that the *K* value in this state is not exactly determined.

The main characteristics of all known rotational states of $(^{12}C^{16}O)_2$ and $(^{13}C^{16}O)_2$ (initial energies and average distances between monomers) are presented in Fig. 2. Note that the rotational constants somewhat differ from those reported previously, where these values were determined separately for the levels of A^+ and A^- symmetry. The processing of data by formula (4) provides for a much better coincidence of the rotational constants of various isotopomers. As can be seen from Fig. 2, these constants in the *a* and *b* states coincide to within the data-processing accuracy, while the small decrease in the size of $(^{13}C^{16}O)_2$ in the *c* state and the increase in the *a*–*c* splitting are correlated with the smaller curvature and greater asymmetry of the potential well for the O-bound isomer according to the calculations [14].

As can also be seen from Fig. 2, the new high-lying states significantly differ from the lower states. The latter form two groups with dimensions of about ≈0.41 nm (*c*, *d*) and ≈0.435 nm (*a*, *b*) and a reasonable (for the rigid top model) energy difference $\Delta E \approx 2\ cm^{-1} \approx b_{CO} = 1.91\ cm^{-1}$ between the $K = 0$ and $K = 1$ stacks, which is quite consistent with the two shape isomers. The new states, despite the large scatter of dimensions (from 0.39 to 4.4 nm), have close initial energies (8–9 cm^{-1}), which is quite consistent with the characteristics expected for the freely rotating monomers. It should be recalled that, in the rigid top model, the energy difference between $K = 2$ and $K = 0$ states must be $\Delta E \approx 4b_{CO}$. Analogous states with $K = 1$ and $K = 2$ previously found in *para*N_2–CO also have close energies, which provided grounds for their assignment to the $(j_{N2}, j_{CO}) =$

[3] Following [5], various rotational states of the CO dimer are denoted by lower-case Latin letters; the four lowest levels of the *g* state were previously found in [9].

(1, 1) group [3].[4] Thus, we have found a group of states in the CO dimer with almost free rotations (including counterrotations) of both monomers.

Of special interest is the *n* state with very small distance (0.39 nm) between the monomers. This contraction is quite natural, provided that both monomers are rotating in the same direction relative of the dimer axis. In this case, the same van der Waals bond length is achieved when the distance between the centers of gravity of the monomers is reduced by $0.5R_{CO} \cong 0.05$ nm. An analogous decrease in the size of a complex on the passage to the $K = 2$ $(j_{N2}, j_{CO}) = (1, 1)$ state was observed in *para*N_2–CO. This allows us to refine the quantum number K for the *n* state, since such a rotation corresponds to $K = 2$.

Taking into account that the new states of the COP dimer exhibit almost free rotations of the monomers, it is interesting to consider the well-known low-lying states as well. In the model admitting monomer rotations, the *a* and *c* states correspond to $(j_{CO}, j_{CO}) = (0, 0)$ states, while *b* and *d* correspond to $(j_{CO}, j_{CO}) = (1, 0)$, that is, to the rotation of only one monomer. However, the initial energies of the *b* and *d* states are significantly lower than the $b_{CO}j(j + 1)$ values typical of the free rotations, which implies strong retardation of the monomer rotations.

Finally, let us consider the results on the tunneling splitting. The main parameters (coefficients in formula (4)) for all the known states in $(^{12}C^{16}O)_2$ and $(^{13}C^{16}O)_2$ are presented in Fig. 3. As can be seen from these data, three of the new states (*m*, *n*, *g*) are characterized by approximately the same large splitting, while splitting of the *l* state is about half as small. As will be demonstrated below, this result indicates that only one monomer rotates: $(j, j) = (2, 0)$. Since the sizes of dimers in the *a*, *b*, and *l* states are close, the latter state is naturally identified with the $K = 2$ state of the C-bound isomer.

Within the framework of the model of monomer rotations, it is easy to explain the strong reciprocal dependence of splitting on the K value in both isomers. In this model, the *b* and *d* states are characterized by the rotation of only one monomer, $(j, j) = (1, 0)$, which breaks the exchange symmetry of the dimer and, accordingly, suppresses the tunneling transitions. In the *m*, *g*, and *n* states, both monomers rotate with the same *j*, and the tunneling is not suppressed despite the difference in K. Thus, the suppression of tunneling is determined by the asymmetry of monomer rotations in the CO dimer rather than by the K value. Analogous strong suppression of the tunneling as a result of broken exchange symmetry (caused by the excitation of vibrations in one of the monomers) was observed in $(HCl)_2$ [12] (however, the dependence of tunneling on K in this dimer was weak because the rotation of monomers was absent).

[4] To the best of our knowledge, the rotations of both monomers were not reported in other papers.

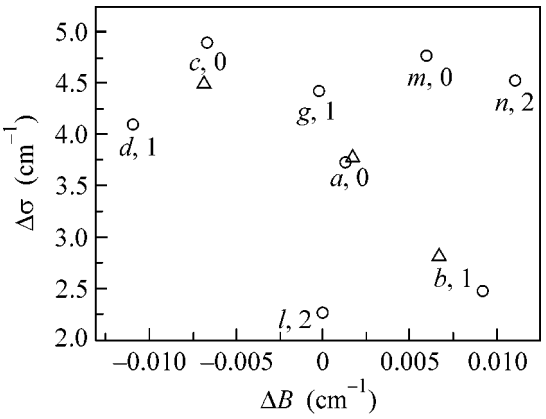

Fig. 3. Tunneling-splitting parameters for (○) $(^{12}C^{16}O)_2$ and (Δ) $(^{13}C^{16}O)_2$ (figures indicate K values) in various rotational states.

Since the suppression of tunneling splitting is stronger in the *l* state than in the *b* and *d* states, the asymmetry of internal rotations in the former case should be still more pronounced. This is possible if only one monomer rotates at $j = 2$. This state with $(j, j) = (2, 0)$ may also possess $K = 2$ and the initial energy between $4b_{CO}$ (in the rigid top limit) and $6b_{CO}$ (free rotations), which is quite consistent with characteristics of the *l* state. These considerations confirm the validity of assigning the *l* state with $K = 2$ to the C-bound isomer.

Thus, we can distinguish three groups of states having close properties with respect to the tunneling splitting: (i) *a*, *b*, and *l* (C-bound isomer); (ii) *c* and *d* (O-bound isomer); and (iii) *m*, *g*, and *n* (states with the rotation of both monomers). The minimum tunneling splitting is observed in the ground state of the C-bound isomer, while the O-bound and (1, 1) states are characterized by close tunneling rates. The dependence of the tunneling splitting on the rotations of the whole dimer (i.e., on J) is negative in the O-bound isomer and positive in the other cases. This dependence is weak for $K = 0$ and is an order of magnitude greater for $K > 0$.

The data in Fig. 3 also clearly demonstrate the dependence of the tunneling splitting on the reduced mass (unfortunately, measured only in three states of the dimer). There is some reasoning behind the positive dependence of splitting on the isotope mass in the *b* state. The barrier asymmetry in this state depends on the CO rotation rate. In ^{13}CO, this rate is naturally smaller and the asymmetry is lower. Apparently, this effect is stronger than the standard decrease in the probability of tunneling with increasing isotope mass. It is not excluded that resonance effects also play a certain role due to the proximity of splitting in the ground state (3.73 cm^{-1}) and the rotational energy ($2b_{CO} = 3.82$ cm^{-1}).

These considerations by no means eliminate the need for conducting quantum-mechanical calculations. We believe that such calculations can be more readily

performed for the group of new $(j_{CO}, j_{CO}) = (1, 1)$ states with almost freely rotating monomers.

In conclusion, new rotational states have been found in the $(CO)_2$ molecule. There are three states corresponding to the mutual rotations of both CO monomers with the projections of the total angular moment on the intermolecular axis $K = 0$, 1, and 2, and a state with one rotating monomer at $K = 2$. To our knowledge, the states with counterrotating monomers ($K = 0$) in molecular complexes have been found for the first time. The tunneling splitting was measured in all these states. It was demonstrated that the rotations of both monomers with the same j weakly influences the tunneling splitting, whereas the rotation of only one monomer suppresses this splitting.

The authors are grateful to D. Efremov, V.G. Koloshnikov, and V.R. Mironenko for fruitful discussions. This study was supported by the Russian Foundation for Basic Research, project nos. 03-02-17478 and 03-02-04006.

REFERENCES

1. P. E. S. Wormer and A. van der Avoird, Chem. Rev. **100**, 4109 (2000).
2. L. A. Surin, D. Roth, I. Pak, *et al.*, J. Chem. Phys. **112**, 4064 (2000).
3. C. Xia and A. R. W. McKellar, J. Chem. Phys. **113**, 525 (2000).
4. P. R. Bunker *et al.*, J. Mol. Spectrosc. **157**, 208 (1993).
5. M. D. Brookes and A. R. W. McKellar, Chem. Phys. Lett. **287**, 365 (1998).
6. M. D. Brookes and A. R. W. McKellar, J. Chem. Phys. **111**, 7321 (1999).
7. A. R. W. McKellar, J. Chem. Phys. **115**, 3571 (2001).
8. D. Roth, I. Pak, L. Surin, *et al.*, J. Chem. Phys. **113**, 3034 (2000).
9. Jian Tang, A. R. W. McKellar, L. A. Surin, *et al.*, J. Mol. Spectrosc. **214**, 87 (2002).
10. L. A. Surin, D. N. Fourzikov, *et al.*, J. Mol. Spectrosc. **223**, 132 (2004).
11. A. S. Pine, W. J. Lafferty, and B. J. Howard, J. Chem. Phys. **81**, 2939 (1984).
12. M. D. Schuder, C. M. Lovejoy, *et al.*, J. Chem. Phys. **99**, 4346 (1993).
13. L. A. Surin, D. N. Fourzikov, *et al.*, J. Mol. Spectrosc. **222**, 93 (2003).
14. G. W. M. Vissers, P. E. S. Wormer, and A. van der Avoird, Phys. Chem. Chem. Phys. **5**, 4767 (2003).
15. A. V. Burenin, Opt. Spektrosk. **95**, 208 (2003) [Opt. Spectrosc. **95**, 192 (2003)].
16. L. A. Surin, B. S. Dumesh, *et al.*, Rev. Sci. Instrum. **72**, 2535 (2001).
17. L. A. Surin *et al.*, J. Mol. Spectrosc. (in press).

Translated by P. Pozdeev